

THESIS FOR THE DEGREE OF DOCTOR OF PHILOSOPHY

Approximating the Three-Nucleon Continuum

- Solving the Faddeev equations for statistical inference of chiral forces -

SEAN B. S. MILLER

Department of Physics
CHALMERS UNIVERSITY OF TECHNOLOGY
Gothenburg, Sweden 2022

APPROXIMATING THE THREE-NUCLEON CONTINUUM

- SOLVING THE FADDEEV EQUATIONS FOR STATISTICAL INFERENCE OF CHIRAL FORCES -

Sean B. S. Miller

ISBN: 978-91-7905-721-3.

© Sean B. S. Miller, 2022

Doktorsavhandlingar vid Chalmers tekniska högskola

Ny serie nr 5187

ISSN 0346-718X

Department of Physics
Chalmers University of Technology
SE-412 96 Gothenburg
Sweden
Telephone +46 (0)31-7721000

Cover: The neutron vector analysing power, $A_y(n)$, for elastic neutron-deuteron scattering shown with respect to scattering energy ($E_{\text{Lab}} \in [1, 90]$ MeV) and angle ($\theta_{\text{c.m.}} \in [0, 180]$ degrees). The calculations were done using the Tic-tac code with $N_{\text{WP}} = 150$, $J \leq 3$, and $\mathcal{J} \leq \frac{17}{2}$, see Chap. 3, with the two-nucleon next-to-leading-order potential used in Paper III. The low-energy constants were set to the inferred maximum *a posteriori* values.

Chalmers Reproservice
Gothenburg, Sweden 2022

Approximating the Three-Nucleon Continuum
- Solving the Faddeev equations for statistical inference of chiral forces -
SEAN B. S. MILLER
Department of Physics
Chalmers University of Technology

Abstract

Three-nucleon forces (3NFs) are necessary to accurately describe the properties of atomic nuclei. These forces arise naturally together with two-nucleon forces (2NFs) when constructing nuclear interactions using chiral effective field theories (χ EFTs) of quantum chromodynamics. Unlike phenomenological nuclear interaction models, χ EFT promises a handle on the theoretical uncertainty in our description of the nuclear interaction. Recently, methods from Bayesian statistics have emerged to quantify this theoretical truncation error in physical predictions based on chiral interactions. Alongside quantifying the truncation error, the low-energy constants (LECs) of the chiral interactions must be inferred using selected experimental data. In this regard, the abundant sets of experimentally measured nucleon-nucleon (NN) and nucleon-deuteron (Nd) scattering cross sections serve as natural starting points to condition such inferences on. Unfortunately, the high computational cost incurred when solving the Faddeev equations for Nd scattering has thus far hampered Bayesian parameter estimation of LECs from such data. In this thesis, I present the results from a two-part systematic investigation of the wave-packet continuum discretisation (WPCD) method for reliably approximating two- and three-nucleon (NNN) scattering states with an aim towards a quantitative Bayesian analysis in the NNN continuum. In the first part, I explore the possibilities of using graphics processing units to utilise the inherent parallelism of the WPCD method, focusing on solving the Lippmann-Schwinger equation. In the second part, I use the WPCD method to solve the Faddeev equations for Nd scattering and analyse the reliability of the approximations of the WPCD method. This allows me to quantify the posterior predictive distributions for a range of low-energy neutron-deuteron cross sections conditioned on NN scattering data and NN interactions up to fourth order in χ EFT.

Publications

This thesis is based on the work contained in the following papers:

- I “Wave-packet continuum discretisation for nucleon–nucleon scattering predictions”
S. B. S. Miller, A. Ekström, and C. Forssén
Preprint: [arXiv:2106.00454](https://arxiv.org/abs/2106.00454) [nucl-th]
J. Phys. G 49 (2022) 2, 024001
- II “Neutron-deuteron scattering cross-sections with chiral NN interactions using wave-packet continuum discretization”
S. B. S. Miller, A. Ekström, and K. Hebeler
Preprint: [arXiv:2201.09600](https://arxiv.org/abs/2201.09600) [nucl-th]
Phys. Rev. C 106 (2022), 024001
- III “Posterior predictive distributions for neutron-deuteron cross sections”
S. B. S. Miller, A. Ekström, and C. Forssén
Preprint: [arXiv:2209.06501](https://arxiv.org/abs/2209.06501) [nucl-th]
(submitted to *Phys. Rev. C*)

This thesis is also based on the following research software. The code is not appended to this thesis but can be downloaded via the provided web address.

- I “Tic-tac” - An open-source research code for three-nucleon scattering calculations based on wave-packet continuum discretization
S. B. S. Miller, A. Ekström, and K. Hebeler
Licence: GPLv3
<https://github.com/seanbsm/Tic-tac>

Statement of contributions

My contributions to the included papers were:

- I I developed the code, generated the numerical data, performed the analyses, generated the figures, and wrote the majority of the text.
- II I developed the code (Tic-tac), generated the numerical data, performed the analyses together with my co-authors, wrote the methodology sections and the appendices, and wrote the other sections together with my co-authors.
- III I generated the numerical data, performed the analyses together with my co-authors, wrote the methodology section, and wrote the other sections together with my co-authors.

Acknowledgements

In my opinion, there is no such thing as a self-made person. I know I would not have been able to undertake a PhD if my mother had not taught me the value of hard work. Nor would I have been so curious as to start one, had my father not taught me the value of pursuing answers. I know I wouldn't have known where to go so surely, had my brother not already trodden the path that I walk. Those who stood alongside me through school and university would have left me isolated, insecure, and scared, had they not been there for me to call my friends. And at last, had she not been my constant support and guidance, source of happiness and laughter, and the light in my everyday, I know I would not take another step into the future with the same courage I now have, together with my Adri.

Among the many more I owe my gratitude, there are few who I would especially like to give my thanks. I thank my advisors, Andreas Ekström and Christian Forssén, for their ample and invaluable feedback, and wonderful group leadership. I have learned a lot in my time here, and much more than physics alone. I know Andreas is not one to seek praise, but I firmly believe I could not have gotten a better advisor. I also thank my examiner, Gabriele Ferretti, for his continuous interest in my PhD studies, and Håkan T. Johansson, for providing endless support to the whole group. I would also like to thank my other colleagues, both past and present; Tor Djärv, Isak Svensson, Oliver Thim, Giovanni Bruni, Alexandra Roussou, Chieh-Jen Yang, Weiguang Jiang, and Eric Nilsson, as well as the remaining subatomic and high-energy physicists at Chalmers. You have all given me wonderful discussions and ideas throughout my studies, and, of course, a lot of fun besides. Isak, Oliver, and Erik: I wish you all the best in your continued studies.

Furthermore, I would, of course, also like to thank the rest of my family, all the friends I have met during my time here in Gothenburg (you know who you are), and my close friend, Brage Blix. You all have been wonderfully supportive along the way.

I know I am not a self-made person, but I hope, with this crystallisation of my strife over these last few years, I pay homage to those who have carried me so far.

Til minne av Pappa

-

Jeg savner deg

“And you,” I said with childish impertinence, “never commit errors?”

“Often,” he answered. “But instead of conceiving only one, I imagine many, so I become a slave of none.”

- Brother William and novice Adso,
The Name of the Rose

List of acronyms

	Symbols	HMC	Hamiltonian Monte Carlo
NN	nucleon-nucleon		L
NNN	three-nucleon		
Nd	nucleon-deuteron	LEC	low-energy constant
χ EFT	chiral effective field theory	LO	leading order
nd	neutron-deuteron	LS	Lippmann-Schwinger
np	neutron-proton		M
pd	proton-deuteron		
2NF	two-nucleon force		
3NF	three-nucleon force	MAP	maximum <i>a posteriori</i>
	A	MI	matrix-inversion
AGS	Alt-Grassberger-Sandhas		N
	C	N^2 LO	next-to-next-to-leading order
c.m.	centre-of-mass	N^3 LO	next-to-next-to-next-to-leading order
CIB	charge independence breaking	NLO	next-to-leading order
COO	coordinate format		P
CPU	central processing unit		
CSC	compressed sparse column		
CSR	compressed sparse row	PA	Padé approximant
	D	PDF	probability density function
DoB	degree-of-belief	PPD	posterior predictive distribution
	E		Q
EFT	effective field theory	QCD	quantum chromodynamics
	F		R
FWP	free wave packet	RMSE	root-mean square error
	G		S
GiB	gibibyte	SWP	scattering wave packet
GPU	graphics processing unit		W
	H		
HDPI	highest posterior density interval	WPCD	wave-packet continuum discretisation

Contents

List of acronyms	xiii
1 Introduction	1
2 Few-nucleon scattering	7
2.1 Kinematics and the partial-wave bases	8
2.1.1 Partial-wave bases	10
2.1.2 Antisymmetrisation and the permutation operator	11
2.2 Two-nucleon scattering	13
2.2.1 The spin-scattering matrix	13
2.2.2 The Lippmann-Schwinger equation	14
2.2.3 Convergence of NN scattering solutions	16
2.3 Three-nucleon scattering	16
2.3.1 The spin-scattering matrix	17
2.3.2 The Faddeev equations	18
2.3.3 Benchmarking the permutation matrix	21
3 Wave-packet continuum discretisation	25
3.1 The wave-packet basis	25
3.2 Approximate scattering states	27
3.3 The Lippmann-Schwinger equation in WPCD	28
3.3.1 Solving the LS equation in parallel	29
3.3.2 Some considerations in utilising a GPU	30
3.3.3 Convergence of the WPCD method for NN scattering	32
3.4 The Faddeev equations in WPCD	35
3.4.1 Solving the Faddeev equations	36
3.4.2 Convergence of the WPCD method for elastic Nd scattering	42
4 Posterior predictive distributions for neutron-deuteron scattering cross sections	47
4.1 Theoretical predictions and uncertainty	47
4.2 Statistical model for evaluating PPDs	49

4.2.1	Sample correlations and PPD integral evaluation	50
4.2.2	Trading method accuracy for computational speed	50
4.2.3	Theoretical uncertainty modelling	52
4.3	PPD analysis and interpretation	54
4.3.1	The total cross section	54
4.3.2	Differential cross section and A_y -observable	55
5	Summary and outlook	61
A	Discretising the continuum using pseudostate eigendifferentials	67
B	Posterior predictive distributions for neutron-deuteron spin-observables	69

Chapter 1

Introduction

A term used in physical science is “*ab initio*”, with literal meaning “from the beginning”. It is often used when referring to the practice of explaining a physical phenomenon from first, or fundamental, principles, which is a common motivation in the natural sciences. In nuclear physics, atomic nuclei and nuclear matter are mainly governed by the strong nuclear force, of which quantum chromodynamics (QCD) is our most fundamental theory. It states that quarks interact by the exchange of gluons that carry charges of colour, hence the name “chromo”, similarly to how photons carry the electromagnetic force. This theory became part of the Standard Model of particle physics: a crowning achievement of international scientific collaboration throughout the latter half of the 20th century, which ultimately depended on large high-energy accelerator facilities for experimental verification [1].

At high energies, QCD is a perturbative theory. Asymptotic freedom reduces the strength of the strong coupling constant appearing at each coupling vertex between quarks and gluons [2]. This means that the infinitely many quark-gluon and gluon-gluon couplings, provided by the QCD Lagrangian, can be truncated. This makes it possible to make theoretical predictions of high-energy observables, which was needed to establish QCD. However, at the low energies in naturally occurring nuclei, the strong coupling constant is on the order of unity, such that all combinations of strong couplings contribute equally when making predictions. This makes perturbative calculations impossible. A way around this builds on the pioneering work on effective field theories (EFTs) by, among others, S. Weinberg, who articulated the concept in 1979 [3].

An EFT can be used to provide models at a given energy, or momentum, scale of a physical system where multiple scales are present [4]. The presumption for such a theory to be effective is that the fine details of interactions at one scale should not affect the interactions at another. For example, the orbits of planets matter little more to the movements of galaxies beyond the mass of individual

solar systems, but these systems only exist if the planets stay in orbit, i.e., through the fine details. Weinberg’s suggestion was to write the most general Lagrangian possible that is consistent with the symmetries of an underlying field theory, using all relevant degrees of freedom at the scale of interest.

One key advantage of an EFT is that its derived models allow for calculable, order-by-order improvable predictions. The region of validity of an EFT is encapsulated in the “soft” scale, Q , of the physics we wish to describe and a “hard”, or “breakdown”, scale, Λ_b , where we expect the EFT to start failing. With Q and Λ_b defined, one can assign a hierarchy to the EFT interaction diagrams in terms of their contribution to the force acting between the degrees of freedom. Terms with a higher exponent of $\frac{Q}{\Lambda_b}$ are then naively assumed to contribute less, thus providing a perturbative theory. This hierarchy is known as power counting.

In constructing an EFT of QCD, one ends up with a Lagrangian abiding by the symmetries of QCD, with pions and nucleons as the relevant degrees of freedom. The resulting EFT for pion-nucleon interactions is known today as chiral perturbation theory [5], while extensions to include interactions between nucleons is known as chiral effective field theory (χ EFT) [6–11]. The prefix “chiral” comes from the chiral symmetry of massless quarks, which is spontaneously broken to give Nambu-Goldstone boson fields corresponding to pions. Through chiral symmetry breaking, pions replace gluons as the strong-force mediators in χ EFT. For reviews on χ EFTs, as well as pionless χ EFTs, which I will neglect in the remaining text, I refer the reader to, for example, Refs. [12–14].

In this work, I use Weinberg power counting to do calculations, where interaction diagrams get assigned to *chiral orders*, $\nu \geq 0$, as illustrated in Fig. 1.1. Note there exists other power-counting schemes such as modified Weinberg power counting, see, e.g., the discussion of Ref. [15], but I will not discuss these here. By truncating the series at a given order ν , we get a finite set of interaction diagrams that we can evaluate. By including higher orders, starting from leading order (LO) and going to next-to-leading order (NLO), next-to-next-to-leading order (N²LO), and next-to-next-to-next-to-leading order (N³LO), etc, we should hopefully converge onto the nuclear physics that would be predicted by low-energy QCD.

Remarkably, unlike phenomenological nuclear potentials where interactions are constructed “by hand”, χ EFT inherently provides many-nucleon interactions as dictated to exist by QCD [14], in addition to two-nucleon forces (2NFs). It is reasonable to expect three-nucleon (NNN) interactions, arising already at the third order, to significantly contribute to the nuclear force and our predictions of nuclear systems. In fact, it is well known that they are often essential to accurately reproduce nuclear data, showing significant effects all the way in going from light nuclei to infinite nuclear matter [16, 17]. The importance of including the three-nucleon forces (3NFs) entails a need for statistical inference of chiral potentials using data from systems of more than two nucleons. Building

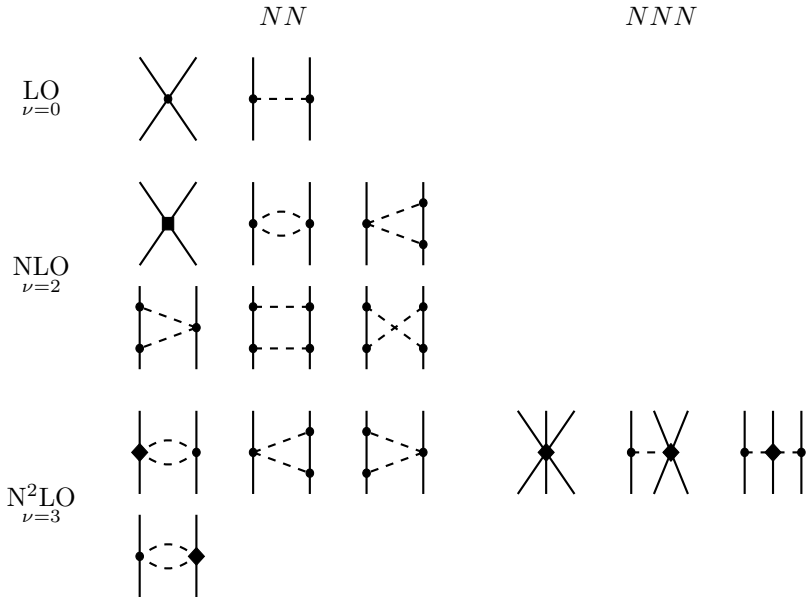


Figure 1.1: The LO, NLO, and N^2 LO diagrams for the nucleon-nucleon (NN) and NNN interactions [14]. The solid lines represent nucleons, while the dashed lines are pions. The circle, diamond, and square vertices denote the number of pion mass- and/or momentum-factors, 0, 1, and 2, respectively. All diagrams with $\nu = 1$ violate time- and parity-reversal invariance.

on this, it is the main purpose of this work to quantify theoretical uncertainty in predictions of NNN scattering observables, i.e., the NNN continuum.

One source of theoretical uncertainty arises from interaction vertices such as those appearing in Fig. 1.1. Each interaction vertex symbolises a coupling constant where the underlying, high-energy physics in a nucleon-nucleon, pion-nucleon, etc, vertex are subsumed into a low-energy constant (LEC). The LEC values are *a priori* undetermined and can be inferred from nuclear data. In principle, one can extract them from QCD using, for example, lattice QCD [18]. While there is currently much progress in the lattice QCD community, the method remains computationally inhibiting for determining LECs [19], leaving statistical inference conditioned on nuclear data as the commonly-used method of choice. For this, I use methods from Bayesian statistics, as will be covered in Chap. 4.

Given that χ EFT is a low-energy theory, one expects that LECs should be inferred from low-energy observables such as nuclear structure observables, for example binding energies. Computational *ab initio* methods for solving the

many-body Schrödinger equation as well as calculating heavy nuclear reactions have seen astonishing development [20–23]. However, such observables also rely on many-nucleon forces which appear at higher chiral orders. Furthermore, the external momentum used for the chiral soft scale is ambiguous when making bound-state predictions, as touched upon in, e.g., Ref. [24]. For a χ EFT model with 2NFs and 3NFs, as motivated above, NN and nucleon-deuteron (Nd) scattering data are handy. These are physically simple systems with few nucleons and a clear external momentum. They also provide a continuum of scattering energies for which there is ample experimental data, readily available in, e.g., the EXFOR database [25]. The continuous energy-dependency of scattering observables allows, for example, a controlled investigation of the χ EFT region of validity, and, of course, ample data to infer LECs.

In Chap. 2 I will present the formalism of NN and NNN scattering. Observable calculations for NN and Nd scattering require solutions to either the Lippmann-Schwinger (LS) equation or the Faddeev equations [26], respectively. The former equation, together with the NN Schrödinger equation, can be solved cheaply to such an extent that extensive Bayesian inference of 2NFs have been performed [27–32]. The Faddeev equations, however, are much more demanding to solve computationally.

There exist several computational methods for solving the Faddeev equations. One can either use momentum-space representations [33] or coordinate-space representations. Groups working with the latter use, e.g., the Kohn variational principle with the Faddeev equations [34], or use the hyperspherical harmonics method [35]. With these methods, much insight has been gained into chiral forces from data in the NNN continuum [36–42]. Nonetheless, these methods are often plagued by computationally demanding mathematical traits such as energy-dependent moving singularities or requiring special treatment of the asymptotic wave function [43]. Ultimately, a full Bayesian analysis of 2NFs and 3NFs involving the NNN continuum has been inhibited due to the computational complexity of solving the Faddeev equations. Alongside this work, there has been much development in the use of model reduction methods such as emulators like eigenvector continuation [44–47], low-rank matrix-decomposition [48, 49], and other specialised methods [50]. However, while promising for future work, most of these methods are not yet applicable for Nd scattering. Instead, bound-state methods offer appealing advantages [43], one method of which comes from wave-packet continuum discretisation (WPCD) [51].

The WPCD method is a bound-state method for approximating scattering states. Using approximate scattering states allows one to greatly simplify the computational cost of solving the Faddeev equations [52]. The wave-packet basis representation averages operators and removes energy-dependent singularities. This feature makes the method inherently suited for parallel computations, promoting efficient use of parallel computational resources [53]. Of course, the method has some drawbacks, worst of which is the need for a greater state

space to accurately model the physics of the NNN continuum, compared to other methods.

In Chap. 3 I will cover the formalism, computational aspects, and convergence of the WPCD method in detail, for both the LS and Faddeev equations, summarising the studies of Papers I and II. In Paper I, I implemented the WPCD method to do parallel calculations on a graphics processing unit (GPU) to investigate speedup of NN scattering calculations. In Paper II, I implemented the WPCD method for solving the Faddeev equations and investigated its accuracy in calculating elastic Nd scattering observables. A result of the study was the development of an open-source code for solving the Faddeev equations, named Tic-tac, which will also be covered in Chap. 3.

In Chap. 4 I present the study of Paper III, which was motivated by longstanding, unresolved discrepancies between experimental data and theoretical predictions in the NNN continuum, such as the “ A_y puzzle” [54, 55]. While there are studies that suggest 3NFs are necessary to resolve these discrepancies [56, 57], there exist, to date, no fully Bayesian analyses to document this necessity. One such Bayesian approach is to investigate the posterior predictive distributions (PPDs) with 2NF-only models with LECs conditioned on, for example, NN scattering data. A PPD is a prediction of new observables conditioned on past data; in this case, neutron-deuteron (nd) scattering predictions from χ EFT 2NF models conditioned on NN scattering data. This would root out 2NF LEC-variability as the cause of discrepancy, barring wrongful inference of the LECs. Investigation of these PPDs, up to and including N^3 LO with neglected 3NFs, was the topic of study in Paper III.

While the reach of this work does not extend all the way to an inclusion of 3NFs in statistical studies of chiral forces in, or with, the NNN continuum, the work serves as an important first step in a new direction towards this goal. By the inclusion of 3NFs in our description of nuclear forces, we hopefully take a significant next step towards an age of highly predictive nuclear theory, which can help transform nuclear systems into precision tools in the exploration of new physics and technologies.

Chapter 2

Few-nucleon scattering

In scattering experiments there are usually two freely-moving bodies in the initial state prior to scattering. Post-scattering, there are four possible “channels” to consider [58, 59]:

1. Elastic scattering - only kinetic energy is transferred between the two colliding bodies. There occur no state excitations or exchanges of constituent particles.
2. Inelastic scattering - kinetic energy is transferred between the two colliding bodies to give state excitations in one or both bodies.
3. Break-up - The bodies can break apart in the scattering process, giving more than two outbound bodies to measure.
4. Rearrangement or transfer - Constituent particles are exchanged between the two bodies.

In this work I have studied elastic NN and Nd scattering. I will return briefly to the topic of deuteron break-up in Nd scattering in Chap. 3 to show that in the WPCD formalism we can extract both elastic and break-up observables from the same calculation.

In elastic scattering there are in general five different types of polarisation measurements we can do. These are shown in Tab. 2.1, in addition to the usual measurements of total (integrated) and differential cross sections. See Ref. [60] for a broader, general discussion on spin and polarisation experiments for $2 \rightarrow 2$ scattering. Any spin-operator \hat{O} that polarises reactants as in the table can be projected onto a spin basis via [62]

$$\langle \hat{O} \rangle = \frac{\text{Tr}\{M\hat{\rho}_i M^\dagger \hat{O}\}}{\text{Tr}\{M\hat{\rho}_i M^\dagger\}}, \quad (2.1)$$

Table 2.1: Types of spin-polarisation observables [60] written in the Madison convention [61]; the arrow signifies a reactant with known polarisation. Here I use standard nuclear reaction notation, i.e., $A(b, c)D$, which symbolises $A + b \rightarrow c + D$.

Polarisation	Observable type
$A(\vec{b}, \vec{c})D$	Polarisation
$A(\vec{b}, c)D$	Analysing power
$A(\vec{b}, \vec{c})\vec{D}$	Polarisation transfer
$\vec{A}(\vec{b}, c)D$	Spin correlation (initial channel)
$A(\vec{b}, \vec{c})\vec{D}$	Spin correlation (final channel)

where $\hat{\rho}$ are spin-density operators represented via the Pauli spin matrices, and M is the spin-scattering matrix containing all the transition amplitudes between different spin polarisations of the initial and final states. Note that M will depend on the scattering energy and angle, here written $E_{\text{c.m.}}$ and $\theta_{\text{c.m.}}$ in the centre-of-mass (c.m.) system, respectively. Any solutions to the LS equation or Faddeev equations, which I here refer to collectively as scattering equations, would be contained in M . In the following I will discuss NN elastic scattering and the LS equation, and from there continue to Nd scattering and the Faddeev equations. I will illustrate the underlying theoretical methodology and emphasise some of the computational challenges involved in solving them. First, however, I define the partial-wave bases for NN and NNN states.

2.1 Kinematics and the partial-wave bases

There are three quantities typically used in the description of elastic scattering data; the laboratory kinetic energy E_{Lab} , the c.m. energy $E_{\text{c.m.}}$, and the c.m. relative momentum, written here as p (q) for the two-body (three-body) system, where I will denote the reduced mass as μ_0 (μ_1). The Jacobi momenta, used to uniquely describe N -body dynamics in c.m. systems, are here expressed as follows.

Each nucleon i has a momentum \mathbf{k}_i and mass m_i . The Jacobi momentum in a two-body system (12) is then

$$\mathbf{p}_{12} \equiv \frac{m_2 \mathbf{k}_1 - m_1 \mathbf{k}_2}{m_1 m_2}, \quad (2.2)$$

where Fig. 2.1 illustrates the directions of the vectors. With a third nucleon 3 relative the (12) two-body system, referred to now as the *pair* system, the c.m.

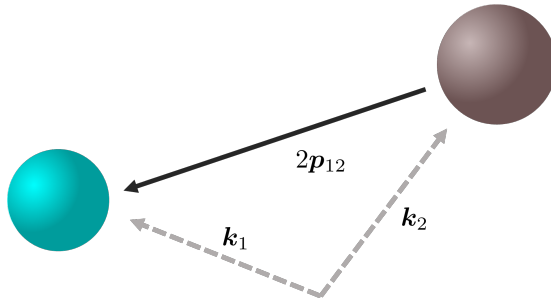


Figure 2.1: The nucleon-nucleon system. Each nucleon has momentum \mathbf{k}_i , relative to an arbitrary reference frame.

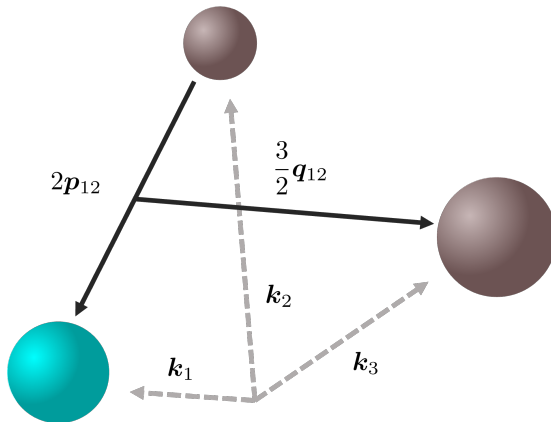


Figure 2.2: Illustration of the neutron-deuteron system. Each nucleon has momentum \mathbf{k}_i , relative to an arbitrary reference frame.

momentum of the third nucleon, often referred to as the *spectator* nucleon, is

$$\mathbf{q}_{12} \equiv \frac{(m_1 + m_2)\mathbf{k}_3 - m_3\mathbf{p}_{12}}{m_1 + m_2 + m_3}, \quad (2.3)$$

as illustrated in Fig. 2.2. While the two-body system only has two options for ordering the Jacobi momentum, (12) and (21), the three-body system has $3! = 6$ possible orderings. The relations between momentum expressions using different orderings are presented in Tab. 2.2. Naturally, the ordering of Jacobi momenta should not impact the outcome of our calculations. The relations between the free relative momentum, E_{Lab} , and $E_{\text{c.m.}}$ are shown in Tab. 2.3.

Table 2.2: Jacobi momentum equalities for the two- and three-body systems with equal masses and momenta \mathbf{k}_1 , \mathbf{k}_2 , and \mathbf{k}_3 [17]. In each case one can simply permute the pair-system indices, e.g. $(ij) \leftrightarrow (ji)$, to get equivalent expressions. Note the appearance of the total momentum $\mathbf{P} \equiv \sum_{i=1}^3 \mathbf{k}_i$.

	\mathbf{p}_{ij}	\mathbf{q}_{ij}	\mathbf{k}_i
\mathbf{k}_i	$\frac{1}{2}(\mathbf{k}_i - \mathbf{k}_j)$	$\frac{2}{3}(\mathbf{k}_k - \frac{1}{2}(\mathbf{k}_i + \mathbf{k}_j))$	\mathbf{k}_i
(ij)	\mathbf{p}_{ij}	\mathbf{q}_{ij}	$\mathbf{p}_{ij} - \frac{1}{2}\mathbf{q}_{ij} + \frac{1}{3}\mathbf{P}$
(jk)	$-\frac{1}{2}\mathbf{p}_{jk} + \frac{3}{4}\mathbf{q}_{jk}$	$-\mathbf{p}_{jk} - \frac{1}{2}\mathbf{q}_{jk}$	$\mathbf{q}_{jk} + \frac{1}{3}\mathbf{P}$
(ki)	$-\frac{1}{2}\mathbf{p}_{ki} - \frac{3}{4}\mathbf{q}_{ki}$	$\mathbf{p}_{ki} - \frac{1}{2}\mathbf{q}_{ki}$	$-\mathbf{p}_{ki} - \frac{1}{2}\mathbf{q}_{ki} + \frac{1}{3}\mathbf{P}$

Table 2.3: Conversion formulae between laboratory energy, E_{Lab} , c.m. relative momentum $p \equiv \|\mathbf{p}\|$, and c.m. energy $E_{\text{c.m.}}$ for two-body elastic scattering. For generality, m_t and m_b are the target- and beam-particle masses, respectively, and $\mu \equiv \frac{m_t m_b}{m_t + m_b}$ is the c.m. system's reduced mass. The relations between E_{Lab} and $E_{\text{c.m.}}$ are easily derived through p and hence omitted. These equations apply equally for NN and Nd scattering.

	p	$E_{\text{c.m.}}$	E_{Lab}
p	p	$\sqrt{2\mu E_{\text{c.m.}}}$	$\sqrt{\frac{m_t^2 E_{\text{Lab}}(E_{\text{Lab}} + 2m_b)}{(m_t + m_b)^2 + 2E_{\text{Lab}}m_t}}$
$E_{\text{c.m.}}$	$\frac{p^2}{2\mu}$	$E_{\text{c.m.}}$	[Omitted]
E_{Lab}	$\frac{1}{m_t} \left[\sqrt{(p^2 + m_t^2)(p^2 + m_b^2)} + p^2 - m_b m_t \right]$	[Omitted]	E_{Lab}

2.1.1 Partial-wave bases

A single nucleon state is defined by momentum \mathbf{k} , spin \mathbf{s} , orbital angular momentum \mathbf{l} , total angular momentum $\mathbf{j} \equiv \mathbf{l} + \mathbf{s}$, and isospin \mathbf{t} . I will assume the neutron and proton to be identical particles with nucleon mass¹ $m_N \equiv \frac{2m_p m_n}{m_p + m_n}$, with proton and neutron masses m_p and m_n , respectively, in different isospin states. I let the beam-axis \hat{z} be the quantisation axis, and use standard notation such as $j \equiv \|\mathbf{j}\|$ and $m_j \equiv \mathbf{j} \cdot \hat{z}$. Isospin, however, is written with $t_z \equiv \mathbf{t} \cdot \hat{z}$. Lastly, as above, I use $k \equiv \|\mathbf{k}\|$. I denote the partial-wave state for the single nucleon as

$$|k; \eta\rangle \equiv |k; s, l, t, t_z\rangle, \quad (2.4)$$

where $\eta \equiv \{(ls)j, t, t_z\}$, and where the parenthesis-notation $(ls)j$ signifies the order of coupling. Note that $s = t = \frac{1}{2}$ for nucleons. All dependence on m_j is

¹Note that $m_N \equiv \frac{m_p + m_n}{2}$ is also common to use. The difference between the definitions is at the 7th significant digit and causes no visible change in calculated observables.

resolved outside of the scattering equations due to rotational invariance and is thus usually omitted from the state expression.

With two nucleons we can define a coupled basis by coupling first the spin and orbital angular momenta as $\mathbf{S} \equiv \mathbf{s}_1 + \mathbf{s}_2$ and $\mathbf{L} \equiv \mathbf{l}_1 + \mathbf{l}_2$, where for example \mathbf{s}_1 is the spin of nucleon 1, followed by the coupling to total angular momentum $\mathbf{J} \equiv \mathbf{L} + \mathbf{S}$. The isospin is also coupled as $\mathbf{T} = \mathbf{t}_1 + \mathbf{t}_2$. The NN partial-wave states are defined as

$$|p; n\rangle \equiv |k; \eta\rangle_1 \otimes |k; \eta\rangle_2 = |p; (LS)J, T, T_z\rangle_{12}, \quad (2.5)$$

where n denotes the set of pair-system quantum numbers and $p \equiv \|\mathbf{p}_{12}\|$. Note one can instead couple \mathbf{j} of each nucleon to get \mathbf{J} . This, and the convention above, are referred to as jj - and LS -schemes, respectively.

Given a system of three nucleons, we can first couple two of them into a pair system as above. Then we can couple the pair state to the last nucleon; the *spectator* nucleon. Again, there are two ways to do this. Either we couple $(Ll)\mathcal{L}$ and $(Ss)\mathcal{S}$ to $(\mathcal{L}\mathcal{S})\mathcal{J}$, or use $(Jj)\mathcal{J}$. I will define NNN partial-wave states using (Jj) -coupling,

$$\begin{aligned} |p, q; \alpha\rangle &\equiv |k; \eta\rangle_1 \otimes |k; \eta\rangle_2 \otimes |k; \eta\rangle_3 \\ &= |p; n\rangle_{ij} \otimes |q; \gamma\rangle_{ij} \\ &= |p, q; (LS)J, (ls)j, (Jj)\mathcal{J}, (Tt)\mathcal{T}, \mathcal{T}_z\rangle_{ij}, \end{aligned} \quad (2.6)$$

where the subscript (ij) denotes the pair system and $(i, j, k) \in [1, 2, 3]$ are unequal each other, and where $\gamma \equiv \{(ls)j, t, t_z\}$ is relative the c.m. of the pair. Since $s = t = \frac{1}{2}$ and $t_z = \mathcal{T}_z - T_z$, I will abbreviate $\gamma = \{l, j\}$. Due to conservation of total angular momentum and parity we usually denote NNN channels by \mathcal{J}^Π , where $\Pi \equiv (-1)^{L+l}$ is the NNN parity. For the remaining text, unless otherwise stated, I will use n to denote the set of pair-system quantum numbers, γ for the spectator nucleon relative to the pair, and $\Gamma \equiv \{\mathcal{J}\mathcal{T}\mathcal{T}_z\}$ for total NNN state, such that $\alpha = \{n, \gamma, \Gamma\}$. This shorthand notation will be convenient later when discussing NN operators in NNN state space in Chap. 3. Another commonly used shorthand notation I will use hereafter is the ‘‘odd-man-out’’ notation, where a subscript i symbolises (jk) . I will omit the z -components t_z , T_z and \mathcal{T}_z and assume them implicitly set when discussing operator representations.

2.1.2 Antisymmetrisation and the permutation operator

An arbitrary, N -fermion system requires antisymmetric wave functions as dictated by the Pauli exclusion principle. We can fully antisymmetrise states using the N -body antisymmetrisation operator [63],

$$\hat{A}_{123\dots N} = \frac{1}{N!} \sum_{\hat{P} \in S_N} (-1)^i \hat{P}, \quad (2.7)$$

where \hat{P} are permutation operators of particles indices, i is the number of permutations by \hat{P} , and S_N is the symmetric group. The group has $N!$ elements, i.e. $N!$ distinct orderings of N particles. In the case of NN states, $|ab\rangle$, where a and b refers to the individual nucleons, this becomes

$$\hat{A}_{12} = \frac{1}{2!} \left(\mathbb{1} - \hat{P}_{12} \right), \quad (2.8)$$

where the permutation operator swaps particles 1 and 2 such that

$$\hat{P}_{12}|ab\rangle = |ba\rangle. \quad (2.9)$$

Letting \hat{A}_{12} act on the partial-wave basis states $|p; n\rangle$ returns the same state but with a well-known prefactor [59],

$$\hat{A}_{12}|p; n\rangle = \frac{1}{2} [1 - (-1)^{L+S+T}] |p; n\rangle, \quad (2.10)$$

i.e. the state cannot be antisymmetric unless $(-1)^{L+S+T} = -1$, often called the “generalised” Pauli exclusion principle. The fact that all antisymmetry of the two-nucleon states can be contained in a simple prefactor, which we can easily extract from any operator expectation values, makes it straightforward to define fully antisymmetric NN states.

In the NNN case we have $3!$ unique orderings, and the antisymmetrisation operator is written,

$$\begin{aligned} \hat{A}_{123} &= \frac{1}{3!} \left(\mathbb{1} - \hat{P}_{12} - \hat{P}_{23} - \hat{P}_{13} + \hat{P}_{123} + \hat{P}_{132} \right) \\ &= \frac{1}{3!} \left(\mathbb{1} - \hat{P}_{ij} \right) \left(\mathbb{1} + \hat{P}_{123} + \hat{P}_{132} \right), \end{aligned} \quad (2.11)$$

where, for example,

$$\hat{P}_{132}|abc\rangle \equiv \hat{P}_{13}\hat{P}_{32}|abc\rangle = \hat{P}_{13}|acb\rangle = |bca\rangle. \quad (2.12)$$

One can see that Eq. (2.11) contains \hat{A}_{ij} , such that

$$\hat{A}_{123} = \frac{1}{3} \left(\mathbb{1} + \hat{P}_{123} + \hat{P}_{132} \right) \hat{A}_{ij} \quad \forall (ij). \quad (2.13)$$

This means that the three-body antisymmetrisation operator can be expressed in terms of the antisymmetrisation operator of any of the three possible pair-systems (ij) . Thus, given a state $|p, q; \alpha\rangle_{ij} = |p; n\rangle_{ij} \otimes |q; \gamma\rangle_{ij}$, we can first antisymmetrise the pair-system state to give *partially*-antisymmetric partial-wave NNN states. Assuming $|p; n\rangle_{ij}$ to be already antisymmetric, we have

$$\begin{aligned} \hat{A}_{123}|p, q; \alpha\rangle_{ij} &= \frac{1}{3} \left(\mathbb{1} + \hat{P}_{123} + \hat{P}_{132} \right) \hat{A}_{ij}|p, q; \alpha\rangle_{ij} \\ &= \frac{1}{3} \left(\mathbb{1} + \hat{P}_{123} + \hat{P}_{132} \right) |p, q; \alpha\rangle_{ij}. \end{aligned} \quad (2.14)$$

Furthermore, for partially-antisymmetric states, the two operators \hat{P}_{123} and \hat{P}_{132} have the same effect [59],

$$\begin{aligned} {}_{23}\langle p', q'; \alpha' | \hat{P}_{132} | p, q; \alpha \rangle_{23} &= (-1)^{L'+S'+T'} (-1)^{L+S+T} {}_{23}\langle p', q'; \alpha' | \hat{P}_{123} | p, q; \alpha \rangle_{23} \\ &= {}_{23}\langle p', q'; \alpha' | \hat{P}_{123} | p, q; \alpha \rangle_{23}, \end{aligned} \quad (2.15)$$

where $\hat{P}_{123} = \hat{P}_{23}\hat{P}_{123}\hat{P}_{23}$ was used. This follows similarly for the channel (12) and (13). Therefore, we have

$${}_{ij}\langle p', q'; \alpha' | \hat{A}_{123} | p, q; \alpha \rangle_{ij} = {}_{ij}\langle p', q'; \alpha' | \frac{1}{3} \left(\mathbb{1} + 2\hat{P}_{123} \right) | p, q; \alpha \rangle_{ij}, \quad (2.16)$$

meaning only one of the three-body permutation operators is of interest to acquire physically allowed three-body states, given partially antisymmetric NNN states. As derived explicitly in Paper II, the projection of the permutation operator in the (12) system can be written as

$${}_{12}\langle p' q'; \alpha' | \hat{P}_{123} | p q; \alpha \rangle_{12} = \int_{-1}^1 dx G_{\alpha\alpha'}(p', q', x) \frac{\delta(\bar{p} - p)}{\bar{p}p} \frac{\delta(\bar{q} - q)}{\bar{q}q}, \quad (2.17)$$

where $G_{\alpha\alpha'}(p', q', x)$ is the *geometric* function, containing complicated recoupling terms, and where \bar{p} and \bar{q} are defined from p' , q' , and x .

2.2 Two-nucleon scattering

In this section I will summarise the theory of two-nucleon scattering by presenting all steps required to evaluate Eq. (2.1), as well as the standard computational method used to solve the relevant equations. Then I will provide some benchmark calculations to document the convergence of the method, as well as highlight its computational bottleneck. This will serve as a benchmark for the WPCD-discussion in Chap. 3.

2.2.1 The spin-scattering matrix

As stated with Eq. (2.1), elastic spin observables can be calculated using the spin-scattering M -matrix. With two nucleons, the channel-spin we can measure is the total spin $\mathbf{S} \equiv \mathbf{s}_1 + \mathbf{s}_2$. The partial-wave expansion of the M -matrix is written here as [59]

$$\begin{aligned} M_{S'm_{S'}, S m_S}(\theta, p) &= \frac{\sqrt{\pi}}{ip} \delta_{S'S} \sum_{J,L,L'} i^{L'-L} \sqrt{2L+1} C_{S m_S, L 0}^{J m_S} C_{S m_{S'}, L'(m_S - m_{S'})}^{J m_S}, \\ &\quad \times (S_{L'L}^{S J} - \delta_{L'L}) Y_{L'}^{(m_S - m_{S'})}(\theta, 0) \end{aligned} \quad (2.18)$$

where $C_{j_1 m_1, j_2 m_2}^{j_3 m_3}$ are the Clebsch-Gordan coefficients, $Y_l^{m_l}$ are the spherical harmonics, and I assume antisymmetric NN states, which fulfil $-1 = (-1)^{L+S+T}$. The “ S -matrix” element, $S_{L'L}^{S'J}$, is the scattering probability amplitude between different channels in the initial and final scattering states. The S -matrix is given by a direct term plus an interactive term given by the “ T -matrix” element [59],

$$S_{L'L}^{S'J}(p', p; E) = \delta_{L'L} - 2\mu_0 p \pi i T_{L'L}^{S'J}(p', p; E). \quad (2.19)$$

The T -matrix is the solution to the LS equation. Obtaining T -matrix solutions is the most computationally demanding part in calculating NN observables. Therefore, understanding and solving the LS equation will be the focus in rest of this section.

2.2.2 The Lippmann-Schwinger equation

There are several ways to derive the LS equation that are introduced very pedagogically in, for example, Ref. [64]. Here, I will summarise one such approach based on operator identities, several of which will be relevant for the introduction of the WPCD method in Chap. 3.

The T -matrix elements are transition amplitudes between the asymptotic states of the scattering wave function at times $t = \pm\infty$, which are plane-wave states. The time-evolution of the scattering wave function is provided by the time-dependent Schrödinger equation. To work with the boundary of the wave function, i.e., the asymptotic states, we require the integral form of the Schrödinger equation. It can be shown that the Green’s operator, $\hat{G}(E)$, for on-shell energy E , equals the integral of a plane-wave scattering with potential \hat{v} for $t = \pm\infty$ [64]. The Green’s operator, for some complex value z , is defined

$$\hat{G}(z) \equiv (z - \hat{h})^{-1}, \quad (2.20)$$

where $\hat{h} \equiv \hat{h}_0 + \hat{v}$ is the full Hamiltonian and \hat{h}_0 is the free Hamiltonian. Knowing the Green’s operator for all z entails knowing the eigenspectrum of \hat{h} . This is because $\hat{G}(z)$ is non-analytic (singular) only when z equals eigenvalues E of \hat{h} . However, knowing the eigenspectrum is not normally feasible in the continuum since we normally cannot solve the Schrödinger equation analytically for nuclear potentials. Instead, unlike \hat{h} , the eigenspectrum of \hat{h}_0 is known to be plane-wave states. To replace \hat{h}_0 by \hat{h} , we introduce the following operator identity, also named the LS equation for $\hat{G}(z)$,

$$\hat{G}(z) = \hat{G}_0(z) + \hat{G}_0(z)\hat{v}\hat{G}(z), \quad (2.21)$$

where $\hat{G}_0(z) \equiv (z - \hat{h}_0)^{-1}$ is the *free* Green’s operator. This identity also works for $\hat{G}(z) \leftrightarrow \hat{G}_0(z)$. Another important quantity to introduce is the T -operator $\hat{t}(z)$, defined as

$$\hat{t}(z) \equiv \hat{v} + \hat{v}\hat{G}(z)\hat{v}. \quad (2.22)$$

From these relations one finds

$$\hat{t}(z)\hat{G}_0(z) = \hat{v}\hat{G}(z), \quad (2.23)$$

which is a useful relation for switching between the use $\hat{G}(z)$ and $\hat{G}_0(z)$. Note that the equations above will reappear in Chap. 3. Equation (2.22) is the operator form of the LS equation, meaning $\hat{t}(E)$ provides the T -matrix of Eq.(2.19). Note that another commonly used name for the Green's function is *resolvent*, which I will use hereafter.

Projecting Eq. (2.22) on the NN basis with states $|p; n\rangle$ gives

$$T_{n'n}(p', p; E) = v_{n'n}(p', p) + \sum_{n''} \int_0^\infty dk k^2 v_{n'n''}(p', k) g_0(k; E) T_{n''n}(k, p; E), \quad (2.24)$$

where $T_{n'n}(p', p; E) = T_{L'L}^{S'J}(p', p; E)$ is the same quantity used in Eq. (2.19), for $n' = \{(L'S)J, T, T_z\}$ and $n = \{(LS)J, T, T_z\}$. The LS equation is an inhomogeneous Fredholm type-II integral equation which can be solved with a Liouville-Neumann series, see e.g. Ref. [59]. However, this solution can also be achieved using matrix inversion [65].

Matrix-inversion method

The matrix-inversion (MI) method [65] is a highly accurate and precise method to find T -matrix elements, and is quite straightforward to implement in code. The starting point of the method is the quadrature approximation of the integral in Eq. (2.24),

$$T_{n'n}(p, p; E) = v_{n'n}(p, p) + \sum_{n''} \sum_{i=1}^{N_Q} w_i v_{n'n''}(p, k_i) g_0(k_i; E) T_{n''n}(k_i, p), \quad (2.25)$$

where k_i are the quadrature points and w_i the associated weights. Introducing matrix notation where, for example, the elements of the matrix $\mathbf{T}_{n'n}$ are defined as $[\mathbf{T}_{n'n}]_{ij} \equiv T_{n'n}(k_i, k_j; E)$, we can shorten the LS equation into,

$$\sum_{n''} \mathbf{F}_{n'n''} \mathbf{T}_{n''n} = \mathbf{V}_{n'n}, \quad (2.26)$$

where the “wave matrix” is given by

$$[\mathbf{F}_{n'n}]_{ij} \equiv \delta_{ij} \delta_{n'n} - [\mathbf{V}_{n'n}]_{ij} \mathbf{D}_j, \quad (2.27)$$

and where

$$\mathbf{D}_i \equiv \begin{cases} \frac{w_i k_i^2 m_N}{k_i^2 - p^2} & \text{if } i \leq N_Q, \\ -\sum_{i=1}^{N_Q} \frac{w_i p^2 m_N}{k_i^2 - p^2} + \frac{i\pi p m_N}{2} & \text{if } i = N_Q + 1. \end{cases} \quad (2.28)$$

Equation (2.26) is a straightforward matrix-inversion type problem where the last column or row of $\mathbf{T}_{n'n}$ contains the on-shell element $T_{n'n}(p, p; E)$. Note that direct matrix inversion is commonly not recommended due to numerical instability, and instead it is suggested to use algorithms such as Gaussian elimination or Cramer's rule for solving sets of linear equations [66].

In the context of computational solutions, it should be noteworthy that this method can also be used when replacing the T -matrix with a real-valued matrix defined by the principal-value kernel of the LS equation [59]. The form and complexity of the matrix inversion problem remains the same with the real-values matrix as for the T -matrix, but the lack of complex numbers reduces the number of required operations by a factor of 8, due to the $\mathcal{O}((N_Q + 1)^3)$ complexity of matrix-inversion type techniques.

2.2.3 Convergence of NN scattering solutions

There are several variables to consider in terms of convergence of NN observables. Specifically, we can change N_Q , the truncation $J \leq J_{\max}$ of the sum in Eq. (2.18), and the number of on-shell energies for which we calculate the T -matrix. Focusing on N_Q and J_{\max} , the convergence with respect to these parameters is shown Fig. 2.3 for neutron-proton (np) total cross section σ_{tot} . The benchmark, with $J \leq 30$ and $N_Q = 96$, is considered a converged calculation. The calculations were done using the chiral N2LO_{opt} potential [67]. The absolute relative errors, calculated as $\left| \frac{\sigma_i - \sigma_{i, \text{benchmark}}}{\sigma_{i, \text{benchmark}}} \right|$, show that for less than single-precision errors, i.e. 10^{-7} or less, $N_Q = 48$ and $J_{\max} = 20$ is sufficient. With a complexity cost scaling as $\mathcal{O}((N_Q + 1)^3)$ to solve the LS equation for a single T -matrix, this is a significant speedup compared to the benchmark calculation. This conclusion is much the same for the differential cross section, shown Fig. 2.4 at four different E_{Lab} , although generally with 1-2 orders of magnitude larger errors.

2.3 Three-nucleon scattering

Here, I start with a summary of the historical development of the Faddeev equations, focusing on elastic scattering with two-nucleon forces, followed by a mention on some computational challenges of solving the equations. I end the section by summarising an investigation of the bound-state Faddeev equations as a benchmark to apply NNN antisymmetrisation to the NNN partial-wave basis.

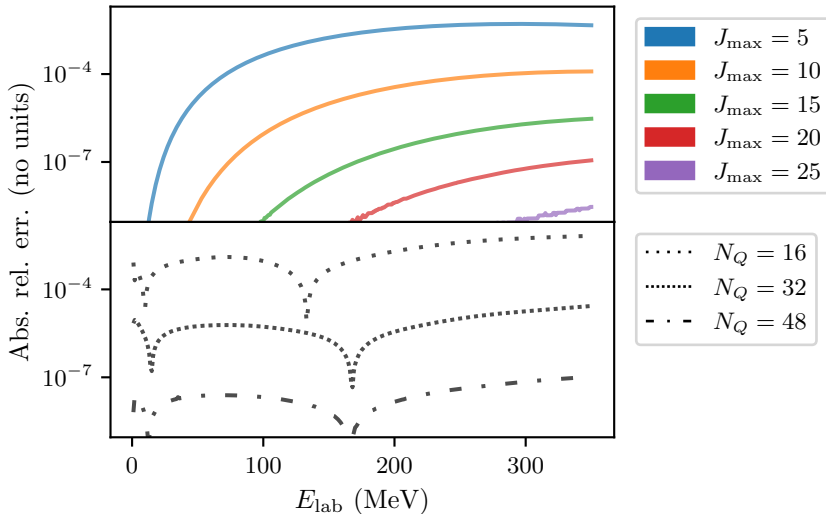


Figure 2.3: Convergence with J_{\max} (top panel) and N_Q (bottom panel) for the total np cross section relative a $J_{\max} = 30$, $N_Q = 96$ benchmark. Calculations were done using the $N^2\text{LO}_{\text{opt}}$ interaction.

2.3.1 The spin-scattering matrix

Focusing on elastic scattering, since the deuteron's quantum numbers remain fixed in the scattering process it is only possible for the spectator nucleon to affect the channel spin Σ . Therefore, a commonly used channel-spin definition is [62]

$$\Sigma \equiv \mathbf{J} + \mathbf{s}, \quad (2.29)$$

where the coupling order is $(Js)\Sigma$. With this, the spin-scattering matrix of Eq. (2.1) is given in a partial-wave expansion as [62, 68]

$$M_{\Sigma' m_{\Sigma'}, \Sigma m_{\Sigma}}(\theta, q) = \frac{\sqrt{\pi}}{iq} \sum_{\mathcal{J} l'} i^{l'-l} \sqrt{2l+1} C_{\Sigma m_{\Sigma}, l 0}^{\mathcal{J} m_{\Sigma}} C_{\Sigma' m_{\Sigma'}, l' (m_{\Sigma} - m_{\Sigma'})}^{\mathcal{J} m_{\Sigma}} \times \left(S_{l' \Sigma', l \Sigma}^{\mathcal{J}} - \delta_{\Sigma' \Sigma} \delta_{l' l} \right) Y_{l'}^{(m_{\Sigma} - m_{\Sigma'})}(\theta, 0), \quad (2.30)$$

which, of course, is almost identical in form to Eq. (2.18). Here, the S -matrix is defined with the Nd equivalent of the T -matrix, the U -matrix, as [69]

$$S_{l' \Sigma', l \Sigma}^{\mathcal{J}} = \delta_{l' l} \delta_{\Sigma' \Sigma} - 2\pi i q m_N i^{l'-l} U_{l' \Sigma', l \Sigma}^{\mathcal{J}}. \quad (2.31)$$

The remaining text is dedicated to determining the on-shell U -matrix elements using the elastic Faddeev equations.

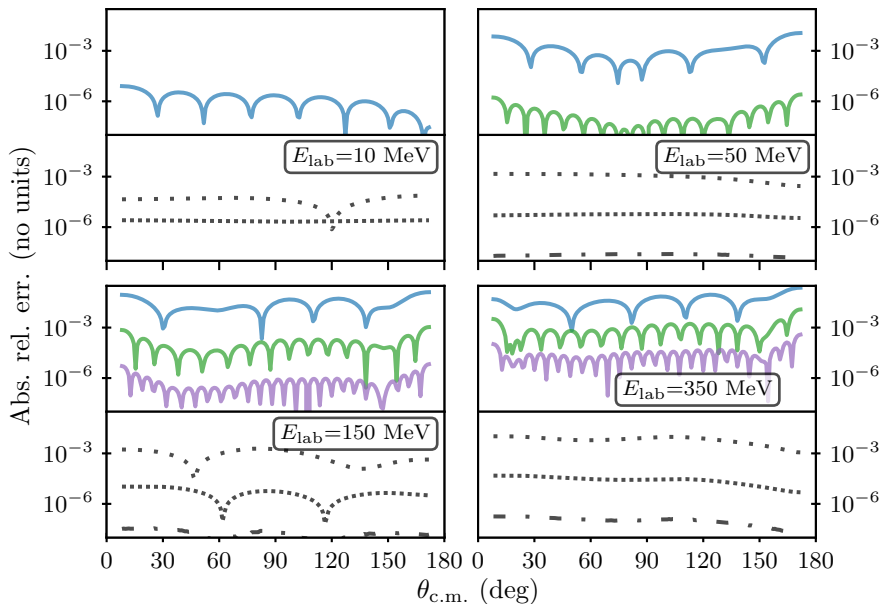


Figure 2.4: Convergence with J_{\max} (top halves) and N_Q (bottom halves) of the differential np cross section relative a $J_{\max} = 30$, $N_Q = 96$ benchmark, at four different scattering energies (annotated in panels). The calculation and figure legend is the same as in Fig. 2.3. The lines at $J_{\max} = 10$ and 20 have been omitted.

2.3.2 The Faddeev equations

The history of the Faddeev equations and the need for its formulation is summarised in, for example, Ref. [33]. In short, writing an LS equation for NNN scattering is problematic as it will turn out not to have a compact or connected kernel. As a counterexample, the kernels $\hat{v}\hat{G}(z)$ as well as $\hat{t}\hat{G}_0(z)$ in Eq. (2.22) are both compact and connected. It was shown by L. Faddeev in 1960 that this entails that the NNN LS equation does not have unique solutions [26]. Instead, Faddeev suggested a splitting of the NNN T -matrix into three components, T_i for $i = 1, 2$, and 3. Each T_i would be a *partial* solution. The coupled integral equations for the partial solutions are called the Faddeev equations for the T -matrix [58]. There were still many formal problems to be solved, summarised in, e.g., Ref. [58], but Faddeev had made a pivotal first step for a NNN scattering equation. In 1971, W. Glöckle derived what is today called the fundamental set

of LS equations, and that showed they provide unique solutions [70]. They can be written [33],

$$|\Psi_1^+\rangle = \delta_{i1}|\phi_1\rangle + \lim_{\epsilon \rightarrow 0} \hat{G}_i(E \pm i\epsilon)\hat{v}^1|\Psi_1^{(+)}\rangle, \quad (2.32)$$

where, using the odd-man-out notation where i is the channel where nucleon i is the spectator, E is the on-shell energy, $|\Psi_1^{(+)}\rangle$ is the scattering state in channel 1, $|\phi_1\rangle$ is the initial plane-wave state, and $\hat{G}_i(z) \equiv (z - \hat{h}_i)^{-1}$ with $\hat{h}_i \equiv \hat{h}_0 + \hat{v}_i$ being the channel Hamiltonian. Furthermore, $\hat{v}^i \equiv \hat{v}_j + \hat{v}_k$, for $i \neq j$ and $i \neq k$, is the sum of interactions between the spectator and the pair, assuming only NN interactions. His work presents a formalism that extends straightforwardly to general N -body scattering.

Besides this, in 1967, E. O. Alt, P. Grassberger, and W. Sandhas derived an equivalent set of equations for the scattering amplitudes, known as the Alt-Grassberger-Sandhas (AGS) equations [71]. These equations are what I will use to solve Nd scattering as they provide U -matrices for use in Eq. (2.31), i.e., transition amplitudes between asymptotic scattering states. Following Ref. [33], the important steps of the derivation are as listed below.

The scattering amplitude A_{i1} is defined as the probability of getting out an asymptotic final plane-wave state $|\phi_i\rangle$, and is written

$$A_{i1} = \langle \phi_i | \hat{v}^i | \Psi_1^{(+)} \rangle, \quad (2.33)$$

This amplitude can be expressed in terms of a transition operator, \hat{U}_{i1} , defined as

$$\hat{U}_{i1}|\phi_1\rangle \equiv \hat{v}^i|\Psi_1^{(+)}\rangle = (\hat{v}_j + \hat{v}_k)|\Psi_1^{(+)}\rangle. \quad (2.34)$$

Inserting Eqs. (2.32), this can be shown to give the AGS equations,

$$\hat{U}_{i1}|\phi_1\rangle = (1 - \delta_{i1})\hat{G}_0^{-1}|\phi_1\rangle + \hat{G}_i\hat{v}^i|\Psi_1^{(+)}\rangle + \sum_{j \neq i} \hat{t}_j \hat{G}_0 U_{j1}|\phi_1\rangle, \quad (2.35)$$

by using $\hat{v}_1|\phi_1\rangle = \hat{G}_0^{-1}|\phi_1\rangle$ and $\hat{v}_i\hat{G}_i \equiv t_i\hat{G}_0$, where t_i is the two-body T -matrix for pair-system i . However, the equations are not antisymmetric as written here.

In the partially-antisymmetric NNN basis introduced in Sec. 2.1.1, $|\phi_i\rangle$ are only antisymmetric in the pair-system i . Since $|\phi_i\rangle$ has an antisymmetric pair, a superposition of the three channels will be totally antisymmetric. Thus, the scattering state can be written

$$|\Psi^{(+)}\rangle = \sum_{i=1}^3 |\Psi_i^{(+)}\rangle \quad \text{and} \quad \hat{U}_i|\phi_1\rangle \equiv \sum_{k=1}^3 \hat{U}_{ik}|\phi_k\rangle, \quad (2.36)$$

where we define the transition operator \hat{U}_i for scattering into $|\phi_i\rangle$ from a fully antisymmetric scattering state. Inserting Eq. (2.35) gives,

$$\hat{U}_i|\phi_1\rangle = \sum_{k \neq i} \hat{G}_0^{-1}|\phi_k\rangle + \sum_{k \neq i} t_j \hat{G}_0 \hat{U}_j |\phi_1\rangle, \quad (2.37)$$

Using Eqs.(2.34) and (2.36), we can find that the transition amplitude is uniquely defined in terms of any one of the operators \hat{U}_i ,

$$\hat{U}_2|\phi_1\rangle = \hat{P}_{123}\hat{U}_1|\phi_1\rangle \quad \text{and} \quad \hat{U}_3|\phi_1\rangle = \hat{P}_{132}\hat{U}_1|\phi_1\rangle, \quad (2.38)$$

so Eq. (2.37) is written as (where I drop the odd-man-out notation),

$$\langle \phi' | \hat{U} | \phi \rangle = \langle \phi' | \hat{P} \hat{v} | \phi \rangle + \langle \phi' | \hat{P} \hat{v} \hat{G} \hat{U} | \phi \rangle, \quad (2.39)$$

where I inserted $\hat{G}_0^{-1} = \hat{v}$ and $\hat{t}\hat{G}_0 = \hat{G}\hat{v}$, and defined $\hat{P} \equiv 2\hat{P}_{123}$. Thus, solving this equation gives us *elastic* transition amplitudes. Note, however, that I have not included three-body forces or discussed breakup channels here, but the theory of both is well documented in for example Ref. [33].

Despite the compact form, this equation bears some computational challenges:

- For converged scattering observables, typically one can expect to have to use $N_p \simeq 30$ and $N_q \simeq 40$ momentum quadrature points for the p and q momenta, respectively, and up to $N_\alpha \simeq 60$ partial-wave states is required per $\Gamma = \{\mathcal{J}, \mathcal{P}\}$ channel for $\mathcal{J} \leq \frac{17}{2}$ with $J \leq 3$ [33]. This entails matrix dimensions $N \times N$ of 72000×72000 , requiring around 38 gibibytes (GiBs)² of computer memory using double floating-point precision *per matrix*. This mostly renders MI-type methods too costly to solve Eq. (2.39). Instead, one can use a Liouville-Neumann series, see for example Ref. [59]. In WPCD, the number of required p and q wave packets is even greater, as I will show with the convergence of observables in Chap. 3 in a wave-packet basis.
- The singularities arising in the resolvent \hat{G}_0 in the second term of Eq. (2.39), acquired by using $\hat{t}\hat{G}_0 = \hat{v}\hat{G}$, are referred to as “moving” singularities [58]. They arise from the momentum restrictions imposed by permutation operator, seen in Eq. (2.17). See e.g. Ref. [72] for a modern, computationally-oriented treatment of the singularities. In the WPCD method, these singularities are solved analytically, which is one of the strengths of the method, as I will discuss in Chap. 3.

²The standardised denotation “gigabyte”, or GB, is 1000^3 bytes, while a GiB is 1024^3 bytes. The latter is more suitable for computers as they operate with binary numbers.

- The momentum restrictions imposed by the permutation operator can also impose momentum restrictions on the \hat{t} operator, again by using $\hat{t}\hat{G}_0 = \hat{v}\hat{G}$. This displaces the usual quadrature-mesh on which the T -matrix is usually acquired from solving the LS equation. An effective treatment for this displacement is through the use of a spline-basis [73]. In the WPCD method, the permutation operator is calculated in closed form and imposes no momentum restrictions on neighbouring operators.

There problems arising from these challenges have all been worked out in currently used methods, but we will see that in the WPCD method some of them are solved inherently. Of the operators appearing in Eq. (2.39), the permutation operator is especially difficult to implement without error due to the complexity of the geometric function, shown explicitly in Eq. (A13) of Paper II. This is where the bound-state Faddeev equations serves as a useful benchmark due to its simplicity relative to the AGS equations.

2.3.3 Benchmarking the permutation matrix

The three-body bound state is simpler to define uniquely due the lack of asymptotic boundary conditions. Additionally, the lack of on-shell energy-dependent singularities in the Faddeev equations makes it easier to implement computationally. It can be shown that in the case of three-body bound-state systems with energy $E < 0$ and only two-body interactions, the total antisymmetric wave function $|\Psi\rangle$ is given by [74]

$$|\psi_i\rangle = \hat{G}_0 \hat{t}_i(E) \hat{P} |\psi_i\rangle, \quad (2.40)$$

through $|\Psi\rangle = \sum_{i=1}^3 |\psi_i\rangle$, where $|\psi_i\rangle$ are referred to as the Faddeev amplitudes. In a partial-wave projection, this becomes

$$\begin{aligned} \langle pq; \alpha | \psi \rangle_{ij} = & \frac{2}{E - \frac{p^2}{2\mu_0} - \frac{q^2}{2\mu_1}} \sum_{\alpha' \alpha''} \int_0^\infty dp' p'^2 t_{nn'} \left(p, p'; E - \frac{q^2}{2\mu_1} \right) \\ & \times \int_{-1}^{+1} dx G_{\alpha' \alpha''}(p', q', x) \langle \bar{p} \bar{q}; \alpha'' | \psi \rangle_{ij}, \end{aligned} \quad (2.41)$$

where I have explicitly inserted the permutation operator from Eq. (2.17). To solve this equation, we realise that Eq. (2.40) can be written

$$|\psi_i\rangle = \hat{K}(E) |\psi_i\rangle, \quad (2.42)$$

where $\hat{K}(E)$ follows obviously. Solving this equation is done usually by guessing at values for E and checking if the ensuing state $|\psi_i\rangle$ is self-consistent. Due to the uniqueness Faddeev amplitudes, this approach is guaranteed to provide the

correct energy E . Mathematically, this approach can be written as an eigenvalue problem,

$$\hat{K}(z)|\psi_i(z)\rangle = \lambda(z)|\psi_i(z)\rangle, \quad (2.43)$$

where we find which $z \in \mathbb{R}^-$ satisfies $\lambda(z) = 1$. It is noteworthy that $\lambda(z)$ will be largest when $z = E$ is the “physical” value [75]. This is quite useful when one resorts to Lanczos algorithms to numerically determine eigenvalues of \hat{K} since these algorithms usually iteratively converge first on the largest and smallest eigenvalues [76]. However, for benchmarking, we can afford to numerically diagonalise \hat{K} using direct matrix diagonalisation routines on modern desktop computers. This is because ${}^3\text{H}$, which was of focus for benchmarking due to lack of Coulomb forces, exists in the state $\mathcal{J}^\Pi(\mathcal{T}) = \frac{1}{2}^+ \left(\frac{1}{2}\right)$ where only about $N_\alpha \sim 25$ is required for converged results for E .

A pivotal part of this work consisted of benchmarking a computational implementation of Eq. (2.41). This test would ensure a consistent use of geometrical couplings in all operator expressions required for an Nd scattering code. As input for this implementation I used a pre-developed code [17, 77] for calculating the permutation matrix in a NNN basis, and the Idaho-N3LO potential [78]: a fourth-order $\chi\text{EFT } NN$ -only interaction fitted to NN scattering data. The resulting benchmarking is summarised in Tab. 2.4, where we see perfect agreement between an external, bound-state code [77] and my own. I also show additional benchmark calculations. With consistent use of geometrical coupling confirmed, meaning the operators of Eq. (2.43) are well-understood in the NNN partial-wave basis defined earlier, a large source of error is removed when attempting an Nd scattering code, which will be discussed in the next chapter.

Table 2.4: Bound-state energies for ${}^3\text{H}$ predicted for the Idaho-N3LO potential [78], using $N_p = 32$ and several combinations of J and N_q , by solving Eq. (2.43). For each combination, I also show the highest eigenvalue, λ , of the kernel $\hat{K}(z)$ in Eq. (2.43) for several proposed energies z . When $\lambda = 1$ we retrieve $E_b = z$. Here, I extract E_b using cubic polynomial interpolation conditioned on my calculated λ to determine where $\lambda = 1$. Benchmark calculations were provided in Ref. [77]. Reference [78] predicts $E_b = 7.855$ MeV with $J \leq 4$ (giving 34 channels).

J_{\max}	N_q	E_b (MeV)	E_b (MeV) [77]	z	λ	λ [77]
1	10	-7.4282	-7.429	-7.0	1.02713	
				-7.5	0.99566	
				-8.0	0.96695	
				-8.5	0.94062	
				-9.0	0.91633	
	20	-7.6605	-7.661	-7.0	1.04215	
				-7.5	1.00976	
				-8.0	0.98027	
				-8.5	0.95323	
				-9.0	0.92829	
	30	-7.6705	-7.671	-7.0	1.04289	1.0429
				-7.5	1.01039	1.0104
				-8.0	0.98082	0.9808
				-8.5	0.95371	0.9537
				-9.0	0.92871	0.9287
2	10	-7.5910	-7.592	-7.0	1.03678	
				-7.5	1.00540	
				-8.0	0.97679	
				-8.5	0.95055	
				-9.0	0.92636	
	20	-7.8240	-7.825	-7.0	1.05164	
				-7.5	1.01935	
				-8.0	0.98995	
				-8.5	0.96301	
				-9.0	0.93816	
	30	-7.8338	-7.834	-7.0	1.05237	1.0524
				-7.5	1.01997	1.0200
				-8.0	0.99050	0.9905
				-8.5	0.96348	0.9635
				-9.0	0.93858	0.9386

Chapter 3

Wave-packet continuum discretisation

Wave-packet continuum discretisation [52, 79–85] is a quadrature-type method for calculating observables in the scattering continuum, bearing similarities to bound-state methods. The method builds in part on the concepts of pseudostates and eigendifferentials, which combined are named pseudostate eigendifferentials. I leave these concepts to App. A. Wave packets can be used to construct an approximate basis for the eigenstates of the full Hamiltonian. Knowing the eigenspectrum allows us to analytically evaluate the full resolvent, which can significantly simplify the scattering equations shown in Chap. 2.

The method is summarised in Ref. [51], parts of which I will cover in the first two sections of this chapter. I will go through the formalism of wave packets by first defining a wave packet followed by deriving approximate scattering states. After this introduction, I show how the LS and Faddeev equations look in a wave-packet basis, how they can be efficiently solved on a computer, and their convergence patterns. These last points present the outcomes of Papers I and II for NN and NNN scattering, respectively.

3.1 The wave-packet basis

A wave packet is defined a normalised integral of continuum states over some finite interval referred to here as a “bin”. Depending on the type of continuum state, we can have different wave packets. I define a free wave packet (FWP) $|x_i\rangle$ as an integral of plane-wave states $|p\rangle$ over the bin $\mathcal{D}_i \equiv [k_i, k_{i+1}]$, i.e.

$$|x_i\rangle \equiv \frac{1}{\sqrt{N_i}} \int_{\mathcal{D}_i} dp p f(p) |p\rangle, \quad (3.1)$$

Table 3.1: Wave-packet variables and eigenvalues for both momentum and free Hamiltonian operators in the two-body system, for both momentum and energy wave packets, illustrating that these two kinds of wave packets do not have equal eigenvalues. Note that $E_i = \frac{k_i^2}{2\mu}$.

Quantity	Energy wave packets	Momentum wave packets
$f(p)$	$\sqrt{\frac{p}{\mu}}$	1
Width	$\Delta E_i \equiv \frac{k_{i+1}^2}{2\mu} - \frac{k_i^2}{2\mu}$	$\Delta k_i \equiv k_{i+1} - k_i$
N_i	ΔE_i	Δk_i
e_i	$E_i + \frac{1}{2}\Delta E_i = \frac{k_{i+1}^2}{2\mu} + \frac{k_i^2}{2\mu}$	$\frac{k_{i+1}^2 + k_{i+1}k_i + k_i^2}{6\mu}$
p_i	$\frac{2}{3} \frac{k_{i+1}^2 - k_i^2}{k_{i+1} - k_i}$	$k_i + \frac{1}{2}\Delta k_i$

where N_i is the normalisation constant, k_i are momenta, and $f(p)$ is a weighting function. Furthermore, I denote the kinetic energy and momentum eigenvalues as $\hat{h}_0|x_i\rangle = e_i|x_i\rangle$ and $\hat{p}|x_i\rangle = p_i|x_i\rangle$,

The weighting function determines whether we use the momentum operator \hat{p} as the defining operator for our basis or the free Hamiltonian \hat{h}_0 . We can switch the type of FWP, named ‘‘momentum’’ and ‘‘energy’’ FWPs, by letting $f(p) = 1$ or $f(p) = \sqrt{\frac{p}{\mu}}$, respectively. We must distinguish the two because whereas plane-wave states are eigenstates of both \hat{p} and \hat{h}_0 , an FWP is not. This can be seen in Tab. 3.1 where widths, weights, and eigenvalues of the two types of FWP are shown. Since the widths ΔE_i and Δk_i are not the same between the two types, the eigenvalues are not the same, meaning they are not equal FWPs.

Using the identity operator in the FWP basis, $\mathbb{1} \equiv \sum_{i=1}^{\infty} |x_i\rangle\langle x_i|$, one can show that the usual plane-wave expectation value of an arbitrary operator \hat{O} is given approximately in an FWP basis as

$$\langle q'|\hat{O}|q\rangle \approx \frac{f(q)f(q')}{\sqrt{N_i N_j}} \frac{1}{q'q} \langle x_i|\hat{O}|x_j\rangle \mathbb{1}_{\mathcal{D}_i}(q') \mathbb{1}_{\mathcal{D}_j}(q), \quad (3.2)$$

where $\mathbb{1}_{\mathcal{D}_i}(q')$ is the indicator function. Of course, we can now replace \hat{O} by for example \hat{t} or \hat{U} for scattering. While it may seem intuitive that a wave-packet basis provides an approximate treatment of the continuum, it can be shown formally that the quality of the approximation depends purely on the bin width in the sense that narrowing the bins provide better approximations systematically. I summarise a proof from Ref. [51] in App. A. Note that in calculated observables there is negligible difference between momentum and energy FWPs, but it can be easier to calculate analytical expressions in one than the other.

3.2 Approximate scattering states

The real strength of the WPCD method lies in approximating scattering states, meaning we can approximate positive-energy eigenstates of the full Hamiltonian \hat{h} . We approximate by finding the wave-packet eigendecomposition of the Hamiltonian by diagonalisation in a FWP basis,

$$[\mathbf{H}]_{ij} \equiv \langle x_i | \hat{h} | x_j \rangle = [\mathbf{C} \mathbf{D} \mathbf{C}^T]_{ij} \quad (3.3)$$

where¹ $[\mathbf{D}]_{ij} \equiv \delta_{ij} \epsilon_i$ is diagonal with eigenvalues ϵ_i of \hat{h} and $[\mathbf{C}]_{ij} \equiv \langle x_i | z_j \rangle$ are the transformation coefficients of the associated eigenvectors $|z_i\rangle$ into the FWP basis. The eigenvectors are approximate scattering states and are referred to here as scattering wave packets (scattering wave packet (SWP)s). Note that for a realistic NN Hamiltonian there is only one case of $\epsilon_i < 0$, in the deuteron channel, and that otherwise we have $\epsilon_i > 0$.

From the positive-energy eigenspectrum above I define a SWP similarly to FWPs in Eq. (3.1),

$$|z_i\rangle \equiv \frac{1}{\sqrt{N_i}} \int_{\mathcal{D}_i} dp p f(p) |\psi(p)\rangle, \quad (3.4)$$

where $|\psi(p)\rangle$ are unknown, continuum eigenstates of the full Hamiltonian. If our operators acting on $|z_i\rangle$ depend solely on the full Hamiltonian, we only need to know the bin boundaries \mathcal{D}_i and weighting function $f(p)$, while $|\psi(p)\rangle$ is irrelevant. I will reserve \mathcal{D}_i for FWPs outside of this section. Since SWPs are Hamiltonian eigenstates, they are automatically energy wave packets with $f(p) = \sqrt{\frac{p}{\mu}}$. The boundaries will need to be extracted from the eigenvalues ϵ_i , and must be done such that the eigenenergies are obtained according to Tab. 3.1, i.e. $\epsilon_i = \mathcal{E}_i + \frac{1}{2} \Delta \mathcal{E}_i$, where \mathcal{E}_i is are the bin boundaries such that $\mathcal{D}_i = [\mathcal{E}_i, \mathcal{E}_{i+1}]$. For this, I use an approximate algorithm [86],

$$\mathcal{E}_1 \equiv 0, \quad \mathcal{E}_i \equiv \frac{1}{2} (\epsilon_{i-1} + \epsilon_i), \quad \mathcal{E}_{N_{\text{WP}}+1} \equiv \epsilon_{N_{\text{WP}}} + \frac{1}{2} (\epsilon_{N_{\text{WP}}} - \epsilon_{N_{\text{WP}}-1}). \quad (3.5)$$

where N_{WP} is the size of the FWP and SWP bases, and where $N_{\text{WP}} < \infty$ introduces finiteness as needed for computations. Here I assume $\epsilon_{i-1} < \epsilon_i$. In the case of bound states, where a vector $|z_i\rangle$ of \mathbf{C} corresponds to an eigenenergy $\epsilon_i < 0$, the treatment above still works by incrementing the lowermost index in Eq. (3.5) by the number of bound states.

In the case of coupled NN channels such as ${}^3\text{S}_1$ - ${}^3\text{D}_1$, the Hamiltonian diagonalisation in will return eigenstates ϵ_i^κ where κ indexes the coupled state, i.e. either ${}^3\text{S}_1$ or ${}^3\text{D}_1$. To define boundaries for ${}^3\text{S}_1$ and ${}^3\text{D}_1$ separately using

¹This matrix must not be confused with the vector \mathbf{D} of Eq. (2.27).

Eq. (3.5), it is necessary to distinguish ϵ_i^κ from $\epsilon_i^{\kappa'}$ for $\kappa \neq \kappa'$. As was discussed more extensively in Paper I, the eigenstates can be disentangled using [84],

$$\epsilon_i^{\kappa-1} \leq \epsilon_i^\kappa. \quad (3.6)$$

Thus, for a coupled-channel Hamiltonian diagonalisation, we can sort the eigenvalues in ascending order, and use that odd-indexed eigenvalues belongs to one channel while even-indexed values belong to the other. Of course, the corresponding eigenstates must be sorted accordingly. To reflect this sorting, I introduce explicit channel-indexing $\mathbf{C}_{n'n}$, as defined in Sec. 2.2.2, where $[\mathbf{C}_{n'n}]_{ij} \equiv \langle x_i^{n'} | z_j^n \rangle$ and $|x_i^{n'}\rangle$ is the FWP basis used for $|n'\rangle$. However, I distribute all FWPs equally and will mostly drop the state-indexing to write $|x_i\rangle$.

3.3 The Lippmann-Schwinger equation in WPCD

Much of the formalism covered here was presented in Paper I, and is a brief presentation of the WPCD review of the LS equation in Ref. [51]. Having constructed an FWP basis $\{|x_i\rangle\}_{i=0}^{N_{\text{WP}}}$ and a SWP basis $\{|z_i^n\rangle\}_{i=0}^{N_{\text{WP}}}$ for all NN -channels ($n'n$) with transition matrices $\mathbf{C}_{n'n}$, we can project Eq. (2.22) to an FWP basis as follows

$$\begin{aligned} \langle x_i | \hat{t}_{n'n}(E) | x_j \rangle &= \langle x_i | \hat{v}_{n'n} | x_j \rangle + \sum_{n''} \sum_{k=1}^{N_{\text{WP}}} \langle x_i | \hat{v}_{n'n''} | z_k^{n''} \rangle \langle z_k^{n''} | \hat{G}(E) | z_k^{n''} \rangle \\ &\quad \times \langle z_k^{n''} | \hat{v}_{n''n} | x_j \rangle. \end{aligned} \quad (3.7)$$

The remarkable property of the WPCD method is that we can now analytically derive the full resolvent in the SWP basis, and that all singularities of the operator are averaged out. The resolvent, and the remaining terms of this equation, were derived in Paper I. I can now introduce matrices with matrix elements defined as

$$\begin{aligned} [\mathbf{V}_{n'n}]_{ij} &\equiv \langle x_i | \hat{v}_{n'n} | x_j \rangle, \\ [\mathbf{G}_{n'n}(E)]_{ij} &\equiv \delta_{ij} \delta_{n'n} \langle z_i^{n'} | \hat{G}(E) | z_j^n \rangle, \\ [\tilde{\mathbf{V}}_{n'n}]_{ij} &\equiv \sum_{n''} \mathbf{V}_{n'n''} \mathbf{C}_{n''n}, \end{aligned} \quad (3.8)$$

such that the LS equation can be written in matrix form,

$$\mathbf{T}_{n'n}(E) = \mathbf{V}_{n'n} + \sum_{n''} \tilde{\mathbf{V}}_{n'n''} \mathbf{G}_{n''n''}(E) \tilde{\mathbf{V}}_{n''n}^T. \quad (3.9)$$

This equation is trivial to solve using standard matrix multiplication routines such as those contained in BLAS [87]. However, the WPCD method has a unique property can be used to significant computational advantage here: its inherent parallelism.

3.3.1 Solving the LS equation in parallel

To utilise the parallelism of the WPCD method it is easiest to focus on only the on-shell T -matrix elements of Eq. (3.9),

$$[\mathbf{T}_{n'n}(E_k)]_{ii} = [\mathbf{V}_{n'n}]_{ii} + \sum_{n''} \sum_{j=1}^{N_{\text{WP}}} [\tilde{\mathbf{V}}_{n'n''}]_{ij} [\mathbf{G}_{n''n''}(E_k)]_{jj} [\tilde{\mathbf{V}}_{n''n}^T]_{ji}, \quad (3.10)$$

where $E_k \in \mathcal{D}_i$ is one energy in a set of energies $\{E_k\}_{k=1}^{n_E}$ for which we wish to calculate the T -matrix. This equation is essentially the element-wise product of two arrays, followed by a vector-vector inner-product, surmounting to a total computational complexity that scales linearly with N_{WP} and n_E . With n_E processors at hand, like in a GPU, one can calculate all scattering energies simultaneously.

In Fig. 3.1 I show the theoretical complexity models derived in Paper I for the MI method² and both the sequential and parallel implementations of the WPCD method. These models contain all steps involved in the three approaches, including, e.g., the Hamiltonian diagonalisation cost. It is apparent that whereas the MI complexity has a heavier cost with n_E , the parallel WPCD method is at least two orders of magnitude less expensive to execute for $p = 1024$ processing threads. To access such a large number of threads, one can use a GPU [53]. These processing units have many more threads than the usual central processing unit (CPU). I will discuss the use of a GPU in the next section.

An important consideration of the WPCD method concerns where E lands within the FWP boundaries. In my studies I have found that the WPCD method provides worse approximations of observables $\langle \hat{O}(E) \rangle$ when $E \in \mathcal{D}_i$ falls far from the bin mid-points e_i (see Tab. 3.1). This likely occurs due to the averaging of operators in the continuum when we project on a wave-packet basis. In Ref. [51], it is argued that a smoothly varying E is not well-motivated in the WPCD method, and one should instead average the T -matrix with respect to E within the bin \mathcal{D}_i . In Paper I, we used such energy averaging. With a discrete energy resolution in the output of T -matrix elements, I simply employ linear interpolation from bin-midpoints to calculate scattering observables at any energy E .

²See Sec. 2.2.2 for a discussion on the MI method.

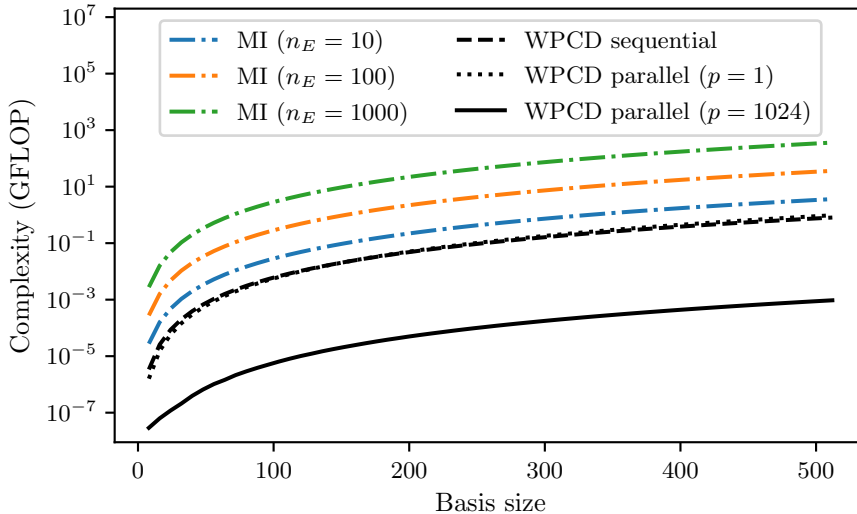


Figure 3.1: Estimated complexities of WPCD (MI) method for solving the LS equation as a function of the basis size N_{WP} (N_{Q}) for n_E scattering energies. Here, p is the number of processing threads used in the parallel calculation. Note that in the WPCD method we calculate $n_E = N_{\text{WP}}$ energies. The complexity models used are shown in Paper I.

3.3.2 Some considerations in utilising a GPU

Much of Paper I was dedicated to documenting the efficiency a GPU can offer in solving the WPCD LS equation, using a detailed comparison with the MI method. The study provided much insight into the handling of a GPU and how hardware layout, if not considered, can severely impact performance. In this section I will summarise these findings.

A GPU is in essence a computer processing unit with several times more FP32 units than a CPU³. An FP32 unit is a single part of a chip that can, in a single clock cycle, multiply two 32-bit floating-point numbers and add another on the form $a \times b + c$. It may be interesting to mention that, e.g., typical BLAS matrix-matrix multiplication routines also work with this format, i.e. $\mathbf{A} \times \mathbf{B} + \mathbf{C}$, which is written to fully utilise the efficiency of the FP32 units. A GPU is designed with a focus on throughput rather than computing rate, i.e., high clock frequency, which is a design principle that works well with parallel

³It is common to speak of computing “cores” rather than FP32 units. However, this is an ill-advised terminology to use for GPU-CPU comparison as their cores differ in many key aspects from a computing-power point of view.

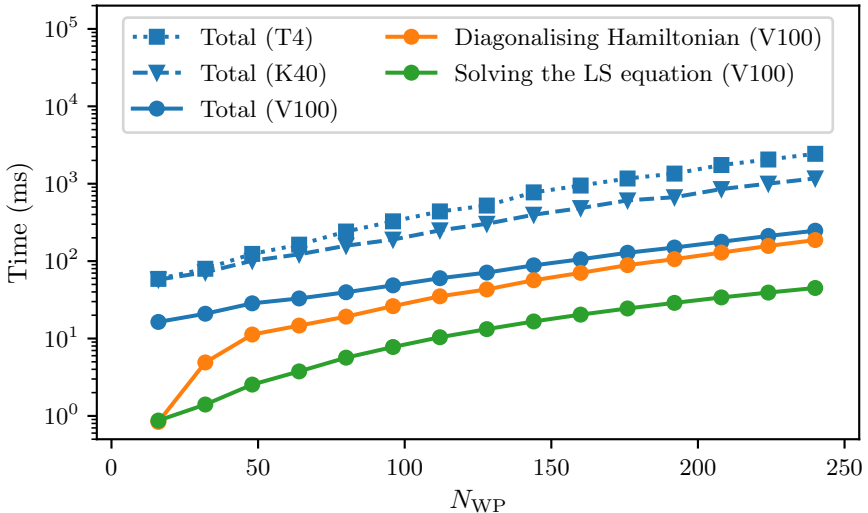


Figure 3.2: Total runtimes of the parallel WPCD-LS implementation versus wave-packet basis size, for three different GPUs ([91–93]) with decomposition of runtime for the V100 GPU. The omitted overhead for the V100 total runtime accounts for, e.g., potential matrix construction and calculation of observables.

algorithms. See for example Ref. [88] for a pragmatic study into the capabilities of a modern GPU, and Ref. [89] for an introduction to GPU programming and architecture. In my implementation I used the CUDA interface [90] for programming Nvidia GPUs.

Figure 3.2 shows the time spent by three different GPUs on solving Eq. (3.10) for $J \leq 30$, using a CUDA-based implementation for utilising Nvidia GPUs. It is clear that the majority of the time is spent diagonalising the NN Hamiltonian matrix (Eq. (3.3)). This is because the diagonalisation has a complexity cost scaling as $\mathcal{O}(N_{WP}^3)$, while solving the LS equation and other overheads of the algorithm are far cheaper.

Focusing on the Hamiltonian diagonalisation in Fig. 3.2, there is a different trend in time usage below $N_{WP} = 50$. The two data points, shown at $N_{WP} = 16$ and $N_{WP} = 32$ in the figure, are different due to the size of on-chip memory in the GPU. A GPU, like a CPU, has memory caches available on the chip. These caches are usually 64 kiB big and are typically ~ 100 faster for the computing units in the chip to access. With 64-bit precision, the Hamiltonian matrix requires $32^2 \times 64 \text{ b} = 8 \text{ kiB}$ to be stored and thus fit on the chip for $N_{WP} = 32$. Due to coupled channels, however, we also get 64^2 -size matrices. At $N_{WP} = 48$

we get uncoupled channels that fit on-chip and coupled channels that do not, which explains the non-linear transition between $N_{\text{WP}} = 16$ and $N_{\text{WP}} = 48$. The on-chip memory-size dependency brings to light that one must take care to efficiently utilise the loaded memory on-chip before disregarding it. This applies to CPUs as well, but it is more important to consider in GPU efficiency due to the massive read-write accesses to the GPU global memory from parallel-running threads, and the lower clock rate increasing random-access time to the global memory.

3.3.3 Convergence of the WPCD method for NN scattering

There are two WPCD method parameters that affect convergence in the evaluation of the T -matrix, N_{WP} and the number of quadrature points used to integrate potential matrix elements within a bin, N_k . I typically find convergence already at $N_k \sim 10$. I will therefore focus on the convergence with N_{WP} in this section, and its balance with computational performance.

First, however, I mention the choice of distribution of the FWP boundaries k_i from Eq. (3.1). I have used a Chebyshev distribution $\{x_i\}_{i=1}^n$, generally written as [51, 85]

$$x_i = s \tan^t \left(\frac{2i-1}{4N_{\text{WP}}} \pi \right), \quad i = 1, \dots, n, \quad (3.11)$$

where t is the sparseness degree and s is a scaling factor. This distribution focuses the boundaries on a close region around s , as a function of t , while providing grid points towards zero and infinity. Smaller t provide a denser mesh around s , giving sparser layouts of boundaries in the asymptotic regions. To avoid excessive tuning of t and s to any specific potential, I set $t = 2$ and $s = 100$ MeV for all potentials used for NN scattering in this work. Here, as in Paper I, I use momentum FWPs with $p_i = x_i$. As I will show, these choices provide accurate results in the range $N_{\text{WP}} \sim \mathcal{O}(10) - \mathcal{O}(10^2)$.

The convergence of the total np cross section with N_{WP} is shown in Fig. 3.3, in the same style as Fig. 2.3, using the N2LO_{opt} potential [67]. Already at $N_{\text{WP}} \sim 32$ is convergence reached to within one percent of the MI-method benchmark for most energies. However, it is clear that the WPCD method has a very slow convergence beyond this. With a sixteen-fold increase in basis size, to $N_{\text{WP}} = 512$ from $N_{\text{WP}} = 32$, we only improve convergence by a factor of roughly 10. Regardless of the slow convergence, as an approximative method the WPCD method works well, with results that converge towards the plane-wave results of the MI-method as $N_{\text{WP}} \rightarrow \infty$.

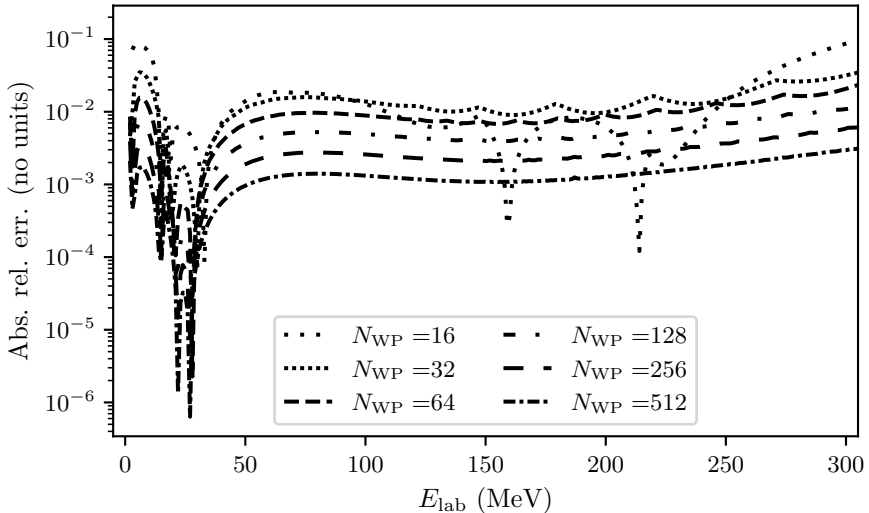


Figure 3.3: Convergence with N_{WP} for the total np cross section relative a MI-method benchmark with $J_{\text{max}} = 30$, $N_Q = 96$. Calculations were done using the $\text{N}2\text{LO}_{\text{opt}}$ potential.

Performance

As discussed in Chap. 1, I focus on the WPCD method as a means of ameliorating statistical inference. It is apparent from the discussion above that the WPCD method implemented on a GPU is efficient in NN scattering. Efficiency besides, however, I will in this section focus on the speed of the parallel WPCD method implemented on a GPU versus an efficient implementation on the CPU of the MI method [94]. Note that the convergence of the MI method was documented in Sec. 2.2.3.

Due to the slow convergence of the WPCD method, it is reasonable to expect its advantage to be when high accuracy is not needed. The necessary accuracy is determined by uncertainty; theoretical model uncertainty and experimental data uncertainty. If the method inaccuracy is comparably low, we are free to reduce method accuracy to increase computational speed. Thus, Paper I was focused on how the WPCD and MI methods compare in speed at a given level of accuracy. We used the root-mean square error (RMSE) of the total np cross section, with a benchmark calculated using the MI method with $N_Q = 96$ and $J \leq 30$, as a measure of the accuracy level.

Figure 3.4 shows an adaptation of Fig. 8 in Paper I focusing on the full energy region $E_{\text{Lab}} \in (0, 350]$ MeV. Just as interpolation can be used between FWP

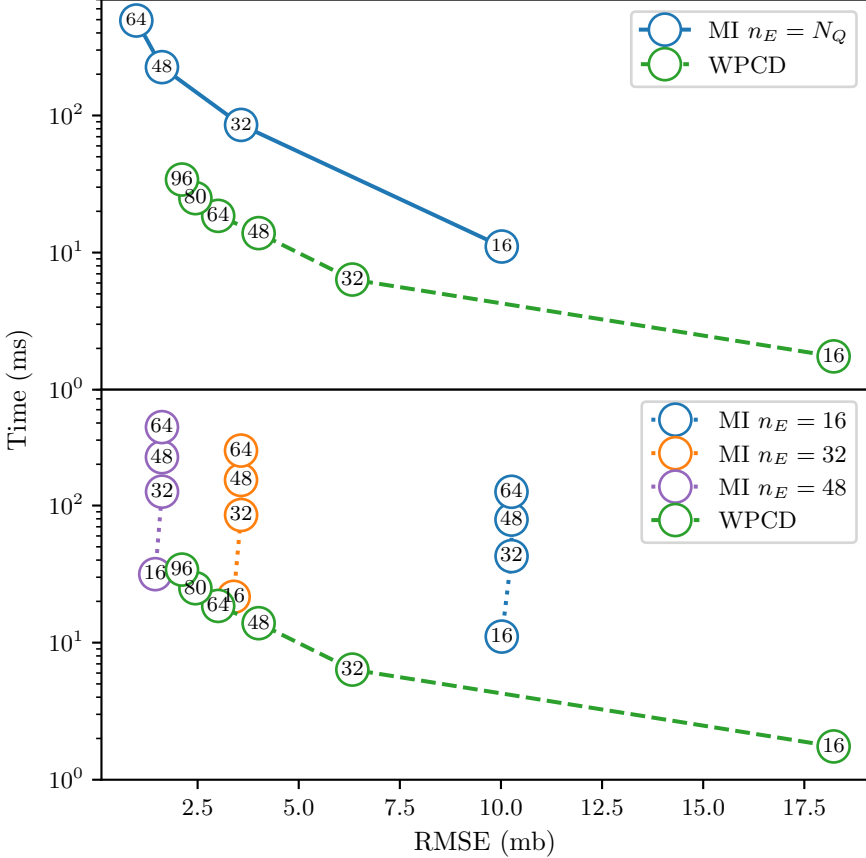


Figure 3.4: Performance of the WPCD GPU-implementation versus an efficient implementation [94] of the MI method, shown by comparing the time spent solving the LS equation against the RMSE of the total np cross section for $E_{\text{Lab}} \in (0, 350)$ MeV. Top panel: The markers contain the value of N_{WP} (N_Q) used for WPCD (MI), with n_E set equal the basis size. Bottom panel: Same as top panel but with n_E fixed at different values for the MI method (see legend). Calculations were done with the $N^2\text{LO}_{\text{opt}}$ potential.

midpoints, interpolation can be used for calculated MI solutions at n_E points. The figure shows results with n_E set⁴ both equal N_Q , as well as set freely, with

⁴The energies were distributed on the FWP midpoints gotten from a $N_{\text{WP}} = n_E$ Chebyshev distribution. This placed the predictions of the two methods at equal scattering energies,

phase-shift linear interpolation used to extract all energies in $E_{\text{Lab}} \in (0, 350]$ MeV. When setting $N_Q = n_E$, the WPCD GPU-implementation outperforms the MI method except for at very low RMSEs of the total cross section. Setting n_E freely, however, we see that the MI method is faster only for $\text{RMSE} \lesssim 2\text{-}4$ mb, which makes WPCD advantageous for $\text{RMSE} \gtrsim 4$ mb. This was interesting since a recent analysis of χEFT truncation errors in NN scattering predictions lay at about 5 mb at 95% degree-of-belief (DoB) [28]. The exact region of advantage for WPCD depends on the studied potential, but the conclusion remains the same: WPCD is a faster method than MI if some inaccuracy is acceptable.

3.4 The Faddeev equations in WPCD

The Faddeev equations project onto a wave-packet basis using the same approach as in the LS equation, but it is necessary to first define NNN wave-packet states $|X_{ij}\rangle$. Using the three-body formalism from Sec. 2.1, we define the wave-packet equivalent of $|p, q\rangle$ as

$$|X_{ij}\rangle \equiv |x_i\rangle \otimes |\bar{x}_j\rangle, \quad (3.12)$$

where both $|x_i\rangle$ and $|\bar{x}_j\rangle$ are defined as in Eq. (3.1). Here, $|x_i\rangle$ corresponds to the pair-system momentum $|p\rangle$, and $|\bar{x}_j\rangle$ to $|q\rangle$. Throughout this text I reserve the bar-notation to distinguish the two. We can insert and get

$$|X_{ij}\rangle = \frac{1}{\sqrt{N_i N_j}} \int_{\mathcal{D}_i \bar{\mathcal{D}}_j} dp p dq q f(p) \bar{f}(q) |p\rangle |q\rangle, \quad (3.13)$$

where I note that the boundary distributions and weighting functions can be different for the two momenta. Similarly to FWPs, we can define SWPs by simply replacing the $|x_i\rangle$ wave packets with $|z_i^n\rangle$, such that

$$|Z_{ij}^\alpha\rangle \equiv |z_i^n\rangle \otimes |\bar{x}_j\rangle, \quad (3.14)$$

where $\alpha = \{n, \gamma, \Gamma\}$ as introduced in Sec. 2.1. The expression for the SWP has identical form to Eq. (3.13).

We can derive analytical expressions for all operators in Eq.(2.39) using the FWP and SWP bases, see App. B of Paper II, which written in matrix form for compactness is

$$\mathbf{U}(E) = \mathbf{C}^T \mathbf{PVC} + \mathbf{C}^T \mathbf{PVC} \mathbf{G}(E) \mathbf{U}(E), \quad (3.15)$$

providing a fair comparison.

where the matrix elements are defined by

$$\begin{aligned}
 \mathbf{V} &: \langle X_{i'j'}^{\alpha'} | \hat{v} | X_{ij}^{\alpha} \rangle, \\
 \mathbf{C} &: \langle X_{i'j'}^{\alpha'} | Z_{ij}^{\alpha} \rangle, \\
 \mathbf{P} &: \langle X_{i'j'}^{\alpha'} | \hat{P}_{123} | X_{ij}^{\alpha} \rangle, \\
 \mathbf{G} &: \langle Z_{i'j'}^{\alpha'} | \hat{G}(E) | Z_{ij}^{\alpha} \rangle, \\
 \mathbf{U} &: \langle Z_{i'j'}^{\alpha'} | \hat{U}(E) | Z_{ij}^{\alpha} \rangle.
 \end{aligned} \tag{3.16}$$

The U -matrix is now expressed in the SWP basis, meaning it contains both the elastic scattering channel as well as the break-up channels. Paper II shows the analytical derivations of these matrix elements where possible. Note I make no attempt to correlate the indices i , j , and α to matrix indices as it depends on the computational implementation of the method. How one chooses to index the matrices, however, has implications on computational cost since it affects the order in which one reads from the computer memory. I will detail this further in the next section where I cover my implementation.

3.4.1 Solving the Faddeev equations

Disseminating the computational problem of solving Eq. (3.15) can done by first considering it in a more compact form,

$$\mathbf{U} = \mathbf{A} + \mathbf{A}\mathbf{G}\mathbf{U}, \tag{3.17}$$

where $\mathbf{A} \equiv \mathbf{C}^T \mathbf{PVC}$. As discussed in Sec. 2.3.2, the large matrix dimensions from the NNN state space makes it unviable to use MI methods to solve this equation. Typically for NNN observables, the WPCD method converges in the order of $N_p = N_q = N_{\text{WP}} \sim \mathcal{O}(10^2)$ and $N_{\alpha} \sim 20\text{-}60$, in the $E_{\text{Lab}} < 50$ MeV region, where N_p and N_q are the number of $|x_i\rangle$ and $|\bar{x}_j\rangle$ states. This means each matrix would have, at least, $(N_p N_q N_{\alpha})^2 \sim 4 \times 10^{10}$ elements, which is the equivalent of 298 GiBs of computer memory with double floating-point precision per matrix. This memory impact is larger than what most modern computers have. This means solving the equation on the form $\mathbf{A}\mathbf{x} = \mathbf{b}$ using standard LAPACK [95] routines is not a practical approach.

Another way forward, touched upon in Chap. 2, is a Neumann series with Neumann terms \mathbf{N}_i . We can realise this by expanding the equation, i.e.

$$\mathbf{U} = \underbrace{\mathbf{A}}_{\mathbf{N}_0} + \underbrace{\mathbf{A}\mathbf{G}\mathbf{A}}_{\mathbf{N}_1} + \underbrace{\mathbf{A}\mathbf{G}\mathbf{A}\mathbf{G}\mathbf{A}}_{\mathbf{N}_2} + \dots = \underbrace{\sum_{i=0}^{m \rightarrow \infty} \mathbf{A} [\mathbf{G}\mathbf{A}]^i}_{\text{Case 1}} = \underbrace{\sum_{i=0}^{m \rightarrow \infty} [\mathbf{A}\mathbf{G}]^i \mathbf{A}}_{\text{Case 2}}. \tag{3.18}$$

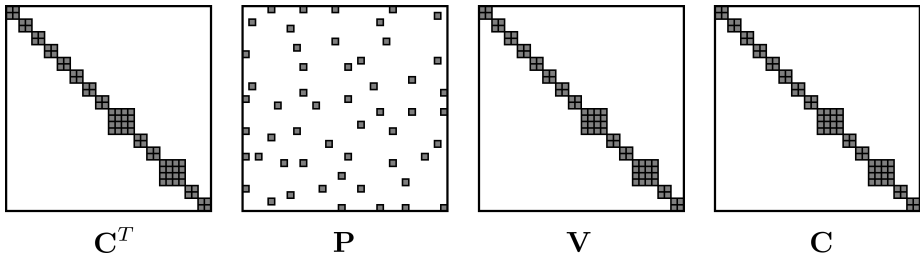


Figure 3.5: Illustration of structures of constituents in kernel \mathbf{A} . Matrices \mathbf{V} , \mathbf{C} , and \mathbf{C}^T are block-diagonal with identical structures, while \mathbf{P} is typically highly sparse ($\sim 99.9\%$) with seemingly randomly distributed non-zero elements.

This equation is simple to solve in the sense that we are only left with straightforward matrix multiplication to solve for \mathbf{U} . This is a significant advantage since matrix multiplication can be done piecewise without requiring much computer memory. Specifically, the matrix \mathbf{A} can be constructed in segments with which I can multiply \mathbf{N}_{i-1} and update to \mathbf{N}_i .

Perhaps unexpectedly, the computational bottleneck of this updating routine is not the matrix-matrix multiplication $[\mathbf{A}\mathbf{G}]^i \mathbf{A}$, or the cost of multiplying the diagonal matrix $\mathbf{G}(E)$ which is completely negligible, but rather the repeated kernel construction of \mathbf{A} . An immediate thought is to prestore \mathbf{A} to disk, but the slow reading of the disk makes it an inefficient approach. Additionally, in the larger channels with $N_\alpha = 60$, we would need almost 2700 GiBs of disk space for $N_p = N_q = 100$. Fortunately, there are several important aspects of \mathbf{C} , \mathbf{V} , and \mathbf{P} that can be utilised when constructing \mathbf{A} , which I will outline below in addition to the other technicalities of extracting on-shell U -matrix elements.

Constructing \mathbf{A} : Step 1 - handling memory

In Fig. 3.5 I illustrate the structure of non-zero matrix elements in the matrices that enter the generation of \mathbf{A} . The three matrices \mathbf{V} , \mathbf{C} , and \mathbf{C}^T all have the same block-diagonal structure that occurs since they represent two-body operators in a three-body basis⁵. Note that the matrices are only block-diagonal if the $|\alpha\rangle$ -basis is set up to have NN -coupled channels neighbouring one another, otherwise the off-diagonal blocks will be further from the diagonal. Where off-diagonal blocks appear has no effect on the computational efficiency of the implementation as it is fast to lookup non-zero blocks since $N_\alpha = \mathcal{O}(10)$. However, for simplicity I will refer to these as block-diagonal in the remaining text.

Many of the blocks in the block-diagonal matrices are repetitions of the same $(n'n)$ -channel occurring in different $(\alpha'\alpha)$ -channels. To avoid storing the

⁵This is seen from the delta functions in Eqs. (B5), (B6), and (B10) of App. B in Paper II.

same blocks repeatedly, I store the unique NN couplings and construct a map of where the blocks appear in the NNN representations \mathbf{V} and \mathbf{C} . Since only \mathbf{C}^T and $\tilde{\mathbf{V}} \equiv \mathbf{V}\mathbf{C}$ appear in the Faddeev equations, these are the only objects necessary to store, i.e.

$$\mathbf{A} \equiv \mathbf{C}^T \mathbf{P} \mathbf{V} \mathbf{C} = \mathbf{C}^T \mathbf{P} \tilde{\mathbf{V}}. \quad (3.19)$$

Note that $\tilde{\mathbf{V}}$ is the three-body equivalent to the one used in Eq. (3.9).

The permutation matrix \mathbf{P} is very sparse, typically about 99.9% sparse in a wave-packet basis, and with no apparent structure for its non-zero elements. The sparseness is almost entirely due to momentum violation. Its somewhat random structure entails I cannot find any simple segregation of elements into some smaller state space like with the block-diagonal matrices. Therefore, I use a standard sparse matrix storage format. Sparse-matrix storage formats are based on only storing non-zero matrix elements as well as their row and column indices. There are several sparse matrix storage formats available. The simplest of the formats is the coordinate format (COO) where each non-zero element v is stored together with its row-index r and column-index c , i.e. we make an entry (r, c, v) and store it. This format reduces the memory footprint of matrices with fewer non-zero elements than a third of the total size of the matrix. This memory impact can be reduced a bit further by using a compressed sparse row (CSR), for row-major storage, or compressed sparse column (CSC) format for column major storage, both of which require sorted indices in the leading matrix dimension. Tic-tac calculates and stores \mathbf{P} in a row-major COO format for simpler manipulation, and converts it to the CSC format when solving the Faddeev equations. For further details on sparse matrix storage and handling I refer the reader to, e.g., Chap. 11 of Ref. [76].

Constructing \mathbf{A} : Step 2 - efficient multiplication

Here I summarise the algorithm used to efficiently construct \mathbf{A} in column-wise segments to use in case 2 of Eq. (3.18). It is important to note that the computational bottleneck of constructing \mathbf{A} is not the actual floating-point operations required for matrix-matrix multiplication, but the memory accesses involved. As with the GPU, the CPU uses ~ 100 clock-cycles to retrieve something from the computer memory, but only a single clock cycle for multiplication. Thus, it is pivotal to minimise the lookup of elements to multiply, and to congregate the memory transfers to utilise the full width of the memory bus. This algorithm, currently used in Tic-tac, is invented with these principles in mind.

The outer matrices \mathbf{C}^T and $\tilde{\mathbf{V}}$ in Eq. (3.19) are stored as non-zero blocks, and can be retrieved using the $(\alpha'\alpha)$ - to $(n'n)$ -channel mapping discussed above. As mentioned, the permutation matrix \mathbf{P} is used in a CSC format, as column-major storage is favourable for case 2. If using the approach I outline here, it is advisable in case 1 of Eq. (3.18) to use the CSR format instead. It is

straightforward, although memory intensive, to transform between the CSC and CSR formats.

The \mathbf{A} -construction algorithm constructs a single column c of \mathbf{A} at a time. I therefore first perform the matrix product $\mathbf{P}\tilde{\mathbf{V}}$,

$$[\mathbf{P}\tilde{\mathbf{V}}]_{ic} = \sum_{j=1}^N \mathbf{P}_{ij} \tilde{\mathbf{V}}_{jc}, \quad (3.20)$$

where $N \equiv N_\alpha N_q N_p$. In the current implementation, an index i is given by the α -, q -, and p -indices as

$$i \equiv i_\alpha N_p N_q + i_q N_p + i_p, \quad (3.21)$$

where notation follows naturally. This indexing was an informed choice since the block-diagonal matrices are completely dense in i_p for a given block, meaning entire rows or columns of the matrix can be transferred from memory simultaneously. For a case-1 approach, one will likely profit by interchanging i_q and i_p . The product above is then written

$$\sum_{j=1}^N \mathbf{P}_{ij} \tilde{\mathbf{V}}_{jc} = \sum_{j_\alpha=1}^{N_\alpha} \sum_{j_q=1}^{N_q} \sum_{j_p=1}^{N_p} \mathbf{P}_{i_\alpha i_q i_p, j_\alpha j_q j_p} \tilde{\mathbf{V}}_{j_\alpha j_q j_p, c_\alpha c_q c_p}. \quad (3.22)$$

The two-body operator restricts the index $j_q = c_q$, and there only exist non-zero entries of $\tilde{\mathbf{V}}$ when j_α and c_α provide a coupling ($n'n$) that is allowed. Thus $\tilde{\mathbf{V}}$ strongly restricts the range of required multiplications in this sum. The column-major CSC format of \mathbf{P} is advantageous here since it immediately provides all non-zero elements in column j . See Fig. 3.6 for an illustration of the $\mathbf{P}\tilde{\mathbf{V}}$ generation. Note that the column-product of $\mathbf{P}\tilde{\mathbf{V}}$ is stored in a regular dense format.

The second matrix product, $\mathbf{C}^T \mathbf{P}\tilde{\mathbf{V}}$, is less complicated to perform as there are no sparse matrices involved when $\mathbf{P}\tilde{\mathbf{V}}$ is stored densely. I can loop through the blocks of \mathbf{C}^T and multiply with the corresponding range in $\mathbf{P}\tilde{\mathbf{V}}$ to give a column-segment of \mathbf{A} , using standard BLAS. This is illustrated in Fig. 3.7.

Resummation of the Neumann-series

The Neumann series in Eq. (3.18) is not guaranteed to be convergent for nuclear potentials. Divergences can occur if any of the Weinberg eigenvalues of the integral-kernel of a Fredholm type-II equation surpass the unit circle [96]. The size of the largest eigenvalue then provides a measure of how rapidly one can expect perturbative convergence, if it occurs. This was shown in detail for chiral NN potentials in [97], where NN bound states cause divergences in the series expansion of the LS equation. The appearance of bound states in the iterated channels of the Faddeev equations causes divergences as well.

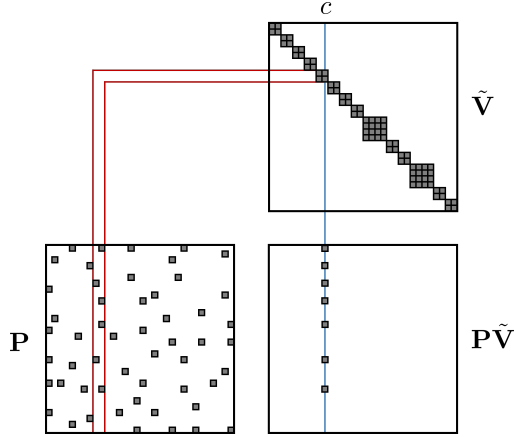


Figure 3.6: Illustration of the $\tilde{\mathbf{P}}\tilde{\mathbf{V}}$ matrix-vector multiplication for column index c , shown in blue. The matrix $\tilde{\mathbf{V}}$ is block diagonal and places strong restrictions on the number of elements of \mathbf{P} required for multiplication, shown in red. This makes a column-major sparse storage format of \mathbf{P} , such as the CSC format, more efficient for computer memory accesses.

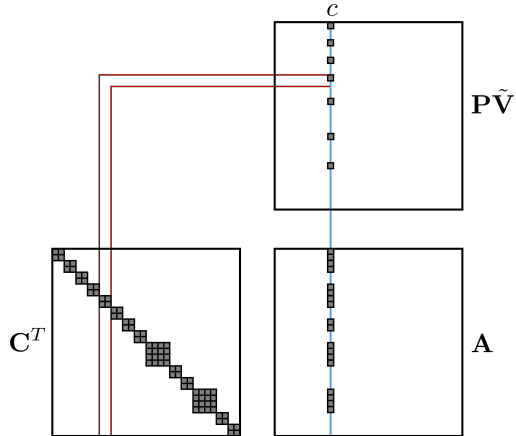


Figure 3.7: Illustration of the $\mathbf{C}^T\tilde{\mathbf{P}}\tilde{\mathbf{V}}$ matrix-vector multiplication for column index c , shown in blue. For each block in \mathbf{C}^T one multiplies with the corresponding range, shown in red, in the column of $\tilde{\mathbf{P}}\tilde{\mathbf{V}}$.

To cope with divergent series, one can use a Padé approximant (PA), see for example Ref. [98]. The series of some meromorphic function $f(z)$ is approximated as a fraction two N - and M -order polynomials, $P_N(z)$ and $Q_M(z)$, respectively, as

$$f(z) = a_0 + a_1z + a_2z^2 + \dots = \frac{P_N(z)}{Q_M(z)}, \quad (3.23)$$

where a_i play the role of the Neumann terms. This method can approximate singularities in $f(z)$, unlike a simple polynomial expansion as given on the left-hand side. The polynomial coefficients of $P_N(z)$ and $Q_M(z)$ can be evaluated as determinants constructed from the coefficients a_i , see for example App. C of Paper II. We can use PAs in Eq. (3.18) by letting $z = 1$ and $f(z)$ be the on-shell U -matrix element of interest, $\mathbf{U}_{(i_d j \alpha'_d, i_d j \alpha_d)}$, and a_i be the corresponding on-shell element of \mathbf{N}_i , i.e. $[\mathbf{N}_i]_{i_d j \alpha'_d, i_d j \alpha_d}$. Here, j is the bin containing the energy $E = E_k$ for some finite set $\{E_k\}_{k=1}^{n_E}$ we wish to calculate, and i_d , α'_d and α_d index the on-shell deuteron channels. Note there are only 2-3 deuteron channels given \mathcal{J}^{II} .

The parallelism of the WPCD method as I have implemented it can be made apparent here by noting that the on-shell solutions of the \mathbf{U} -matrix depend solely on the on-shell elements of \mathbf{N}_i . The parallelism comes with $\{E_k\}_{k=1}^{n_E}$; we can construct a layered \mathbf{N}_i matrix with n_E submatrices $\mathbf{N}_{i,k}$ that contain all rows containing on-shell elements for E_k . This entails that we can reuse the expensive construction of \mathbf{A} by multiplying it with a different resolvent per set of rows, i.e.

$$[\mathbf{N}_{i,k}]_{i_d j \alpha'_d, i_d j \alpha_d} = [\mathbf{N}_{i-1,k} \mathbf{G}(E_k) \mathbf{A}]_{i_d j \alpha'_d, i_d j \alpha_d}. \quad (3.24)$$

Note that j depends on E_k . As stated, it is usually best to use bin mid-points for E_k , in which case $j = k$ in this submatrix-segmentation of \mathbf{N}_i . Unlike WPCD in NN scattering, I have not implemented energy-averaging in Tic-tac, following [51].

I have covered all the steps involved in solving the Faddeev equations efficiently in this section. Tic-tac follows a simple set of steps shown in Fig.3.8, which have all been presented above. Tic-tac contains much additional functionality involving reading and writing from/to disk, setup of potential matrices, internal validation checks, and other user-controllable services. However, none of these functions are particularly time-consuming compared to iterating the Faddeev equations. Note that Tic-tac solves each NNN -channel \mathcal{J}^{II} separately, allowing for parallel execution of different NNN channels.

Note that Tic-tac provides U -matrix elements in a SWP basis. These can be converted to a plane-wave basis using Eq. (D5) in Paper II. For calculating observables, I refer the reader to the discussion of Chap. 2 and Paper II for extracting M -matrices, as well as Refs. [33, 60, 62] for projecting M using Eq. (2.1).

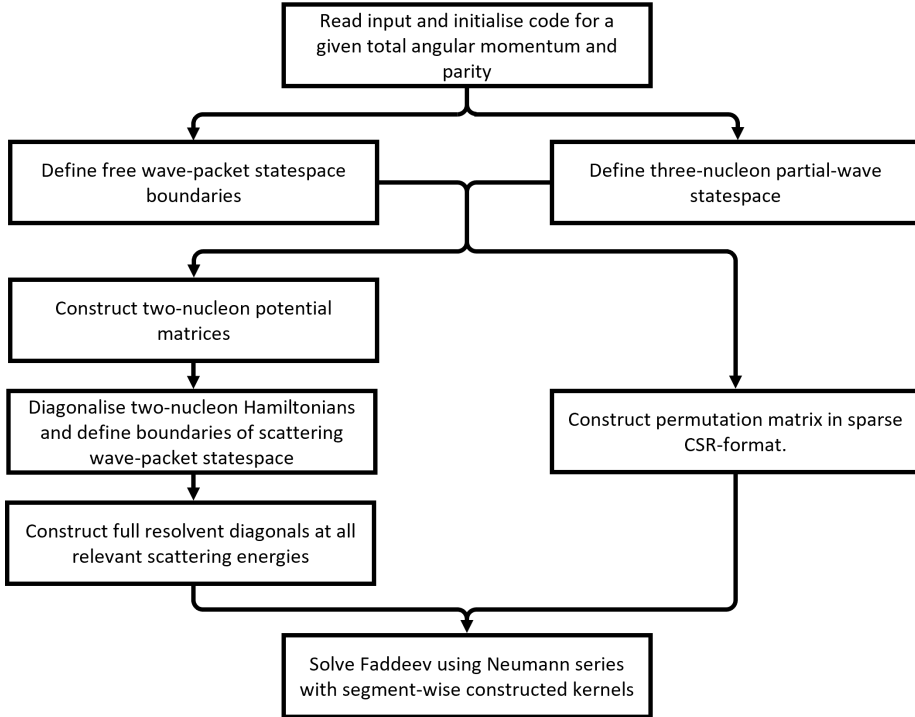


Figure 3.8: Basic flowchart of Tic-tac program execution.

3.4.2 Convergence of the WPCD method for elastic Nd scattering

The WPCD method for solving the Faddeev equations has several method parameters that systematically affect the convergence of scattering observables. A summary of the parameters is shown in Tab. 3.2, making up a total of 11 parameters that require inspection and tuning. Here I will summarise the convergence of Nd scattering observables with respect to the parameters, in the order of appearance in the table, except for the wave-packet basis size which is left for last. The Chebyshev distribution parameters were already discussed above and need not be touched upon further here. This applies to the convergence of \mathbf{V} with respect to N_k as well. However, I note that the Faddeev calculations presented here are based on momentum FWPs in a Chebyshev distribution with $t = 1$ and $s = 200$ MeV.

The permutation matrix is projected to the wave-packet basis with cylindrical quadrature variables as seen in Eq. (B13) of Paper II. I reserve N_x and N_ϕ to denote the number of quadrature points used for each variable, de-

Table 3.2: Summary of WPCD method parameters for solving the Faddeev equations. See text for symbol definitions.

Method step	Number of parameters	Parameters	Comments
FWP basis	4	$N_p, N_q, (t, s)$	Choose FWP type
\mathbf{V}	1	N_k	Negligible cost
\mathbf{P}_{123}	2	N_x, N_ϕ	One-time cost
\mathbf{C}	0	None	Predetermined
$\mathbf{G}(E)$	1	E	Analytically known
$\mathbf{U}(E)$	3	m, N, M	$m = N + M$

noted x and ϕ in the Paper, respectively. Figure 3.9 presents the convergence of randomly-drawn elements of the \mathbf{P}_{123} -matrix with respect to N_x and N_ϕ . The convergence is trivial with N_ϕ , as $N_\phi \sim 20$ appears already convergent. With N_x the convergence trend is more oscillatory but note that most of the larger matrix elements converge already at about $N_x \sim 30$. The size of the FWP basis has little impact on the convergence. In my calculations I have typically used $N_x = N_\phi = 48$ and have seen no noticeable effect in scattering observables in going up to $N_x = 96$.

Following the definition of the FWP basis and construction of \mathbf{V} , there are no parameters that enter the construction of \mathbf{C} , or $\mathbf{G}(E)$ beyond the energy E . The energy, as discussed, could either be integrated out to provide energy-averaged U -matrix elements or set on bin mid-points. As stated, I used the latter in my calculations and set E on the FWP bin midpoints.

The Neumann-series truncation parameter m from Eq. (3.18) must be set so that $m = N + M$. Having seen no computational advantage to asymmetric selections of N and M , I use “symmetric” PAs with $N = M = \frac{m}{2}$. Figure 3.10 shows convergence of the PAs with respect to N and M for two U -matrix elements. The figure shows the typical trend of the PA; it converges usually at some value of $N = M$ in the range $[5, 12]$, thus requiring $m \in [10, 24]$ Neumann terms. Note the lower-right panel. Here we see that the PA can start to diverge due to numerical instability in the polynomial fraction of Eq. (3.23). The instability occurs since the polynomials have very large values due to diverging Neumann terms.

Since the computational cost of setting up Neumann terms dominates the computational time, Tic-tac uses four tests for convergence and the code stops setting up Neumann terms should any one of the conditions be satisfied:

1. If $i = m$ in Eq. (3.18), i.e., the iterations reach an upper limit. I have set this upper limit to $m = 29$.
2. If no better PA is found within 4 increments of N and M .

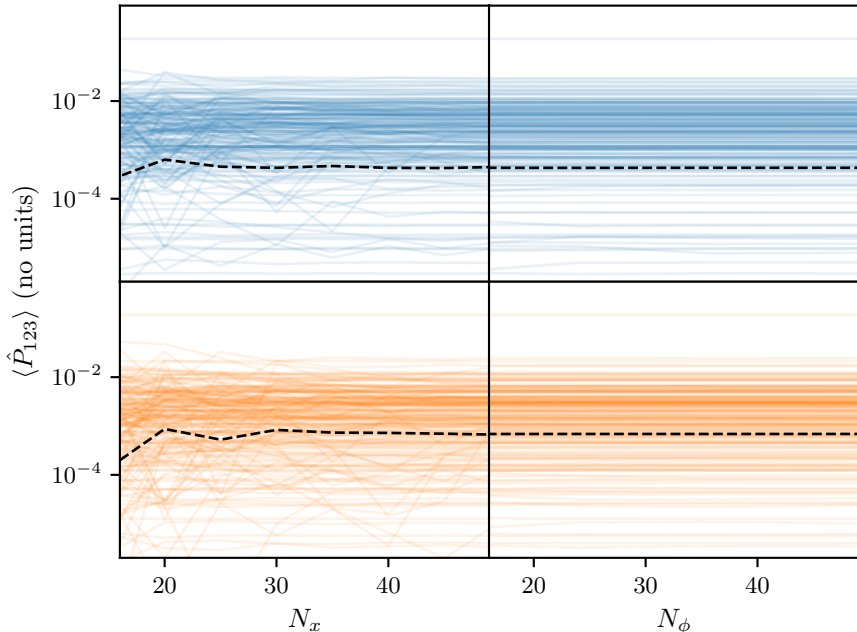


Figure 3.9: Convergence of 200 randomly-drawn \mathbf{P}_{123} -matrix elements in a FWP basis as a function of the number of quadrature points N_x and N_ϕ for x and ϕ , respectively, for $N_{WP} = 50$ (blue, top) and $N_{WP} = 100$ (orange, bottom). The dashed lines show the average of plotted lines.

3. If the difference between two subsequent PAs is less than the 4th significant digit of the prior PA.
4. If the difference between two subsequent PAs is less than single floating-point precision.

Lastly, there is the number of wave packets to use, which was covered extensively in Paper II. In the Paper, we worked with a partial-wave truncation defined by $J \leq 3$ and $\mathcal{J} \leq \frac{17}{2}$. These values provide well-converged results [33] in the $E_{\text{Lab}} \leq 50$ -100 MeV region, depending on the observable. Note I have seen no advantage to use asymmetric selections of N_p and N_q and will simply let $N_{WP} \equiv N_p = N_q$.

In Paper II it was found that in the aforementioned energy region we can typically use $N_{WP} = 50$ -100 to land at around 99% of convergence. To benchmark Tic-tac, and to expand on the benchmarking of Paper II, I show in Fig. 3.11 a reproduction of observables using benchmarking data published by the Bochum-

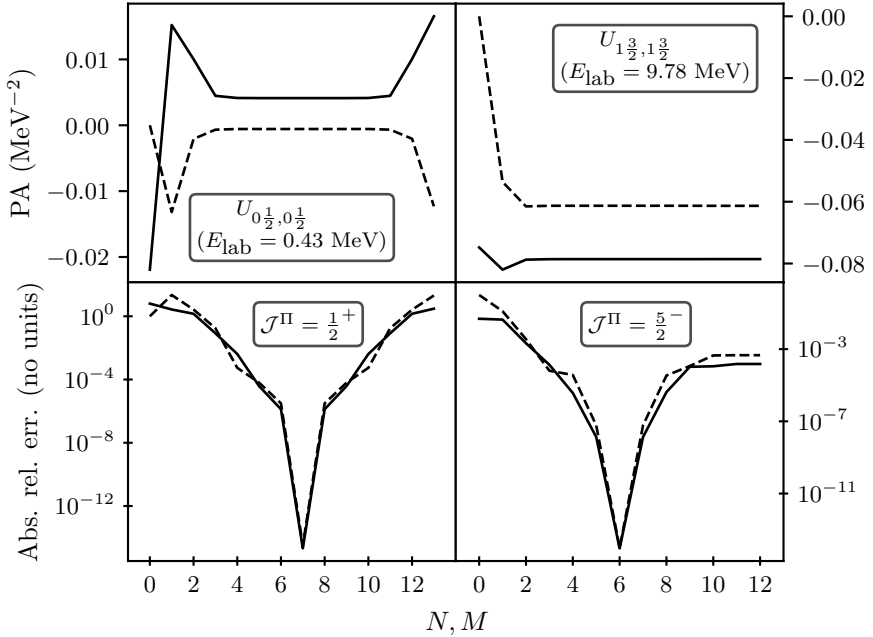


Figure 3.10: Convergence of PAs with number of Neumann-series terms $m = 2M = 2N$ for U -matrix elements $U_{l'j',lj}$ for two NNN partial-wave states as labelled, using the $N2LO_{\text{opt}}$ potential. The energies are randomly drawn FWP midpoint energies. The solid (dashed) lines are real (imaginary) components. The relative difference is taken with respect to the converged U -matrix element returned by Tic-tac, which can be seen to lie at $N = M = 6$ or 7 in the two cases.

Krakov collaboration [33] at $E_{\text{Lab}} = 13$ MeV, made with the Nijmegen-I potential [99] and using charge independence breaking (CIB) for the 1S_0 -interaction. Except for the low-angle discrepancy of the A_y observable, the Tic-tac code manages to reproduce the benchmark well. For further convergence documentation, and comparison with experimental data, see Paper II.

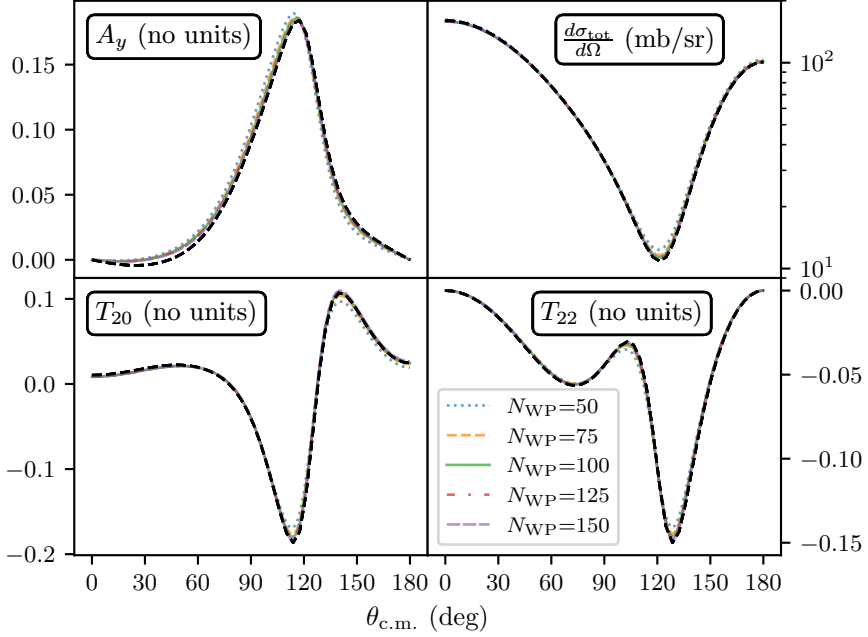


Figure 3.11: Convergence with N_{WP} of the WPCD-generated differential cross section and common spin-observables for elastic nd scattering at $E_{\text{Lab}} = 13$ MeV with the Nijmegen-I potential. The benchmark (dashed, black) is generated from Tab. 13 of Ref. [33]. The calculations were done with $\mathcal{J} \leq \frac{7}{2}$ and using CIB for 1S_0 -interactions.

Chapter 4

Posterior predictive distributions for neutron-deuteron scattering cross sections

In this chapter, I will discuss the study of Paper III. In the paper, we used PPDs to quantify the LEC variability in nd scattering predictions at scattering energies up to 67 MeV, using chiral 2NFs up to $N^3\text{LO}$. As mentioned, the motivation for our study was to root out the LEC variability of 2NFs as the cause of long-standing theoretical discrepancy to experimental data in the NNN continuum. This kind of study had not yet been performed in a fully Bayesian framework.

The LECs were conditioned on NN scattering data in Refs. [31, 32] using Bayesian methods. To calculate nd scattering amplitudes we used the aforementioned code in Chap. 3, Tic-tac, to solve the AGS equations using WPCD. To enable the study, we had to balance computational cost with accuracy, resulting in the use of extrapolation of entire PPDs.

Section 4.1 starts with a discussion on theoretical predictions and how one can account for theoretical uncertainty using Bayesian statistics. In Sec. 4.2, I will summarise the statistical model used in Paper III for quantifying the predictive uncertainty, and describe how we balanced predictive accuracy and computational speed to gain statistical insight. Lastly, in Sec. 4.3, I present the results of our analysis.

4.1 Theoretical predictions and uncertainty

A prediction, $y_{\text{prediction}}$, of an observable, y , is aimed at reproducing observational data, y_{data} , as well as possible. In general terms, a theoretical prediction

can be related to the data via two unknown error-terms, $\delta y_{\text{prediction}}$ and δy_{data} ,

$$y_{\text{data}} = y_{\text{prediction}} + \delta y_{\text{prediction}} + \delta y_{\text{data}} . \quad (4.1)$$

Here I set δy_{data} equal to published experimental error estimates. The prediction error, $\delta y_{\text{prediction}}$, is important to quantify to know the prediction accuracy¹. Assuming independent sources of error, the prediction error can be broken down into separate terms,

$$\delta y_{\text{prediction}} = \delta y_{\text{model}} + \delta y_{\text{method}} + \delta y_{\text{other}} , \quad (4.2)$$

where δy_{model} is the error of the model itself, for example mistakenly using a linear model for analysing oscillating data, and δy_{method} is the error of the method used for observable calculations, for example using too small basis sizes in solving the Schrödinger equation. The last term, δy_{other} , is included to encompass other sources of uncertainty, such as numerical error, which I safely neglect here.

If the model error term is neglected, one presumes a theoretical model that is error-free. Then, the inference process will try to condition the model to reproduce the data exactly, within experimental and method errors. The consequence is an overfitted model that is likely to fail when predicting new observables not included in the inference process. This problem is summarised in, e.g., Ref. [100]. An advantage of χ EFT is that it provides a handle on its power-series truncation error through the systematic convergence trend of a power series. We are now left with a challenge; we have *a priori* unknown LECs whose determination requires inference from data, entailing LEC-uncertainty on top of the uncertainty from the χ EFT truncation error. These uncertainties must be quantified to predict new observables with confidence. This is where we can use methods from *Bayesian statistics*.

Bayesian statistics is built on Bayes' theorem, which for LECs being conditioned on a dataset D can be written [101]

$$\underbrace{\text{pr}(\vec{\alpha}|D, I)}_{\text{posterior}} = \frac{\overbrace{\text{pr}(D|\vec{\alpha}, I)}^{\text{likelihood}} \cdot \overbrace{\text{pr}(\vec{\alpha}|I)}^{\text{prior}}}{\underbrace{\text{pr}(D|I)}_{\text{evidence}}} . \quad (4.3)$$

Here, the posterior probability density function (PDF), $\text{pr}(\vec{\alpha}|D, I)$, is a distribution representing the DoB in values of the LECs, $\vec{\alpha}$, given data, D . The prior information, I , symbolises what we know or suspect prior to inference

¹We usually do not get different results for repeated theoretical predictions, except for stochastic methods such as Monte Carlo simulations, making “theoretical precision” an ambiguous term. Since I do not develop stochastic methods in this work, I will only talk of prediction accuracy.

from D . For example, I can reflect that $\vec{\alpha}$ should have natural values, as well as which functions to use for the likelihood and prior distributions, and the functions' hyperparameters, such as the variance of a normal distribution. The evidence serves as a normalisation constant here and is irrelevant for parameter estimation such as the inference of LECs.

With a LEC posterior in place, one can construct a PDF for observable predictions through marginalisation, where the LEC-dependency is integrated out,

$$\text{pr}(y|D, I) = \int \text{pr}(y|\vec{\alpha}, D, I)\text{pr}(\vec{\alpha}|D, I) d\vec{\alpha}. \quad (4.4)$$

This PDF quantifies the uncertainty in the prediction of y for a given χ EFT model conditioned on D . Then, for example, we have $\text{pr}(y|D, I) = y_{\text{prediction}} + \delta y_{\text{model}} + \delta y_{\text{method}}$. When y is a new observable not contained in D , this marginalisation provides a PPD. At this point it seems natural that, as opposed to a single-point prediction, a distribution arises due to the uncertainties inherent in our predictions as well as in the experimental data.

Note that one can also marginalise with respect to theoretical models, such that one arrives at an observable PPD which contains several theoretical predictions. This is useful in investigating new physics where the theoretical foundations are uncertain, see for example Refs. [102, 103], but such model-marginalisation was not used in Paper III.

4.2 Statistical model for evaluating PPDs

It is perhaps unsurprising that evaluating a multi-dimensional LEC PDF usually requires thousands of model predictions [31, 32]. A PPD typically requires fewer evaluations, roughly on the order of one hundred for a one-dimensional distribution. The number of required distribution samples scales with the dimensionality of the distribution. The cost and speed of computational theoretical predictions of the set of observables y contained in D determine whether statistical inference is achievable. To evaluate the integral in Eq. (4.4), there are at least three practical problems we must control as best as possible:

1. *Sufficiently many uncorrelated distribution samples.* The distributions, $\text{pr}(y|D, I)$ and $\text{pr}(\vec{\alpha}|D, I)$, are not known analytically. Instead, one must numerically sample them using algorithms such as Markov chain Monte Carlo. One sample is a single point in a distribution, i.e., a single observable prediction, y , or a set of LEC values, $\vec{\alpha}$. It is important to have sufficiently many uncorrelated samples resolution to accurately represent the distributions. Correlation of samples can be determined by quantifying the correlation length in sequences of samples, like a Markov chain.

2. *Sufficient computational accuracy and speed.* While sampling the PPD, we must also stay within a limited computational budget. To ensure sufficiently low cost, a balance between the method accuracy and speed must be struck. This is where Paper II served as a guideline for the study of Paper III.
3. *Accurate uncertainty modelling.* The prediction uncertainty must not spoil our study of the LEC variability. This requires an accurate model for our uncertainty to ensure that the model and method errors do not spoil the content of a calculated PPD. I note that we did not model the method uncertainty, as I will discuss further in the next section.

These problems are correlated, as we must strike the right balance between number of PPD samplings, method basis size and accuracy, and uncertainty budget. In this section I will summarise how we addressed these issues in the context of Paper III, in the order of appearance in the list.

4.2.1 Sample correlations and PPD integral evaluation

In Refs. [31, 32], a Bayesian inference study was done using Hamiltonian Monte Carlo (HMC) [104] to extract the PDFs for the LECs in chiral 2NFs up to $N^3\text{LO}$. The PDFs were conditioned on NN scattering cross sections and scattering length data via Eq. (4.3). The advantage of HMC is that it can provide sample correlation lengths at around $\mathcal{O}(1)$, i.e. two subsequent samples can be uncorrelated. For our case, this is not strictly necessary as we only require $\mathcal{O}(10^2)$ for the PPD sampling, as mentioned earlier. While our analysis was too limited to determine the PPD correlation length, see for example the discussion of Ref. [31], we saw no obvious correlation through Fig. 1 of Paper III.

The number of samples had to be decided beforehand due a limiting, yet large, computational budget of $\sim 500,000$ core-hours. Consequently, we had to balance method accuracy and the number of samples required for obtaining PPDs with sufficient quality. While PDFs are usually high-dimensional functions, requiring a vast number of samples to be accurately portrayed, marginal PPDs are one-dimensional distributions for a given observable and can typically be accurately portrayed by $\mathcal{O}(10^2)$ samples. In Paper III, we used 100 samples from the LEC PDFs at each chiral order.

4.2.2 Trading method accuracy for computational speed

In its current state, the code, Tic-tac, cannot calculate 100 samples per chiral order for basis sizes $N_{\text{WP}} \gtrsim 100$, as typically required for sufficient accuracy, with the computational budget stated above². This basis size was established

²As this is hardware-dependent, I note we used computing nodes with 2x Intel Xeon Gold 6130 CPUs, each with 16 cores.

in Chap. 3 and Paper II to typically give converged solutions up to $E_{\text{Lab}} \approx 70$ MeV, where we start to see a difference between $N_{\text{WP}} = 100$ and 125. Depending on the observable, we can even calculate accurately up to $E_{\text{Lab}} = 100$ MeV, where using $J \leq 3$ will start being insufficient for convergence [33]. Therefore, we performed calculations at all $E_{\text{Lab}} \leq 100$ MeV. Calculating predictions in such a wide range of energies was not a problem due to the cheap cost overhead for acquiring multiple on-shell scattering amplitudes by solving the AGS equations with WPCD. To extract amplitudes at arbitrary energies we used linear interpolation of calculated amplitudes at the NN Hamiltonian eigenvalues, as follows from using the SWP basis; see Chap. 3.

As discussed, the WPCD method has a quartic computational scaling with N_{WP} , i.e., $\mathcal{O}(N_{\text{WP}}^4)$. This meant we could significantly reduce computational costs by going to $N_{\text{WP}} = 75$ yet achieve reasonable solution accuracy. Thus, we sampled the PPDs with $N_{\text{WP}} = 75$. However, since this basis size does not provide fully converged solutions, we resampled the PPDs at $N_{\text{WP}} = 30$ and 50, at a negligible additional cost. This allowed us to study the convergence trend of the entire PPD. Furthermore, we calculated the first 10 samples at $N_{\text{WP}} = 100$ to investigate the almost-converged distribution, as far as the budget allowed. Upon inspection of the PPDs at different N_{WP} we saw that the width and shape remain largely the same. This can be seen in Fig. 3 of Paper III where nd differential cross section at $E_{\text{Lab}} = 12$ MeV for $N^2\text{LO}$. Thus, a single-point calculation at some higher value for N_{WP} would allow us to extrapolate entire PPDs from $N_{\text{WP}} = 75$.

To extrapolate PPDs, we calculated the maximum *a posteriori* (MAP) points of the LEC PDFs for $N_{\text{WP}} = 30, 50, 75, 100$ and 150, also shown in Fig. 3 of Paper III. The MAP predictions show slow and steady convergence as expected for the WPCD method. Thus, we extrapolate by shifting all PPDs at $N_{\text{WP}} = 75$ by the distance between the MAP predictions at $N_{\text{WP}} = 75$ and $N_{\text{WP}} = 150$. Note, however, that even $N_{\text{WP}} = 150$ is not fully converged, as shown with Paper II. Full convergence is not so important as we are mainly interested to see if LEC variability can be the cause of the long-standing theoretical and experimental discrepancies in the NNN continuum. An offset accuracy of $\mathcal{O}(1)$ percent of the observable value, as one can expect at $N_{\text{WP}} = 150$, is negligible for discrepancies at $\mathcal{O}(10)$ percent, as seen in, for example, the A_y puzzle. I will return to this observable later in the text.

As a sidenote, the surprisingly consistent PPD widths for different basis sizes may indicate a possibility to speedup the Tic-tac code. The consistency, albeit in a small part of the model parameter space, suggests that the slow convergence of Nd scattering observables with N_{WP} is not primarily due to a coarse-grained representation of the nuclear potential. We investigate the topic of coarse graining in greater depth in the discussion surrounding Fig. 4 of Paper I. Also supporting this claim, we saw convergence of the NN total cross-section to within a few percent for almost all E_{Lab} when using only $N_{\text{WP}} = 64$

in Chap. 3, see Fig. 3.3. Thus, it seems plausible that the permutation operator is suboptimally represented in a wave-packet basis due to its complicated momentum-conservation structure [85]. To circumvent a suboptimal representation, one proposal is to calculate the inner-product $\hat{P}\hat{v}$ in Eq. (2.39) using the standard spline basis [17, 73]. Afterwards, $\hat{P}\hat{v}$ can be projected onto an SWP basis and the kernel \mathbf{A} in Eq. (3.17) can be used as normal. With this approach, one can possibly allow for a smaller basis size, N_{WP} , in solving the AGS equations.

4.2.3 Theoretical uncertainty modelling

Earlier, I mentioned that χEFT provides a direct handle on its theoretical uncertainty through the systematic truncation error. To quantify this, we can consider a general χEFT description of a prediction, $y_{\text{prediction}} = y_{\text{theory}}^{(\nu)}$, with truncation at chiral order ν [105],

$$y_{\text{theory}}^{(\nu)} = y_{\text{ref}} \sum_{k=0}^{\nu} c_k Q^k, \quad (4.5)$$

where the reference value y_{ref} is the natural scale of the observable set by, e.g., the experimental value or the LO prediction, while c_k are dimensionless expansion coefficients, expected to have natural values for all k . Here, Q is dimensionless, whose value is an ongoing topic of discussion, see for example Ref. [106], but we define it as

$$Q \equiv \max\left(\frac{q}{\Lambda_b}, \frac{m_\pi}{\Lambda_b}\right), \quad (4.6)$$

and where we use $\Lambda_b = 600$ MeV for the χEFT breakdown scale following Ref. [32], and q is the external momentum, which in this case is set to the nd relative momentum. The reference, y_{ref} , was set as the LO MAP prediction in the cases of the total and differential cross sections, while it was set to unity for the spin-observables. The coefficients are extracted from predictions at subsequent orders,

$$c^{(\nu)} = \frac{y^{(\nu)} - y^{(\nu-1)}}{y_{\text{ref}} Q^\nu}. \quad (4.7)$$

The truncation uncertainty is contained in the omitted terms of the series,

$$\delta y_{\text{theory}} = \delta y_{\text{theory}}^{(\nu)} = y_{\text{ref}} \sum_{k=\nu+1}^{\infty} c_k Q^k, \quad (4.8)$$

where we must model the unknown coefficients c_k for $k > \nu$. Following Ref. [31], we assume the coefficients to be uncorrelated and normally distributed with

variance \bar{c}^2 and zero mean,

$$\text{pr}(c_k|D_T, I) = \mathcal{N}(0, \bar{c}^2). \quad (4.9)$$

Here, $D_T = \{c_{k,i}\}$ is the set of all known expansions coefficients, $c_{kk,i,i}$, we use to infer \bar{c} , where k and i denote the chiral order and training observable, respectively. As the distribution variance is unknown one should attach a prior distribution for \bar{c}^2 , incorporating our expectation for naturalness. However, we opted for simply determining \bar{c}^2 from the root-mean square (RMS) of D_T ,

$$\bar{c}^2 \equiv \frac{1}{\nu \times N_T} \sum_{i=1}^{N_T} \sum_{k=1}^{\nu} c_{k,i}^2, \quad (4.10)$$

where N_T is however many training observables one uses. Furthermore, the LEC dependence of $c_{k,i}$ should be marginalised out. However, since our PPDs are quite narrow, using the PPD averages to infer \bar{c}^2 provided a suitably accurate approximation. If our expectations are met, we should get $\bar{c} \sim 1$ due to naturalness. If all the coefficients are modelled as independent and normally distributed, Eq. (4.8) becomes a standard geometric series we can solve analytically [29],

$$\text{pr}\left(\delta y_{\text{theory}}^{(\nu)} | \bar{c}^2, I\right) = \mathcal{N}(0, \sigma_{\text{theory}}^2) \quad \text{where} \quad \sigma_{\text{theory}}^2 \equiv \bar{c}^2 y_{\text{ref}}^2 \frac{Q^{2(\nu+1)}}{1 - Q^2}. \quad (4.11)$$

Note that all $\nu = 1$ contributions violate time- and parity-reversal invariance in χEFT , such that ν should be incremented by +1 in σ_{theory}^2 for the LO truncation uncertainty.

Our study did not take into account 3NFs, meaning that the order-by-order construction of $c_{k,i}$ will be wrongful at orders beyond NLO as we do not include all contributions, providing misleading uncertainty estimates. Missing 3NFs when doing χEFT uncertainty modelling was also addressed in Ref. [36]. To attempt accounting for neglected 3NFs, we can increase the scale of the truncation error at a given order, i.e. divide σ_{theory}^2 by factors of Q for all $\nu > 2$.

Alternatively, as we did in Paper III, we focus on observables in energy ranges where they are mostly independent on 3NFs. For example, the differential cross section was known already in 1998 to be insensitive to 3NFs up to 60 MeV [56]. A recent, comprehensive analysis of chiral 3NF contact terms investigated 3NF effects also for the spin-observables $A_y(n)$, iT_{11} , T_{20} , T_{21} , T_{22} , and total cross section [57], where mostly $A_y(n)$ and iT_{11} were susceptible to 3NFs. Note that this is not a new finding [55]. I will present PPDs for some of these observables in the next section, with the rest shown in App. B.

4.3 PPD analysis and interpretation

The study presented in Paper III focuses on nd scattering, showing the differential cross section and the neutron spin analysing power, denoted here in shorthand as A_y , in three scattering energy regions: $E_{\text{Lab}} = 10\text{-}12$, $35\text{-}36$, and $65\text{-}67$ MeV. While these make up a small slice of the observable NNN continuum, they reflect of our overall findings. Here, I will broaden on the presentation by including additional observables and scattering energies, as well as summarise our findings and discuss our conclusions. I will start with by focusing on the total cross section with a comparison of the PPDs to the χEFT uncertainty, using the model introduced in Eq. (4.11). Then I will expand on the analysis of Paper III, focusing on differential cross sections and spin observables with the χEFT uncertainty analysed separately.

As mentioned above, our predictions were made using $J \leq 3$ and $\mathcal{J} \leq \frac{17}{2}$, which is overall accurate for $E_{\text{Lab}} \leq 70$ MeV [33], with CIB in the 1S_0 -channel and using the PPD-shift extrapolation introduced above. We calculated \bar{c} using Eq. (4.10), with coefficients calculated using Eq. (4.7). In the latter equation, we set $y^{(\nu)}$ equal the mean of the PPDs, and inferred at $\theta = 30, 90$ and 150 degrees for any given energy. We set $y_{\text{ref}} = 1$ for the spin observables and y_{ref} set by the LO prediction for the differential cross section. Here, I will also show the nd total cross section, for which I use the LO predictions for y_{ref} and infer \bar{c} at $E_{\text{Lab}} = 5, 35$, and 70 MeV.

4.3.1 The total cross section

While the total cross section is usually too crude to investigate the finer details of the spin-structures of nuclear Hamiltonians, this observable provides a clear overview with respect to the energy dependency of the scattering process. Figure 4.1 shows the PPD for the total cross section for $E_{\text{Lab}} \in [1, 80]$ MeV. The PPDs at all orders show that the PPD widths are consistently comparable to the the experimental uncertainties, and very narrow relative to the size of the observable and the χEFT truncation uncertainty. Note that by following Ref. [36] and modifying the truncation uncertainty to account for missing 3NFs, the N^2LO and N^3LO truncation uncertainty bands become comparable to the one for NLO. While the focus here is not on the accurate predictions of experimental data, the chiral order-by-order convergence in the figure nonetheless warrants commentary.

On close inspection, it is satisfactory to note that we see convergence onto experimental measurements with each new chiral order. However, while there are clear inaccuracies at LO, also appear slight systematic inaccuracies at NLO and N^2LO across the entire shown energy range, with them ultimately starting to fail at around $E_{\text{Lab}} \simeq 50$ MeV. It is first at N^3LO we see a predictive accuracy up to the region where we expect visible effects from 3NFs, at around

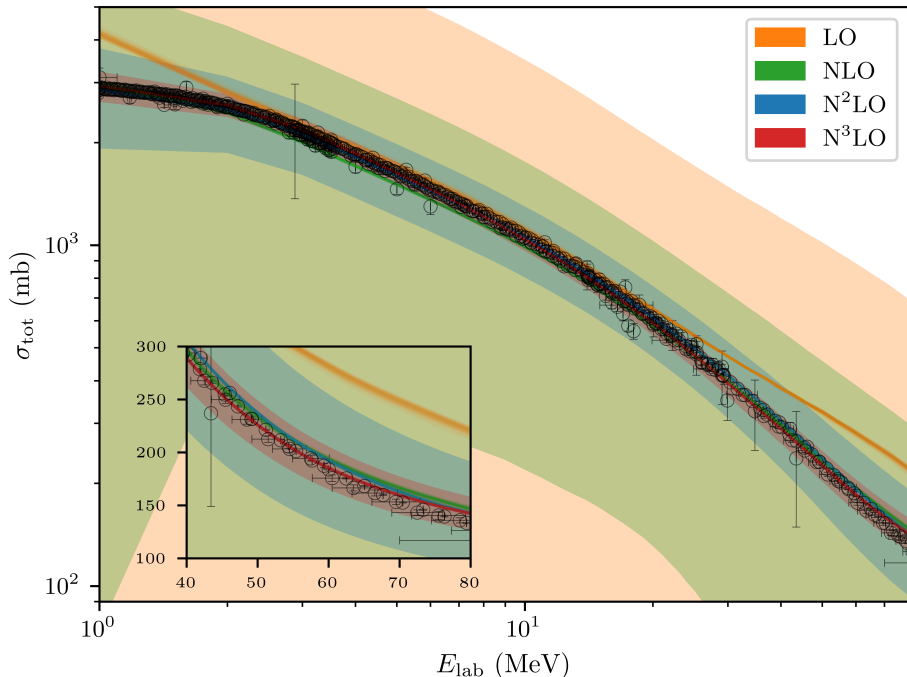


Figure 4.1: PPDs for the nd total cross section up to $N^3\text{LO}$ for NN -only forces inferred on NN scattering data [32]. See text for details on calculation. The nd and proton-deuteron (pd) experimental data (markers) were retrieved using the EXFOR database [25]. The bands show the χEFT truncation uncertainty at 95% DoB bands as normal distributions centred on the PPD mean with $\bar{c} = 6.6$, calculated using Eq. (4.11). The bands are shown with colours corresponding to the chiral order.

$E_{\text{Lab}} = 67$ MeV [56], suggesting $N^3\text{LO}$ to work well below this energy once 3NFs are included. This may also be the case for $N^2\text{LO}$, see, e.g., Ref. [107] for a discussion of 3NFs included at $N^2\text{LO}$ at $E_{\text{Lab}} = 70$ MeV.

4.3.2 Differential cross section and A_y -observable

In Paper III, we investigated the differential cross section and the neutron vector analysing power, A_y , shown in Fig. 4.2. Estimates of the χEFT uncertainty were discussed separately in the Paper, which I will return to later. To quantify the width of PPDs, in Paper III we calculated 90% highest posterior density intervals (HDPIs) by first averaging the PPD at all angles, and then by averaging these PPD-averages with respect to the angle. These averaged intervals are

shown in the figure and demonstrate that the widths of the PPDs clearly grow narrower when going to higher orders. For example, the differential cross section goes from a HDPI of 5.71% to 0.52% at $E_{\text{Lab}} = 12$ MeV. These HDPI values do not change significantly up $E_{\text{Lab}} = 67$ MeV. Mostly, I find the PPDs provide HDPIs that stay below 15% for all observables and energies, and display similar narrowing with higher orders as in the figure.

For the differential cross section at LO, we see a noticeably wider distribution compared to subleading orders. We suspect this larger width ensues directly from the corresponding LEC PDF, which is significantly wider compared to higher orders, see Ref. [32]. However, it is also apparent that the LO predictions must lack relevant details to accurately describe the observables, showing little resemblance to experimental data and higher-order predictions. The higher-order predictions are somewhat in agreement with each other, except for the A_y observable at low energies.

Being too many to include here, I show all PPDs for the spin-observables studied in Ref. [57] at higher scattering energies in App. B, in Figs. B.1 to B.4. The figures show that the PPDs stay consistently thin at all energies, except for at the limit of negligible 3NFs effects ($E_{\text{Lab}} \simeq 67$ MeV) where some PPDs begin to broaden slightly. While I do not quantify HDPIs or compare with experimental data, the PPDs show that all predictions at subleading orders largely agree up to $E_{\text{Lab}} = 60$ MeV. Disagreement between orders, clearly visible at $E_{\text{Lab}} = 80$ MeV in Fig. B.4, reflects the discussion above surrounding the total cross section.

Exception to the overall agreement of PPDs at different orders is the A_y observable. Both in Fig. 4.2 and App. B, A_y and the tensor analysing power iT_{11} , known to behave similarly [33, 110], stand out by showing clear order-by-order differences in the PPDs for all $E_{\text{Lab}} \leq 30$. There is a long-standing discrepancy between theory and experiment for the A_y observable in this energy region, named the “ A_y -puzzle” [54, 55]. While it is interesting to see the close proximity of the experimental and N³LO peaks of the A_y observable, note that the N³LO prediction has significantly lower accuracy at lower angles. Furthermore, as noted in our Paper, the ³H and ³He ground-state energies and radii are further off-mark than for, e.g., N²LO. The A_y observable is also very dependent on the description of the triplet P-wave interactions, see e.g. Ref. [33], which for the N³LO PDFs have unnatural LEC values compared to the majority of the remaining LECs. It is clear that the PPDs of this study do not resolve the puzzle.

To discuss χ EFT uncertainty for the differential cross section and spin-observables, it was easier to compare the PPD and the χ EFT uncertainty by focusing on a specific energy and angle. Figure 4.3 expands on Fig. 5 of Paper III. The figure shows the PPDs and the inferred χ EFT uncertainty distributions, using Eqs. (4.10)-(4.11), at $E_{\text{Lab}} = 12$ MeV and $\theta_{\text{c.m.}} = 120$ degrees. Note that the distributions shown are reflective of all observables shown in Fig. 4.2 up to

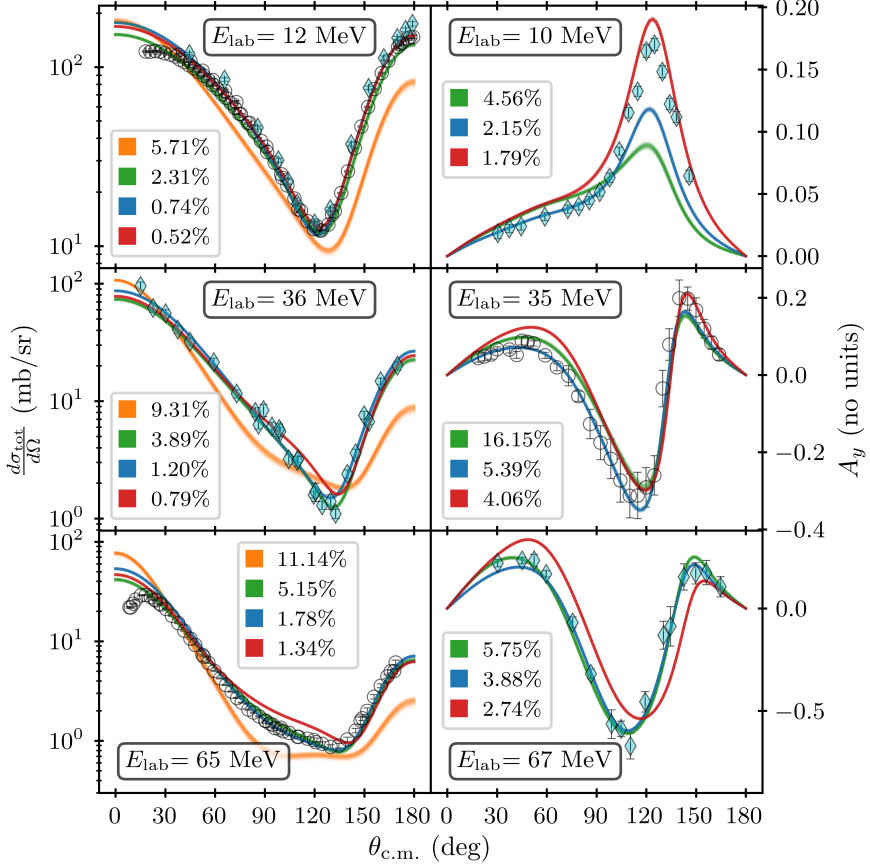


Figure 4.2: PPDs for nd differential cross section (left column) and neutron vector analysing power (right column), modified from Figs. 4 and 6 in Paper III. The colours are the same as in Fig. 4.1. Diamond (cyan) and circles (colourless) markers were retrieved using the EXFOR database (at $E_{\text{Lab}} = 10, 12, 36,$ and 67 MeV) [25], and Ref. [108] (at $E_{\text{Lab}} = 64.5$ MeV) and Ref. [109] (at $E_{\text{Lab}} = 35$ MeV). The percentages are average HDPIs, see text for more information.

$E_{\text{Lab}} = 67$ MeV. For LO- N^2 LO, the PPD widths are again very narrow relative to the χ EFT truncation uncertainty. At N^3 LO, the distributions are roughly equal, meaning LEC variability appears as relevant as omitted chiral orders. Note that at N^3 LO, however, the PPD and χ EFT uncertainty are narrower than typical experimental uncertainty. Furthermore, I emphasise that the uncertainty model

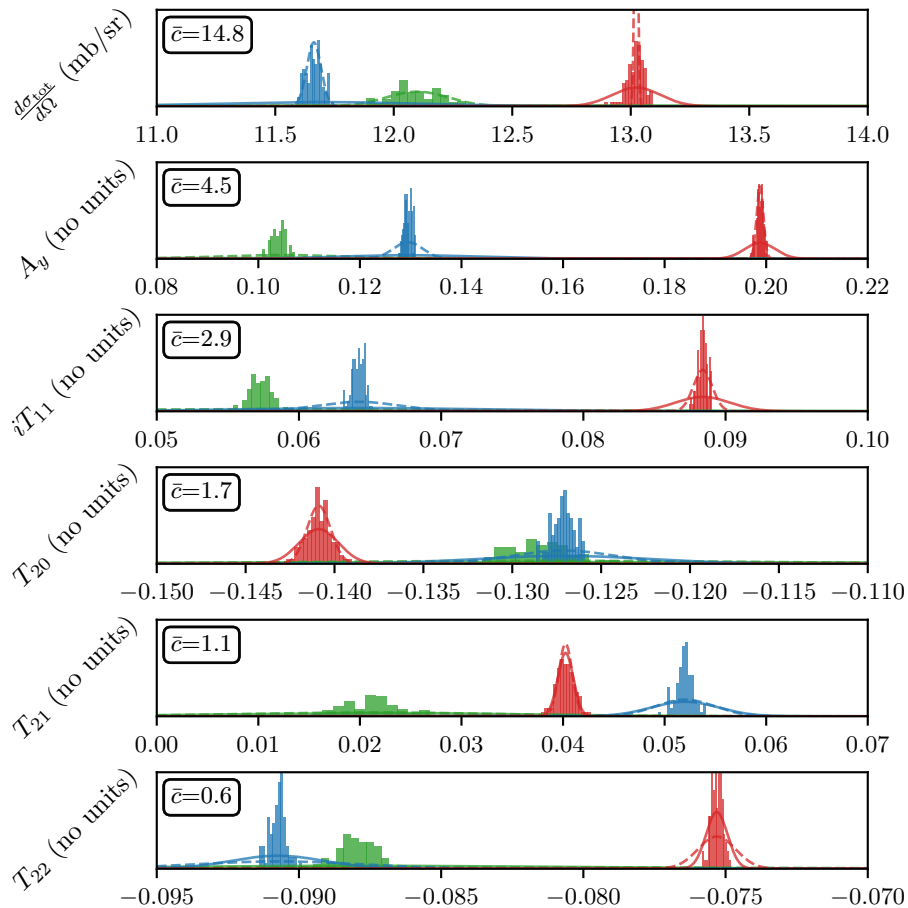


Figure 4.3: PPDs versus χ EFT uncertainty estimates using PPD means for nd scattering observables at $E_{\text{Lab}} = 12$ MeV and scattering angle $\theta = 120$ degrees. The colour-coding is the same as Fig. 4.1. The solid lines are normal distributions with variance set by the standard deviation (shown in figure) of the chiral expansion coefficients, see Eq. (4.10). The dashed lines are the same distributions with natural variance $\bar{c}^2 = 1$.

does not account for missing 3NFs.

In summary, the LEC variability of 2NFs does not resolve experimental discrepancy for elastic nd scattering observables for $E_{\text{Lab}} \leq 67$ MeV. Standard Weinberg power counting suggests that the inclusion of 3NFs should contribute more to χ EFT observable predictions than 2NFs at orders above $N^3\text{LO}$. This

promotes the inclusion of 3NFs as the natural next step in attempting to resolve theoretical discrepancy, such as the A_y puzzle. Once 3NFs are included, we can continue this study to see whether or not including higher chiral orders beyond N³LO is necessary to reproduce experimental data for $E_{\text{Lab}} \leq 67$ MeV.

Chapter 5

Summary and outlook

Understanding atomic nuclei and nuclear matter from fundamental principles is challenging due to the nonperturbative nature of the strong-force interactions occurring in low-energy QCD. Instead, *ab initio* predictions can be done through strong-force models derived from χ EFT, which inherently includes many-nucleon forces with *a priori* undetermined LEC values. These LECs are currently inferred from nuclear observables. Using NN and Nd scattering observables is important for studying 2NFs and 3NFs due to their physical simplicity, ample available data, and unambiguous external momentum for the χ EFT soft scale. In this work, I have studied and implemented the WPCD method as a means to efficiently predict low-energy NN and Nd elastic scattering cross sections. This effort was aimed towards promoting statistical inference of chiral 2NFs and 3NFs in the NNN continuum, which has insofar been hampered by the computational cost of solving the Faddeev equations. The formalism of NN and Nd scattering was summarised in Chap. 2, while the formalism and performance of the method was summarised in Chap. 3 along with the studies of Papers I and II. Specifically, in Chap. 3, the Nd -scattering code developed as part of this study, Tic-tac, is summarised with commentary on the key computational bottlenecks and current performance. In Chap. 4, I summarise our findings of Paper III, where we quantified PPDs of nd -scattering cross sections from chiral 2NFs constrained on NN scattering data.

The WPCD method for few-nucleon scattering and Tic-tac

The WPCD method is a bound-state type method that projects the continuum onto a discrete lattice of “bins”, effectively integrating continuum-representations of operators into an average value across each bin. This coarseness of the method makes it more approximative than others, for example the MI method, such that it typically requires larger basis sizes for accurate predictions. Advantageously, however, it provides approximate scattering states, SWPs, that significantly

simplify the computational challenges of solving both the NN LS and Nd Faddeev equations as shown in Chap. 3. In the same chapter I also summarise the findings of Papers I and II.

Paper I presents a study into WPCD performance, i.e. accuracy versus time usage, for NN scattering observable predictions. We found that whereas the WPCD method has much lower computational complexity than the MI method, given equal basis sizes, the latter has significantly higher accuracy. We compared prediction accuracy versus time usage and found that for low-accuracy results, e.g., when accepting around 2% RMSE of the total np cross section for $N_{\text{WP}} \leq 32$, the WPCD method was roughly twice as fast as the MI method. These time profile were made with a GPU-accelerated code utilising the inherent parallelism of the WPCD method, and a highly efficient CPU-implementation of the MI method [94]. For higher accuracies, the slow convergence of observable accuracy with N_{WP} make MI a more efficient method, in the current implementations.

In Paper II we presented a newly written code, named Tic-tac, for solving the Nd AGS equations using WPCD. We also presented new nd scattering observable predictions using the $N2LO_{\text{opt}}$ NN potential. Much focus was oriented on the convergence of nd scattering observable predictions with the basis size, N_{WP} . We found that using $N_{\text{WP}} \geq 100$ is usually sufficiently accurate compared to experimental errors, although this is dependant on both the scattering energy and the observable studied. Compared to NN scattering, this is a large basis size. Based on Paper I, the NN Hamiltonian appears well-represented already at about $N_{\text{WP}} = 32$. Therefore, the required higher basis dimension may be explained by the highly detailed permutation operator of the Faddeev equations, which may require a high-resolution basis for accurate portrayal.

The Tic-tac code is currently incomplete and does not include 3NFs or Coulomb interactions in observable predictions, and there are several unexplored avenues for optimisation:

- *Include break-up amplitudes.* The U -matrix is calculated a SWP-basis representation. This basis contains the elastic deuteron channel but also the break-up scattering amplitudes. It is simple and straightforward to extend the code to provide such amplitudes as well [85].
- *Include 3NFs.* Currently the code only uses 2NFs. An inclusion of 3NFs would still rely on the FWP and SWP bases, allowing one to simply extend on the current code without major structural changes. Furthermore, there are rewrites of the AGS equations that efficiently include 3NFs [111] which may possibly be combined with the WPCD method.
- *Include Coulomb interactions.* The code does not treat Coulomb interactions, such that it currently cannot provide pd predictions accounting for electromagnetic effects. In scattering, Coulomb effects are included through Coulomb wave functions, see, e.g., the review of Ref. [112]. In

WPCD, these wave functions can be integrated similarly to plane-wave states to form Coulomb wave packets [51, 113]. I have omitted such forces since electromagnetic effects are small in the NNN continuum and limited to small scattering angles [33].

- *Optimise memory usage.* As described in Sec. 3.4.1, currently Tic-tac’s runtime is dominated by accesses to the computer memory, in the repeated reconstruction of the kernel \mathbf{A} . The cost is largely owed to the sparse structure of the permutation matrix making lookup routines of non-zero matrix elements expensive. Further consideration of the memory layout of \mathbf{P} may be profitable. Furthermore, each momentum-violating overlap of wave-packets in the permutation matrix reappears for all NNN partial-wave channels, (α', α) . If there are $N_\alpha = 60$ partial-wave states in the statespace, there are $60^2 = 3600$ reappearances of the same wave-packet overlap. Currently, Tic-tac does not exploit this fact in any way to achieve optimisation, and instead relies only on optimised non-zero element look-ups in the global computer memory.
- *Increase \hat{P}_{123} resolution.* Another avenue for code acceleration may lie in investigating alternative bases to use when numerically calculating the inner products of \mathbf{A} . For example, as discussed in Chap. 4, one can use a spline basis for the product $\hat{P}\hat{v}$, followed by a projection onto the SWP basis.
- *Explore model reduction methods.* Recent advances in model reduction methods [114] focusing on scattering, such as singular value decomposition [49] and eigenvector continuation [47], show promise in reducing the matrix dimensions involved in obtaining scattering solutions. Such reduction methods would undoubtedly reduce the large basis sizes required in WPCD, and notably the derived form of the LS equation used in Ref. [49] is identical to the Faddeev equations as used in Tic-tac.

PPDs of nd scattering observables

In Paper III we calculated PPDs for nd elastic scattering observables using chiral LO-N³LO NN potentials with LECs inferred from NN scattering data [31, 32]. The PPDs were constructed using $N_{\text{WP}} = 75$ scattering predictions and 100 samples of the LEC PDFs, using an extrapolation approach to achieve higher accuracy. Overall, we found that most of the PPDs for nd observables had between 5.7% and 0.5% average HDPI. As a simple rule of thumb, one can say that we found that the PPDs are comparable to typical experimental errors, and two to three orders of magnitude narrower than the χ EFT uncertainty, except for at N³LO where the χ EFT uncertainty and PPDs are similarly wide.

The narrow PPDs from LEC-variability of NN potentials, when inferred on NN scattering data, do not resolve the long-standing theoretical discrepancies to experimental data such as in the A_y puzzle. The analysis of Paper III is not the first to suggest this [39], although, insofar as I am aware, the study is the first fully Bayesian analysis to do so.

We go on to conclude that in order to resolve the theoretical discrepancies, it is best to dedicate efforts into continuing the study by including 3NFs. This, of course, is a cumbersome computational task that requires further development of Nd scattering simulations. One option to achieve this is the realisation of the aforementioned inclusion of 3NFs and suggested optimisations of Tic-tac. Besides this, there are improvements to be made on the methodology of Paper III as well:

- *Improving χ EFT uncertainty modelling.* In future studies aimed at determining coverage of experimental NNN scattering data by χ EFT models, it is important to improve the truncation uncertainty model used here. For example, in Paper III, we did not account for correlations between truncation errors in separate, but close, kinematic regions. Correlated errors were not considered in the LEC-inference study [32] we utilised either, raising concern as to whether the LECs may have been overfitted to NN scattering data. One option to model correlated errors is by the use of Gaussian processes, see, e.g., Ref. [30]. In the Paper, we also used a point-estimate prior for the χ EFT uncertainty normal distribution, in the form of a root-mean square fit of the variance. An improvement on this would be to use, e.g., a conjugate prior such as a normal inverse- χ^2 distribution.
- *Simultaneous fit to NN and Nd scattering data.* As mentioned, the inference study of Ref. [32] only used NN scattering data. An expansion on the investigation of Paper III would be to constrain NN forces on both NN and Nd scattering data, and see if the resulting PDFs of LECs, and consequent PPDs, significantly change. Such a change could indicate, for example, that the LECs were overfitted to NN scattering data.
- *Modelling the WPCD method uncertainty.* In Paper III, the WPCD uncertainty was not quantified. However, without further optimisation, future statistical studies may require significant reduction in the WPCD basis size to gain computational speedup. As mentioned, for example, PDFs usually require thousands of samples, which is currently challenging with Tic-tac to constrain LECs on Nd data. As a result, it would be necessary to formulate a WPCD uncertainty model to ensure method inaccuracy does not spoil the statistical content with uncertainty, when reducing the WPCD basis size.

-
- *Including higher scattering energies.* The study of Paper III focused on a region where 3NFs were believed negligible; $E_{\text{Lab}} \lesssim 67$ MeV. If 3NFs are included, this limitation is no longer necessary, but going beyond brings new challenges. Firstly, the partial-wave statespace may increase as $J \leq 3$ is, for some observables, not sufficient [33]. Secondly, the Chebyshev mesh used here appears to work well for $E_{\text{Lab}} \leq 100$ MeV, but for $E_{\text{Lab}} \geq 100$ MeV the mesh may be optimised by changing the scaling factor in Eq. (3.11).
 - *Use emulators.* Emulators are methods that accurately approximate the outcome of some other method, at a significantly lower cost. One alternative was mentioned above with model reduction methods. Especially eigenvector continuation is well-suited for exploring parametric spaces of models, such as the LECs [47]. Thus, it is clear that emulators can serve to drastically speedup statistical studies, e.g., inference of LECs, in the NNN continuum.

It has been over 60 years since L. Faddeev first suggested a means to solve NNN scattering, and it has been over 30 years since we could first compute accurate solutions to his equations. Today, we can rigorously quantify *ab initio* predictions of NNN scattering observables. By the summary above, the near future is likely to bring quantitative statistical inference of 2NFs and 3NFs using the NNN continuum.

Appendix A

Discretising the continuum using pseudostate eigendifferentials

This discussion follows Ref. [51]. To discretise the continuum we can consider an arbitrary scattering observable that is dependent on the full Hamiltonian, $\hat{O}(\hat{h})$. It can be expressed as an expansion in an arbitrary basis $\mathcal{B} \equiv \{|\psi_i^b\rangle, |\psi(E')\rangle\}_{i=1}^{n_b}$ with energies $e_i^b < 0$ and $E' > 0$, respectively, as

$$\langle \Psi(E) | \hat{O}(\hat{h}) | \Psi(E) \rangle = \sum_{i=1}^{n_b} u(\epsilon_i^b) |\langle \Psi | \psi_i^b \rangle|^2 + \int_0^\infty dE' u(E') |\langle \Psi | \psi(E') \rangle|^2, \quad (\text{A.1})$$

where I define $u(\epsilon_i^b) = \langle \psi_i^b | \hat{O} | \psi_i^b \rangle$ and $u(E') = \langle \psi(E') | \hat{O} | \psi(E') \rangle$. Computationally we cannot work with infinite bases and have to truncate the continuous component of \mathcal{B} to a finite mesh of size n ,

$$\langle \Psi | \hat{O}(\hat{h}) | \Psi \rangle \approx \sum_{i=1}^{n_b} u(\epsilon_i^b) |\langle \Psi | \psi_i^b \rangle|^2 + \sum_{i=1}^n u(E_i) |\langle \Psi | \tilde{\psi}_i \rangle|^2, \quad (\text{A.2})$$

where I replace $\psi(E') \rightarrow \tilde{\psi}_i$, which has energy $E_i > 0$. The positive-energy states of the truncated basis can be called pseudostates: “pseudo-” since their basis does not span the full continuum. To successfully approximate Eq. (A.1), we introduce “equivalent quadrature” [115, 116] weights w_i defined by

$$|\langle \Psi | \tilde{\psi}_i \rangle|^2 = w_i |\langle \Psi | \psi(E_i) \rangle|^2. \quad (\text{A.3})$$

From this we can introduce the following approximate relation,

$$\langle \psi(E_i) | \hat{O}(\hat{h}) | \psi(E_i) \rangle \approx \frac{\langle \tilde{\psi}_i | \hat{O} | \tilde{\psi}_i \rangle}{\sqrt{w_i}}, \quad (\text{A.4})$$

from which, if we know the weights, we can approximate the expectation values of $\hat{O}(\hat{h})$ at the energies E_i . Provision of the weights is where we make use of eigendifferentials.

An unnormalised eigendifferential is defined as the integral over some finite interval $\mathcal{D} \equiv [E, E + \Delta E]$, or “bin”, of the continuum state $|\psi(E')\rangle$ with respect to the energy E' ,

$$|\psi(E, \Delta E)\rangle \equiv \int_E^{E+\Delta E} dE' |\psi(E')\rangle. \quad (\text{A.5})$$

We can discretise the continuum with a basis $\{\mathcal{D}_i | \mathcal{D}_i \cap \mathcal{D}_j = \emptyset \forall i \neq j\}_{i=1}^N$, where $\mathcal{D}_i \equiv [E_i, E_i + \Delta E_i]$. By letting N be finite we get a pseudostate eigendifferential basis. From the definition we can extract an approximative relation for the expectation value of $\hat{O}(\hat{h})$,

$$\langle \Psi(E) | \hat{O}(\hat{h}) | \psi(E') \rangle \approx \frac{\langle \Psi(E) | \hat{O} | \psi(E_i, \Delta E_i) \rangle}{\sqrt{\Delta E_i}}, \quad (\text{A.6})$$

from which it can be argued [80, 81, 117], upon comparison of Eqs. (A.4) and (A.6), that we have the approximation

$$w_i \approx \Delta E_i. \quad (\text{A.7})$$

The pseudostate eigendifferential basis thus provides quadrature weights automatically through the bin widths ΔE . It is interesting to note that in the limit $N_{\text{WP}} \rightarrow \infty$, when $\Delta E_i \rightarrow 0 \forall i$, all the eigendifferential expressions will reduce to the non-pseudostate expressions smoothly. We thus have a systematically improvable method by increasing the number of pseudostate eigendifferentials.

Appendix B

Posterior predictive distributions for neutron-deuteron spin-observables

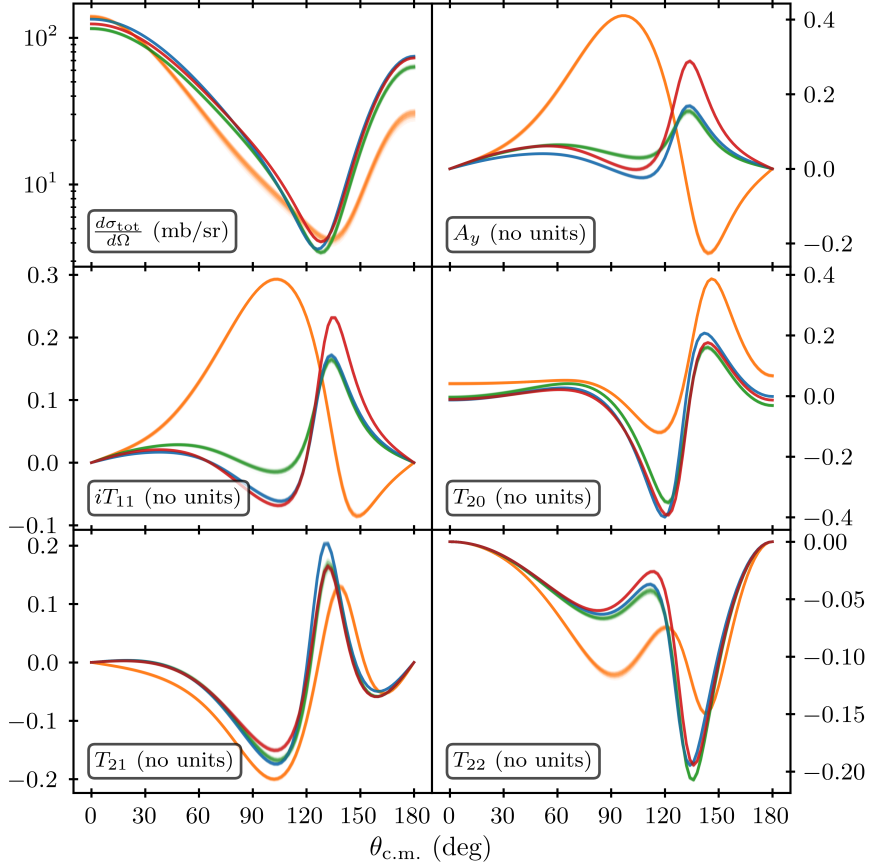


Figure B.1: PPDs for nd scattering observables at $E_{\text{Lab}} = 20$ MeV in same style as Fig. 4.2.

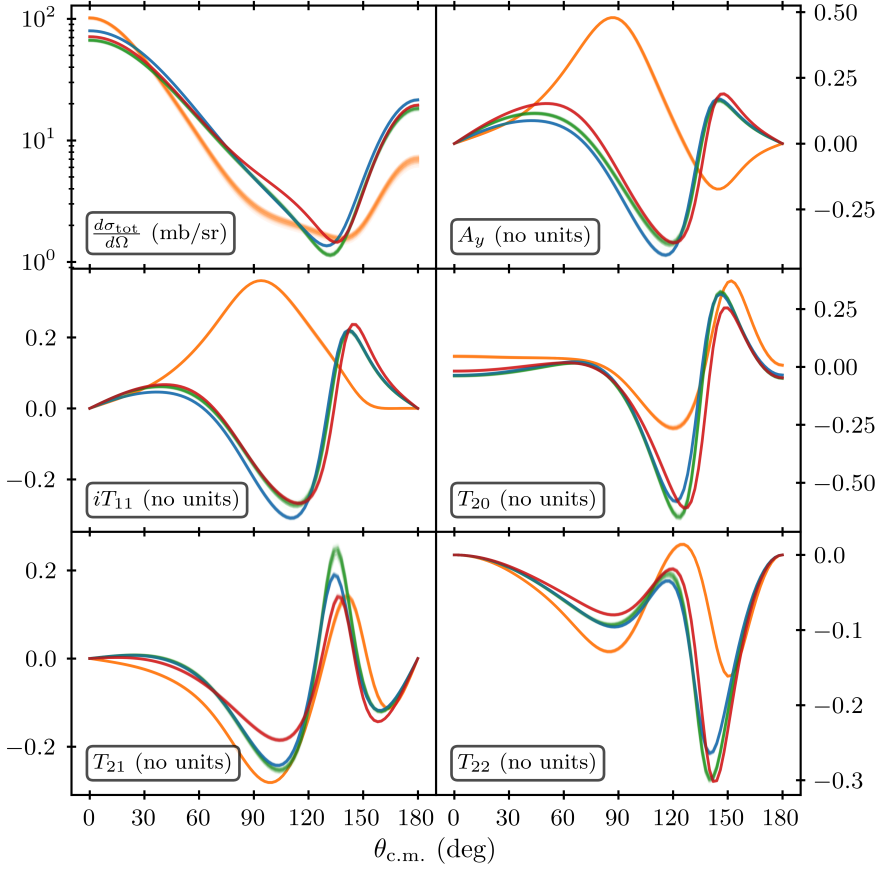


Figure B.2: PPDs for nd scattering observables at $E_{\text{Lab}} = 40$ MeV in same style as Fig. 4.2.

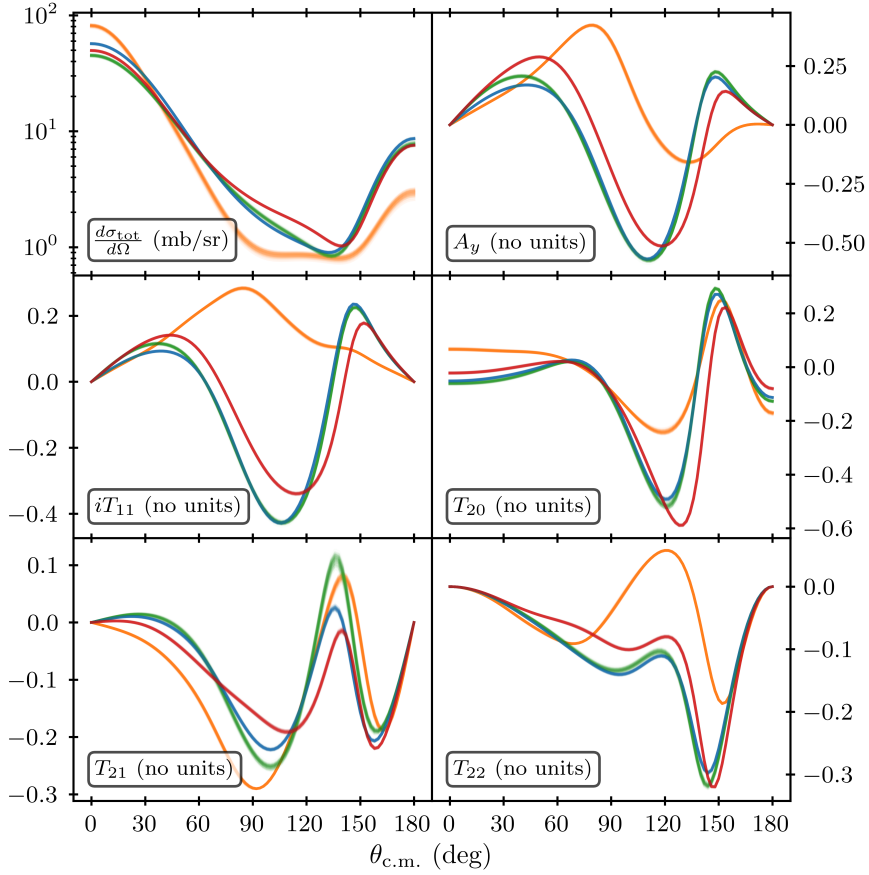


Figure B.3: PPDs for nd scattering observables at $E_{\text{Lab}} = 60$ MeV in same style as Fig. 4.2.

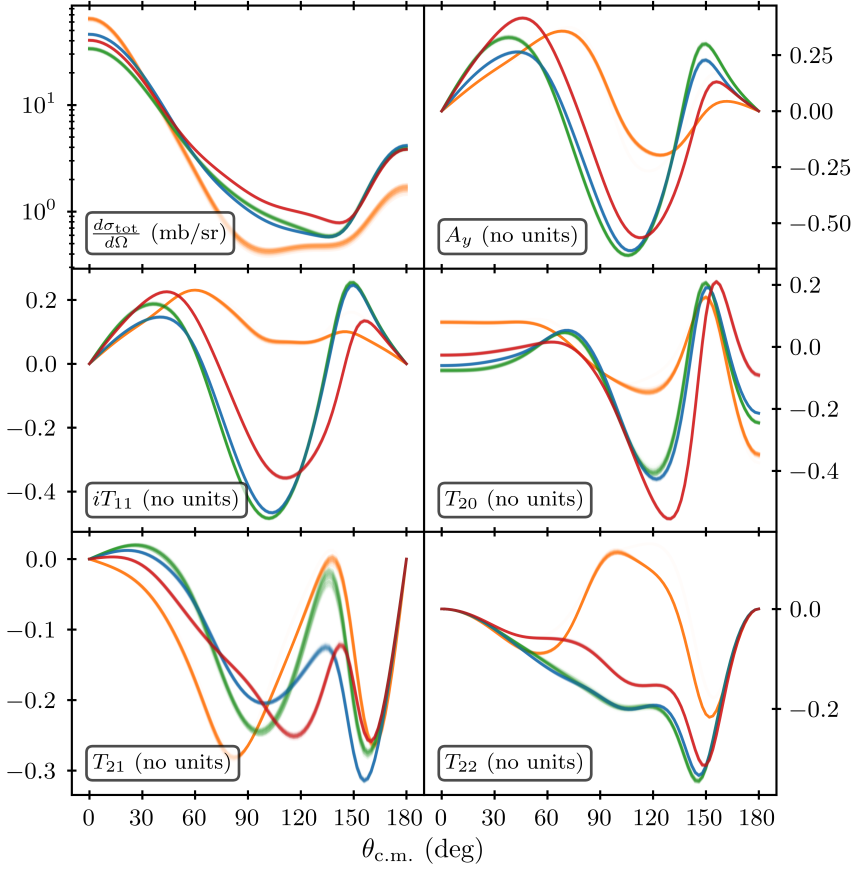


Figure B.4: PPDs for nd scattering observables at $E_{\text{Lab}} = 80$ MeV in same style as Fig. 4.2.

Bibliography

- [1] H. Fritzsche, “History of QCD”, *Subnucl. Ser.* **50**, edited by A. Zichichi, 23–27 (2014).
- [2] A. Deur, S. J. Brodsky and G. F. de Teramond, “The QCD Running Coupling”, *Nucl. Phys.* **90**, 1 (2016), arXiv:1604.08082 [hep-ph].
- [3] S. Weinberg, “Phenomenological Lagrangians”, *Physica A* **96**, edited by S. Deser, 327–340 (1979).
- [4] H. W. Hammer, S. König and U. van Kolck, “Nuclear effective field theory: status and perspectives”, *Rev. Mod. Phys.* **92**, 025004 (2020), arXiv:1906.12122 [nucl-th].
- [5] S. Scherer and M. R. Schindler, *A Primer for Chiral Perturbation Theory*, Vol. 830 (Springer, 2012).
- [6] S. Weinberg, “Nuclear forces from chiral Lagrangians”, *Phys. Lett. B* **251**, 288–292 (1990).
- [7] S. Weinberg, “Effective chiral Lagrangians for nucleon - pion interactions and nuclear forces”, *Nucl. Phys. B* **363**, 3–18 (1991).
- [8] S. Weinberg, “Three body interactions among nucleons and pions”, *Phys. Lett. B* **295**, 114–121 (1992), arXiv:hep-ph/9209257.
- [9] M. Rho, “Exchange currents from chiral Lagrangians”, *Phys. Rev. Lett.* **66**, 1275–1278 (1991).
- [10] C. Ordóñez and U. van Kolck, “Chiral lagrangians and nuclear forces”, *Phys. Lett. B* **291**, 459–464 (1992).
- [11] C. Ordóñez, L. Ray and U. van Kolck, “Nucleon-nucleon potential from an effective chiral Lagrangian”, *Phys. Rev. Lett.* **72**, 1982–1985 (1994).
- [12] P. F. Bedaque and U. van Kolck, “Effective field theory for few nucleon systems”, *Ann. Rev. Nucl. Part. Sci.* **52**, 339–396 (2002), arXiv:nucl-th/0203055.
- [13] E. Epelbaum, H.-W. Hammer and U.-G. Meissner, “Modern Theory of Nuclear Forces”, *Rev. Mod. Phys.* **81**, 1773–1825 (2009), arXiv:0811.1338 [nucl-th].

-
- [14] R. Machleidt and D. R. Entem, “Chiral effective field theory and nuclear forces”, *Phys. Rept.* **503**, 1–75 (2011), [arXiv:1105.2919 \[nucl-th\]](#).
- [15] C. J. Yang, A. Ekström, C. Forssén and G. Hagen, “Power counting in chiral effective field theory and nuclear binding”, *Phys. Rev. C* **103**, 054304 (2021), [arXiv:2011.11584 \[nucl-th\]](#).
- [16] H.-W. Hammer, A. Nogga and A. Schwenk, “Three-body forces: From cold atoms to nuclei”, *Rev. Mod. Phys.* **85**, 197 (2013), [arXiv:1210.4273 \[nucl-th\]](#).
- [17] K. Hebeler, “Three-nucleon forces: Implementation and applications to atomic nuclei and dense matter”, *Phys. Rept.* **890**, 1–116 (2021), [arXiv:2002.09548 \[nucl-th\]](#).
- [18] C. C. Chang et al., “A per-cent-level determination of the nucleon axial coupling from quantum chromodynamics”, *Nature* **558**, 91–94 (2018), [arXiv:1805.12130 \[hep-lat\]](#).
- [19] I. Tews, Z. Davoudi, A. Ekström, J. D. Holt and J. E. Lynn, “New Ideas in Constraining Nuclear Forces”, *J. Phys. G* **47**, 103001 (2020), [arXiv:2001.03334 \[nucl-th\]](#).
- [20] T. Djärv, A. Ekström, C. Forssén and H. T. Johansson, “Bayesian predictions for A=6 nuclei using eigenvector continuation emulators”, *Phys. Rev. C* **105**, 014005 (2022), [arXiv:2108.13313 \[nucl-th\]](#).
- [21] P. Navrátil, S. Quaglioni, G. Hupin, C. Romero-Redondo and A. Calci, “Unified *ab initio* approaches to nuclear structure and reactions”, *Phys. Scripta* **91**, 053002 (2016), [arXiv:1601.03765 \[nucl-th\]](#).
- [22] H. Hergert, “A Guided Tour of *ab initio* Nuclear Many-Body Theory”, *Front. in Phys.* **8**, 379 (2020), [arXiv:2008.05061 \[nucl-th\]](#).
- [23] B. Hu, W. Jiang, T. Miyagi, Z. Sun, A. Ekström, C. Forssén, G. Hagen, J. D. Holt, T. Papenbrock, S. R. Stroberg and I. Vernon, “*Ab initio* predictions link the neutron skin of ^{208}Pb to nuclear forces”, *Nat. Phys.*, [10.1038/s41567-022-01715-8](#) (2022), [arXiv:2112.01125 \[nucl-th\]](#).
- [24] E. Epelbaum, H. Krebs and P. Reinert, “High-precision nuclear forces from chiral EFT: State-of-the-art, challenges and outlook”, *Front. in Phys.* **8**, 98 (2020), [arXiv:1911.11875 \[nucl-th\]](#).
- [25] N. Otuka et al., “Towards a More Complete and Accurate Experimental Nuclear Reaction Data Library (EXFOR): International Collaboration Between Nuclear Reaction Data Centres (NRDC)”, *Nucl. Data Sheets* **120**, 272–276 (2014), [arXiv:2002.07114 \[nucl-ex\]](#).
- [26] L. D. Faddeev, “Scattering theory for a three particle system”, *Zh. Eksp. Teor. Fiz.* **39**, 1459–1467 (1960).

- [27] S. Wesolowski, N. Klco, R. J. Furnstahl, D. R. Phillips and A. Thapaliya, “Bayesian parameter estimation for effective field theories”, *J. Phys. G* **43**, 074001 (2016), [arXiv:1511.03618 \[nucl-th\]](#).
- [28] J. A. Melendez, S. Wesolowski and R. J. Furnstahl, “Bayesian truncation errors in chiral effective field theory: nucleon-nucleon observables”, *Phys. Rev. C* **96**, 024003 (2017), [arXiv:1704.03308 \[nucl-th\]](#).
- [29] S. Wesolowski, R. J. Furnstahl, J. A. Melendez and D. R. Phillips, “Exploring Bayesian parameter estimation for chiral effective field theory using nucleon–nucleon phase shifts”, *J. Phys. G* **46**, 045102 (2019), [arXiv:1808.08211 \[nucl-th\]](#).
- [30] J. A. Melendez, R. J. Furnstahl, D. R. Phillips, M. T. Pratala and S. Wesolowski, “Quantifying Correlated Truncation Errors in Effective Field Theory”, *Phys. Rev. C* **100**, 044001 (2019), [arXiv:1904.10581 \[nucl-th\]](#).
- [31] I. Svensson, A. Ekström and C. Forssén, “Bayesian parameter estimation in chiral effective field theory using the Hamiltonian Monte Carlo method”, *Phys. Rev. C* **105**, 014004 (2022), [arXiv:2110.04011 \[nucl-th\]](#).
- [32] I. Svensson, A. Ekström and C. Forssén, *Bayesian estimation of the low-energy constants up to fourth order in the nucleon-nucleon sector of chiral effective field theory*, (2022) [arXiv:2206.08250 \[nucl-th\]](#).
- [33] W. Glöckle, H. Witała, D. Hüber, H. Kamada and J. Golak, “The Three nucleon continuum: Achievements, challenges and applications”, *Phys. Rept.* **274**, 107–285 (1996).
- [34] C. R. Chen, G. L. Payne, J. L. Friar and B. F. Gibson, “Low-energy nucleon-deuteron scattering”, *Phys. Rev. C* **39**, 1261–1268 (1989).
- [35] A. Kievsky, M. Viviani and S. Rosati, “Polarization observables in p - d scattering below 30-MeV”, *Phys. Rev. C* **64**, 024002 (2001), [arXiv:nucl-th/0103058](#).
- [36] S. Binder et al., “Few-nucleon systems with state-of-the-art chiral nucleon-nucleon forces”, *Phys. Rev. C* **93**, 044002 (2016), [arXiv:1505.07218 \[nucl-th\]](#).
- [37] E. Epelbaum et al., “Towards high-order calculations of three-nucleon scattering in chiral effective field theory”, *Eur. Phys. J. A* **56**, 92 (2020), [arXiv:1907.03608 \[nucl-th\]](#).
- [38] R. Skibiński, Y. Volkotrub, J. Golak, K. Topolnicki and H. Witała, “Theoretical uncertainties of the elastic nucleon-deuteron scattering observables”, *Phys. Rev. C* **98**, 014001 (2018), [arXiv:1803.10345 \[nucl-th\]](#).

-
- [39] Y. Volkotrub, J. Golak, R. Skibiński, K. Topolnicki, H. Witała, E. Epelbaum, H. Krebs and P. Reinert, “Uncertainty of three-nucleon continuum observables arising from uncertainties of two-nucleon potential parameters”, *J. Phys. G* **47**, 104001 (2020), [arXiv:2003.06175 \[nucl-th\]](#).
- [40] P. Reinert, H. Krebs and E. Epelbaum, “Semilocal momentum-space regularized chiral two-nucleon potentials up to fifth order”, *Eur. Phys. J. A* **54**, 86 (2018), [arXiv:1711.08821 \[nucl-th\]](#).
- [41] H. Witała, J. Golak, R. Skibiński, W. Glöckle, H. Kamada and W. N. Polyzou, “Three-nucleon force in relativistic three-nucleon Faddeev calculations”, *Phys. Rev. C* **83**, [Erratum: *Phys.Rev.C* 88, 069904 (2013)], 044001 (2011), [arXiv:1101.4053 \[nucl-th\]](#).
- [42] J. Golak et al., “Investigations of the few-nucleon systems within the LENPIC project”, *SciPost Phys. Proc.* **3**, 002 (2020).
- [43] J. Carbonell, A. Deltuva, A. C. Fonseca and R. Lazauskas, “Bound state techniques to solve the multiparticle scattering problem”, *Prog. Part. Nucl. Phys.* **74**, 55–80 (2014), [arXiv:1310.6631 \[nucl-th\]](#).
- [44] D. Frame, R. He, I. Ipsen, D. Lee, D. Lee and E. Rrapaj, “Eigenvector continuation with subspace learning”, *Phys. Rev. Lett.* **121**, 032501 (2018), [arXiv:1711.07090 \[nucl-th\]](#).
- [45] R. J. Furnstahl, A. J. Garcia, P. J. Millican and X. Zhang, “Efficient emulators for scattering using eigenvector continuation”, *Phys. Lett. B* **809**, 135719 (2020), [arXiv:2007.03635 \[nucl-th\]](#).
- [46] J. A. Melendez, C. Drischler, A. J. Garcia, R. J. Furnstahl and X. Zhang, “Fast & accurate emulation of two-body scattering observables without wave functions”, *Phys. Lett. B* **821**, 136608 (2021), [arXiv:2106.15608 \[nucl-th\]](#).
- [47] X. Zhang and R. J. Furnstahl, “Fast emulation of quantum three-body scattering”, *Phys. Rev. C* **105**, 064004 (2022), [arXiv:2110.04269 \[nucl-th\]](#).
- [48] A. Tichai, P. Arthuis, K. Hebeler, M. Heinz, J. Hoppe and A. Schwenk, “Low-rank matrix decompositions for ab initio nuclear structure”, *Phys. Lett. B* **821**, 136623 (2021), [arXiv:2105.03935 \[nucl-th\]](#).
- [49] A. Tichai, P. Arthuis, K. Hebeler, M. Heinz, J. Hoppe, A. Schwenk and L. Zurek, “Least-square approach for singular value decompositions of scattering problems”, *Phys. Rev. C* **106**, 024320 (2022), [arXiv:2205.10087 \[nucl-th\]](#).
- [50] H. Witała, J. Golak and R. Skibiński, “Efficient emulator for solving three-nucleon continuum Faddeev equations with chiral three-nucleon force comprising any number of contact terms”, *Eur. Phys. J. A* **57**, 241 (2021), [arXiv:2103.13237 \[nucl-th\]](#).

- [51] O. A. Rubtsova, V. I. Kukulin and V. N. Pomerantsev, “Wave-packet continuum discretization for quantum scattering”, *Ann. Phys.* **360**, 613–654 (2015), [arXiv:1501.02531 \[nucl-th\]](#).
- [52] V. N. Pomerantsev, V. I. Kukulin and O. A. Rubtsova, “Solving three-body scattering problem in the momentum lattice representation”, *Phys. Rev. C* **79**, 034001 (2009), [arXiv:0812.0572 \[nucl-th\]](#).
- [53] V. Pomerantsev, V. Kukulin, O. Rubtsova and S. Sakhiev, “Fast gpu-based calculations in few-body quantum scattering”, *Comput. Phys. Commun.* **204**, 121–131 (2016), [arXiv:1508.07441 \[physics.comp-ph\]](#).
- [54] H. Witała, W. Glöckle and T. Cornelius, “Rigorous Faddeev calculations for elastic neutron-deuteron scattering around 8 MeV c.m. energy”, *Nucl. Phys. A* **491**, 157–172 (1989).
- [55] D. Hüber and J. L. Friar, “The A_y puzzle and the nuclear force”, *Phys. Rev. C* **58**, 674–685 (1998), [arXiv:nucl-th/9803038](#).
- [56] H. Witała, W. Glöckle, D. Hüber, J. Golak and H. Kamada, “The Cross-section minima in elastic Nd scattering: A ‘Smoking gun’ for three nucleon force effects”, *Phys. Rev. Lett.* **81**, 1183–1186 (1998), [arXiv:nucl-th/9801018](#).
- [57] H. Witała, J. Golak and R. Skibiński, “Significance of chiral three-nucleon force contact terms for understanding of elastic nucleon-deuteron scattering”, *Phys. Rev. C* **105**, 054004 (2022).
- [58] E. W. Schmid and H. Ziegelmann, *The quantum mechanical three-body problem: vieweg tracts in pure and applied physics*, Vol. 2 (Pergamon, 1974).
- [59] W Glöckle, *The quantum mechanical few-body problem*, Texts and monographs in physics (Springer, Berlin, 1983).
- [60] G. G. Ohlsen, “Polarization transfer and spin correlation experiments in nuclear physics”, *Rept. Prog. Phys.* **35**, 717–801 (1972).
- [61] H. H. Barschall and W Haeberli, “Polarization phenomena in nuclear reactions”, Proceedings of the Third International Symposium (1971).
- [62] R. G. Seyler, “Polarization from scattering polarized spin- $\frac{1}{2}$ on unpolarized spin-1 particles”, *Nucl. Phys. A* **124**, 253–272 (1969).
- [63] A. Messiah, *Quantum mechanics* (Courier Corporation, 2014).
- [64] J. R. Taylor, *Scattering theory: the quantum theory of nonrelativistic collisions* (Courier Corporation, 2006).
- [65] M. I. Haftel and F. Tabakin, “Nuclear saturation and the smoothness of nucleon-nucleon potentials”, *Nucl. Phys. A* **158**, 1–42 (1970).

-
- [66] N. J. Higham, *Accuracy and stability of numerical algorithms* (SIAM, 2002).
- [67] A. Ekström et al., “Optimized Chiral Nucleon-Nucleon Interaction at Next-to-Next-to-Leading Order”, *Phys. Rev. Lett.* **110**, 192502 (2013), [arXiv:1303.4674 \[nucl-th\]](#).
- [68] A. M. Lane and R. G. Thomas, “R-Matrix Theory of Nuclear Reactions”, *Rev. Mod. Phys.* **30**, 257–353 (1958).
- [69] D. Hüber, W. Glöckle, J. Golak, H. Witała, H. Kamada, A. Kievsky, S. Rosati and M. Viviani, “Realistic phase shift and mixing parameters for elastic neutron-deuteron scattering: Comparison of momentum space and configuration space methods”, *Phys. Rev. C* **51**, 1100–1107 (1995).
- [70] W. Glöckle, “A new approach to the three-body problem”, *Nucl. Phys. A* **141**, 620–630 (1970).
- [71] E. O. Alt, P. Grassberger and W. Sandhas, “Reduction of the three - particle collision problem to multichannel two - particle Lippmann-Schwinger equations”, *Nucl. Phys. B* **2**, 167–180 (1967).
- [72] H. Witała and W. Glöckle, “Avoiding moving logarithmic singularities in 3n Faddeev equations”, *Mod. Phys. Lett. A* **24**, edited by I. Fachruddin and T. Mart, 779–784 (2009).
- [73] W. Glöckle, G. Hasberg and A. R. Neghabian, “Numerical treatment of few body equations in momentum space by the Spline method”, *Z. Phys. A* **305**, 217–221 (1982).
- [74] A. Stadler, W. Glöckle and P. U. Sauer, “Faddeev equations with three-nucleon force in momentum space”, *Phys. Rev. C* **44**, 2319–2327 (1991).
- [75] R. A. Malfliet and J. A. Tjon, “Solution of the Faddeev equations for the triton problem using local two particle interactions”, *Nucl. Phys. A* **127**, 161–168 (1969).
- [76] G. H. Golub and C. F. Van Loan, *Matrix computations* (JHU press, 2013).
- [77] K. Hebel, personal communication, 2020.
- [78] D. R. Entem and R. Machleidt, “Accurate charge dependent nucleon nucleon potential at fourth order of chiral perturbation theory”, *Phys. Rev. C* **68**, 041001 (2003), [arXiv:nucl-th/0304018](#).
- [79] O. Rubtsova and V. Kukulin, “Wave-packet discretization of a continuum: path toward practically solving few-body scattering problems”, *Phys. At. Nucl.* **70**, 2025 – 2045 (2007).
- [80] V. I. Kukulin and O. A. Rubtsova, “Discrete quantum scattering theory”, *Theor. Math. Phys.* **134**, 404–426 (2003).

- [81] V. I. Kukulin, V. N. Pomerantsev and O. A. Rubtsova, “Wave-packet continuum discretization method for solving the three-body scattering problem”, *Theor. Math. Phys.* **150**, 403–424 (2007).
- [82] V. I. Kukulin and O. A. Rubtsova, “Elastic scattering on a nucleus and the breakup of the composite projectile via wave-packet continuum discretization”, *Phys. Rev. C* **76**, 047601 (2007).
- [83] O. A. Rubtsova, V. I. Kukulin and A. M. Moro, “Continuum discretization methods in a composite-particle scattering off a nucleus: Benchmark calculations”, *Phys. Rev. C* **78**, 034603 (2008), [arXiv:0806.2307 \[nucl-th\]](https://arxiv.org/abs/0806.2307).
- [84] O. A. Rubtsova, V. I. Kukulin, V. N. Pomerantsev and A. Faessler, “New approach toward a direct evaluation of the multichannel multienergy S matrix without solving the scattering equations”, *Phys. Rev. C* **81**, 064003 (2010).
- [85] O. A. Rubtsova, V. N. Pomerantsev, V. I. Kukulin and A. Faessler, “Three-body breakup within the fully discretized Faddeev equations”, *Phys. Rev. C* **86**, 034004 (2012), [arXiv:1205.5730 \[nucl-th\]](https://arxiv.org/abs/1205.5730).
- [86] H. Mütter, O. A. Rubtsova, V. I. Kukulin and V. N. Pomerantsev, “Discrete Wave-Packet Representation in Nuclear Matter Calculations”, *Phys. Rev. C* **94**, 024328 (2016), [arXiv:1607.01694 \[nucl-th\]](https://arxiv.org/abs/1607.01694).
- [87] L. S. Blackford, A. Petitet, R. Pozo, K. Remington, R. C. Whaley, J. Demmel, J. Dongarra, I. Duff, S. Hammarling, G. Henry et al., “An updated set of basic linear algebra subprograms (blas)”, *ACM Transactions on Mathematical Software* **28**, 135–151 (2002).
- [88] Z. Jia, M. Maggioni, J. Smith and D. P. Scarpazza, “Dissecting the nvidia turing t4 gpu via microbenchmarking”, (2019), [arXiv:1903.07486 \[cs.DC\]](https://arxiv.org/abs/1903.07486).
- [89] N. Wilt, *The cuda handbook: a comprehensive guide to gpu programming* (Pearson Education, 2013).
- [90] NVIDIA, P. Vingelmann and F. H. Fitzek, *Cuda, release: 10.2.89*, 2020.
- [91] Nvidia, *Nvidia v100 tensor core gpu*, <https://www.nvidia.com/en-us/data-center/v100/> (visited on 29/05/2022).
- [92] Nvidia, *Nvidia t4*, <https://www.nvidia.com/en-us/data-center/tesla-t4/> (visited on 29/05/2022).
- [93] Nvidia, *Nvidia k80/k40*, <https://www.nvidia.com/content/dam/en-zz/Solutions/Data-Center/tesla-product-literature/TeslaK80-datasheet.pdf> (visited on 29/05/2022).

-
- [94] B. D. Carlsson, A. Ekström, C. Forssén, D. F. Strömberg, G. R. Jansen, O. Lilja, M. Lindby, B. A. Mattsson and K. A. Wendt, “Uncertainty analysis and order-by-order optimization of chiral nuclear interactions”, *Phys. Rev. X* **6**, 011019 (2016), [arXiv:1506.02466 \[nucl-th\]](#).
- [95] E. Anderson, Z. Bai, C. Bischof, S. Blackford, J. Demmel, J. Dongarra, J. Du Croz, A. Greenbaum, S. Hammarling, A. McKenney and D. Sorensen, *LAPACK users’ guide*, Third (Society for Industrial and Applied Mathematics, Philadelphia, PA, 1999).
- [96] S. Weinberg, “Quasiparticles and the Born Series”, *Phys. Rev.* **131**, 440–460 (1963).
- [97] J. Hoppe, C. Drischler, R. J. Furnstahl, K. Hebeler and A. Schwenk, “Weinberg eigenvalues for chiral nucleon-nucleon interactions”, *Phys. Rev. C* **96**, 054002 (2017), [arXiv:1707.06438 \[nucl-th\]](#).
- [98] A. George Jr et al., *Essentials of padé approximants* (Elsevier, 1975).
- [99] V. G. J. Stoks, R. A. M. Klomp, C. P. F. Terheggen and J. J. de Swart, “Construction of high quality N N potential models”, *Phys. Rev. C* **49**, 2950–2962 (1994), [arXiv:nucl-th/9406039](#).
- [100] J. Brynjarsdóttir and A. O’Hagan, “Learning about physical parameters: the importance of model discrepancy”, *Inverse Probl.* **30**, 114007 (2014).
- [101] P. Gregory, *Bayesian logical data analysis for the physical sciences: a comparative approach with mathematica® support* (Cambridge University Press, 2005).
- [102] S. Huth et al., “Constraining Neutron-Star Matter with Microscopic and Macroscopic Collisions”, *Nature* **606**, 276–280 (2022), [arXiv:2107.06229 \[nucl-th\]](#).
- [103] H. Schatz et al., *Horizons: Nuclear Astrophysics in the 2020s and Beyond*, (2022) [arXiv:2205.07996 \[nucl-ex\]](#).
- [104] S. Duane, A. D. Kennedy, B. J. Pendleton and D. Roweth, “Hybrid Monte Carlo”, *Phys. Lett. B* **195**, 216–222 (1987).
- [105] R. J. Furnstahl, N. Klco, D. R. Phillips and S. Wesolowski, “Quantifying truncation errors in effective field theory”, *Phys. Rev. C* **92**, 024005 (2015), [arXiv:1506.01343 \[nucl-th\]](#).
- [106] S. Wesolowski, I. Svensson, A. Ekström, C. Forssén, R. J. Furnstahl, J. A. Melendez and D. R. Phillips, “Rigorous constraints on three-nucleon forces in chiral effective field theory from fast and accurate calculations of few-body observables”, *Phys. Rev. C* **104**, 064001 (2021), [arXiv:2104.04441 \[nucl-th\]](#).

- [107] E. Epelbaum et al., “Few- and many-nucleon systems with semilocal coordinate-space regularized chiral two- and three-body forces”, *Phys. Rev. C* **99**, 024313 (2019), [arXiv:1807.02848 \[nucl-th\]](#).
- [108] H. Shimizu, K. Imai, N. Tamura, K. Nisimura, K. Hatanaka, T. Saito, Y. Koike and Y. Taniguchi, “Analyzing powers and cross sections in elastic p - d scattering at 65 MeV”, *Nucl. Phys. A* **382**, 242–254 (1982).
- [109] S. N. Bunker, J. M. Cameron, R. F. Carlson, J. R. Richardson, P. Tomaš, W. T. H. Van Oers and J. W. Verba, “Differential cross sections and polarizations in elastic p-d scattering at medium energies”, *Nucl. Phys. A* **113**, 461–480 (1968).
- [110] H. Witała, W. Glöckle, J. Golak, H. Kamada, J. Kuros-Zolnierczuk, A. Nogga and R. Skibiński, “Nd elastic scattering as a tool to probe properties of three nucleon forces”, *Phys. Rev. C* **63**, 024007 (2001), [arXiv:nucl-th/0010013](#).
- [111] D. Hüber, H. Kamada, H. Witała and W. Glöckle, “How to include a three nucleon force into Faddeev equations for the 3N continuum: A New form”, *Acta Phys. Polon. B* **28**, 1677–1686 (1997), [arXiv:nucl-th/9611007](#).
- [112] A. Deltuva, A. Fonseca and P. Sauer, “Nuclear Many-Body Scattering Calculations with the Coulomb Interaction”, *Annu. Rev. Nucl. Part. Sci.* **58**, 27–49 (2008).
- [113] V. I. Kukulin and O. A. Rubtsova, “Solving the charged-particle scattering problem by wave packet continuum discretization”, *Theor. Math. Phys.* **145**, 1711–1726 (2005).
- [114] J. A. Melendez, C. Drischler, R. J. Furnstahl, A. J. Garcia and X. Zhang, “Model reduction methods for nuclear emulators”, *J. Phys. G* **49**, 102001 (2022), [arXiv:2203.05528 \[nucl-th\]](#).
- [115] E. J. Heller, T. N. Rescigno and W. P. Reinhardt, “Extraction of scattering information from fredholm determinants calculated in an L^2 basis: a chebyshev discretization of the continuum”, *Phys. Rev. A* **8**, 2946 (1973).
- [116] C. Corcoran and P. Langhoff, “Moment-theory approximations for non-negative spectral densities”, *J. Math. Phys.* **18**, 651–657 (1977).
- [117] O. A. Rubtsova, V. N. Pomerantsev and V. I. Kukulin, “Quantum scattering theory on the momentum lattice”, *Phys. Rev. C* **79**, 064602 (2009).